ALMA MATER STUDIORUM - UNIVERSITÀ DI BOLOGNA

DIPARTIMENTO DI INGEGNERIA DELL'ENERGIA ELETTRICA E
DELL'INFORMAZIONE "GUGLIELMO MARCONI" – DEI

SCUOLA DI DOTTORATO IN SCIENZE E INGEGNERIA DELL'INFORMAZIONE

CICLO XXV

Settore Concorsuale di afferenza: 09/E3
Settore Scientifico disciplinare: ING-INF/01

ANALYSIS OF CHARGE-TRANSPORT PROPERTIES IN GST MATERIALS FOR NEXT GENERATION PHASE-CHANGE MEMORY DEVICES

Tesi di Dottorato

Presentata da Fabio Giovanardi

Coordinatore della Scuola di Dottorato:

Chiar.mo Prof. Ing. ALESSANDRO VANELLI CORALLI

Relatore:

Chiar.mo Prof. Ing. MASSIMO RUDAN

Esame Finale: anno 2013

Contents

List of Figures

List of Tables

List of symbols and abbreviations

Symbols

α_n	Electron-transition coefficient from the band to an empty trap
b_n	Transition coefficient for the impact ionization
c_n	Transition coefficient for the Auger recombination
d_T	Degeneration coefficient
D_n	Diffusivity of the band electrons
Δ_{MB}	$E_C - E_M$
Δ_{sk}	$\lvert E_s - E_k \rvert$
$\mathcal{E}$	Electric field
$\boldsymbol{\mathcal{E}}$	Electric field vector
E	Energy
E_0	Ground level of the traps
E_C	Bottom energy of the conduction band
E_e	Band-electron energy relative to the minimum E_C
E_F	Fermi level energy
E_k	Energy of the kth level of a trap
E_M	Highest trap energy level
e_n	Electron-emission coefficient from a trap to the band
E_s	Energy of the sth level of a trap
f	Filling fraction of the band states
f_k	Filling fraction of the kth level of a trap
G_C	Device conductance
G_n	Device conductance due to band electrons only

G_T	Device conductance due to trap electrons only
γ	Density of states per unit volume of the band
$\boldsymbol{J}$	Current density vector
J	Current density
J^{th}	Current density at threshold
J_n	Band-electron current density
J_n^{th}	Band-electron current density at threshold
k_B	Boltzmann constant
μ_n	Mobility of the band electrons
N	Concentrations of traps
N_k	kth trap level population
n	Concentrations of band electrons
n^{th}	Concentration of the band electrons at threshold
N_C	Effective density of states of the conduction band
n_T	Concentrations of trap electrons
p	Concentration of empty traps
$\dot{P}_{ks}$	Trap electron transition probability from kth to sth level
$\dot{P}_{sk}$	Trap electron transition probability from sth to kth level
$\dot{P}_{sk}^{P}$	Trap electron transition probability due to phonon stimulated-emission/absorption
$\dot{P}_{sk}^{P}$	Trap electron transition probability due to electron interactions
P_T	Occupation probability of the traps
q	Electron elementary charge
R	Resistance
ρ	Charge density
R_s	Resistance due to the memory cell heater, crystalline cap, and upper contact
σ	Keldysh-like cross section
τ_{ki}	Lifetime of spontaneous phonon emission from kth to ith level of the trap
T_L	Lattice temperature
$\boldsymbol{v}_T$	Trap electron velocity vector
u	Angular average of the group velocity of the band electrons
U_{th}	Thermal-recombination rate
	τ_{ki} the lifetime of spontaneous phonon emission

Abbreviations

AFM	Atomic Forcemicroscopy
CNTs	Carbon Nanotubes
CVD	Chemical Vapor Deposition
DOS	Density Of States
DRAM	Dynamic Random Access Memory
GST	$Ge_2Sb_2Te_5$
PCRAM	Phase-Change Random Access Memory
VAPs	Valence Alternation Pairs (VAPs)

Abstract

The quest for universal memory is driving the rapid development of memories with superior all-round capabilities in non-volatility, high speed, high endurance and low power [23].
Memory is a vital part of every modern electronic device. As processors become faster, the memory becomes the main bottleneck of performance, the slowest one being the hard drive. The memory subsystem accounts for a significant cost and power budget of a computer system. Current DRAM-based main memory systems are starting to hit the power and cost limit. To resolve this issue the industry is improving existing technologies such as Flash and exploring new ones. Among those new technologies is the Phase Change Memory (PCM), which overcomes some of the shortcomings of the Flash such as durability (about 10^4 times more write cycles) and scalability. This alternative non-volatile memory technology, which uses resistance contrast in phase-change materials, offers more density relative to DRAM, and can help to increase main memory capacity of future systems while remaining within the cost and power constraints.
Chalcogenide materials can suitably be exploited for manufacturing phase-change memory devices. However, their contradictory speed and stability properties present a key challenge towards this ambition. As the device size decreases, the phase-change mechanism changes from the material inherent crystallization mechanism (either nucleation- or growth-dominated), to the hetero-crystallization mechanism, which resulted in a significant increase in PCRAM speeds. Reducing the grain size can further increase the speed of phase-change. Such grain size effect on speed becomes increasingly significant at smaller device sizes. Together with the nano-thermal and electrical effects, fast phase-change, good stability and high endurance can be achieved. These findings lead to a feasible solution to achieve a universal memory. $Ge_2Sb_2Te_5$ (GST) has been identified as the most interesting material for industrial applications.
Charge transport in amorphous chalcogenide-GST used for memory devices is modeled using two contributions: hopping of trapped electrons and motion of band electrons in extended states. Crystalline GST exhibits an almost Ohmic

$I(V)$ curve. In contrast amorphous GST (a-GST) shows a high resistance at low biases while, above a threshold voltage, a transition takes place from a highly resistive to a conductive state, characterized by a negative differential-resistance behavior. A clear and complete understanding of the threshold behavior of the amorphous phase not only plays a key role in the investigation of the transport properties of GST, but is fundamental for exploiting such materials in the fabrication of innovative nonvolatile memories. The type of feedback that produces the snapback phenomenon is described as a filamentation in energy that is controlled by electron–electron interactions between trapped electrons and band electrons. The model thus derived is implemented within a state-of-the-art simulator. An analytical version of the model is also derived and is useful for discussing the snapback behavior and the scaling properties of the device.

Sommario

Lo sviluppo dei sistemi di memoria di futura generazione è guidato principalmente dalla ricerca di una tecnologia universale in grado di superare quelle attuali in ogni loro specifica di funzionamento, dalla ritenzione di dato alla velocità di accesso, migliorando la durata e riducendo nel contempo il dispendio energetico.
Le memorie costituiscono una parte vitale per tutti i dispositivi elettronici moderni, il cui sviluppo ha portato alla creazione di processori in grado di elaborare quantità di dati sempre più ampie, tali da costringere ad una riorganizzazione della gerarchia delle memorie, divenute l'attuale limite in termini di velocità di calcolo per le odierne CPU, a partire dai dischi rigidi, ovvero gli attuali componenti di memoria più lenti ancora in uso.
Il sottosistema delle memorie assorbe una parte significativa delle risorse del macro sistema costituito dal calcolatore, sia in termini di costi che di potenze dissipate, tanto da aver quasi raggiunto il limite tecnologico nel caso delle odierne memorie di tipo DRAM. Al fine di risolvere tale problematica, le industrie hanno focalizzato la loro attenzione nello sviluppo dei dispositivi Flash e nelle ricerca di nuove soluzioni in grado di superare i limiti imposti dall'attuale tecnologia basata su transistor a *gate* flottante. Tra queste, la più promettente sembra essere quella delle memorie a cambiamento di fase (PCM), in grado di colmare anche i limiti mostrati dalla tecnologia Flash nell'ambito della durata e scalabilità.
Inoltre questa tecnologia alternativa di memorie non volatili, che sfrutta la differenza di resistenza apprezzabile in determinati materiali in grado di cambiare fase, offre una densità di implementazione delle singole celle in grado di superare anche quella dei dispositivi DRAM ad elevate prestazioni, aprendo lo scenario a futuri sistemi ad elevata capacità di immagazzinamento dei dati pur mantenendo costanti i costi e l'energia dissipata.
I materiali che consentono di realizzare dispostivi a cambiamento di fase pilotato elettricamente appartengono alla famiglia dei calcogenuri. La possibilità di *scaling* di queste future memorie PCRAM risiede nell'acquisizione della tecnologia per controllare il meccanismo di cristallizzazione che, a seguito della riduzione delle dimensione diventa più rapido, come prospettato, ma nel contempo incre-

menta anche la sua instabilità passando da un meccanismo di cristallizzazione inerte ad uno di cristallizzazione eterogenea.
Tra i diversi composti calcogenuri quello attualmente identificato come soluzione di maggiore interesse per applicazioni industriali è il $Ge_2Sb_2Te_5(GST)$.
Il trasporto di carica all'interno di dispositivi di memoria realizzati con tali materiali è stato modellato considerando l'azione di due contributi differenti: *hopping* di cariche intrappolate e moto di elettroni liberi in stati estesi. Il GST mostra un comportamento elettrico pressoché Ohmico in fase cristallina mentre, in fase amorfa, risulta essere poco conduttivo per basse correnti fino al superamento di una tensione di soglia oltre la quale si assiste al passaggio da uno stato altamente resistivo ad uno altamente conduttivo, caratterizzato da un andamento a resistenza differenziale negativa (NDR).
L'accurata interpretazione di tale fenomeno costituisce una fase fondamentale non solo per la comprensione del trasporto di carica in questo tipo di materiali ma anche per la valutazione di tali composti nella fabbricazione di memorie non volatili innovative.
Il meccanismo retroattivo che induce il fenomeno di *snapback* viene descritto come filamentazione in energia controllata dalle interazioni tra elettroni liberi ed elettroni intrappolati. Il modello fisico ricavato è stato implementato all'interno di un simulatore di dispositivi di ultima generazione ed è stato in seguito riprodotto in una versione analitica semplificata in grado, però, di permettere una prima analisi del comportamento elettrico del dispositivo e delle sue proprietà di *scaling*.

Introduction

Current computer systems consist of several cores on a chip, and sometimes several chips in a system. As the number of cores in the system increases, the number of concurrently running applications (or threads) increases, which in turn increases the combined working set of the system. The memory system must be capable of supporting this growth in the total working set. For several decades, DRAM has been the building block of the main memories of computer systems. However, with the increasing size of the memory system, a significant portion of the total system power and the total system cost is spent in the memory system. For example, Lefurgy et al. reported that in a commercial server equipped with 16 processors and 128 GB main memory (e.g., IBM eServer machine), the processors are responsible for only 28% of the entire energy consumption while the memory for 41% [47].
Therefore, technology researchers have been studying new memory technologies that can provide more memory capacity than DRAM while still being competitive in terms of performance, cost, and power [63].
Two promising technologies that fulfill these criteria are Flash and Phase Change Memory(PCM). Flash is a solid-state technology that stores data using memory cells made of floating-gate transistors. PCM stores data exploiting the property of chalcogenide glass to switch between two states, amorphous and crystalline, with the application of heat using electrical pulses. While both Flash and PCM are much slower than DRAM, they provide superior density relative to DRAM. Therefore, they can be used to provide a much higher capacity for the memory system than DRAM within the same budget.
Chalcogenide-GST materials (e.g., $Ge_2Sb_2Te_5$) can suitably be exploited for manufacturing phase-change memory devices [13]. The principle of chalcogenide memory was first proposed in the late 1960s by Ovshinsky [55]. While crystalline GST exhibits an almost ohmic $I(V)$ curve, amorphous GST shows high resistance at low biases, whereas, above a threshold voltage V_{th}, transition takes place from a highly resistive to a conductive state. The transition is characterized by a swift rise in the current, along with a voltage snapback, leading to an S-shaped $I(V)$

curve. Such a behavior is sketched in Fig. 1. It is useful to remind that the device is current driven, so the experiments actually yield one-valued N-shaped $V(I)$ curves. The difference in resistance between the two states is typically about five orders of magnitude and can be used to infer logical states of binary data.
Explaining the negative differential resistance of the device is of utmost importance for exploiting the chalcogenide materials in the fabrication of alternative nonvolatile memories. In fact, such an explanation provides the tool for modeling the threshold behavior, the low-current temperature dependence, the geometrical scaling properties of the device, and other important design properties.
In the last years, different interpretations of the voltage snapback effect have been given in the literature. In the frame of a band-gap model for electric conduction in amorphous- GST materials, the switching mechanism has been related to the competing role of impact ionization and recombination. An alternative interpretation based on trap-limited conduction indicates the field-assisted hopping and the spatial non-uniformity of the electric field due to carrier heating as the effects mainly responsible for the snapback behavior [32],[31].
The analysis of the negative differential resistance and its dependence on the devices physical and geometrical parameters is open to further contributions. This paper examines some aspects of the problem, starting from the relation between the snapback effect and a number of generation–recombination phenomena. The model that is worked out is a generalization of that presented in [12], where only the hopping processes through localized states, due to a combination of tunneling and thermal excitation, were considered. As the initial and final states of the hopping processes belong to a trap, the electrons involved are termed trap electrons. Here, the transport model is enriched by considering a second contribution to conduction due to the electrons occupying extended states (termed band electrons), acting in parallel to the contribution of the hopping processes of the trap electrons. Although the band electrons have a much higher mobility than the trap electrons, the difference in mobility is not sufficient to explain the negative differential resistance. The latter requires the occurrence of a specific feedback mechanism inside the device, which is analyzed by combining the difference in mobility with the sharpness of the extraction mechanism responsible for the trap-to-band transitions of the electrons.
In addition to phonon absorption, the possible extraction mechanisms are those due to the electric field (impact ionization and field emission), and a cooperative effect of the band electrons that act onto the trap electrons through electronelectron interactions. The third effect is similar to impact ionization but requires much lower energy of the band electrons. As the average electric field within the device strongly decreases when snapback occurs, a feedback due to impact ionization and/or field emission would not be able to provide a negative differential resistance. As a consequence, the snapback effect cannot be ascribed entirely to

the intensity of the electric field acting on the trapped electrons. The cooperative effect previously cited is instead a good candidate to explain the negative differential resistance. It will also be shown that the intensity of the field plays a role anyhow, because it enhances the trap electron mobility in the subthreshold region.

The model explains the snapback event, even in the simple case in which the device is 1-D and spatially uniform. It provides macroscopic equations based on a few parameters and, as shown below, lends itself to fitting experimental data and to incorporating the equations into commercial simulation tools. Part I describes the main parameters used for the description of transport and provides the macroscopic models for the generation–recombination mechanisms. Part II illustrates the simplified analytical model of the device implemented into a state-of-the-art device simulator: the feedback mechanism is analyzed and validated against experiments.

Part I

VOLTAGE SNAPBACK IN AMORPHOUS-GST MEMORY DEVICES

Chapter 1

Structural Characterization

The idea of phase-change recording, as suggested by Ovshinsky [55], is based on the differences in electrical and optical properties between amorphous and crystalline phases of Te-based chalcogenides for data storage. The process of phase-change recording is quite simple.
When a melt is cooled down slowly, such that the structure always remains in thermal equilibrium, upon reaching the crystallization temperature the material crystallizes, i.e. is transformed into a solid state with a well-defined periodic structure. If, on the other hand, the cooling rate is fast, then at a certain temperature the viscosity of the liquid increases to a degree such that the structure can no longer relax following the changes in temperature; one obtains a supercooled liquid and then a glass. In contrast to the crystallization temperature, the glass-transition temperature is not well defined. A range of temperatures exists and the particular temperature of the glass transition depends on the cooling rate.
Once in the solid state, the glass, if kept at a temperature close to the glass-transition temperature, crystallizes. On the other hand, rapid heating of the crystalline material to a temperature above the melting point and subsequent rapid cooling (quenching) can produce a glassy state. This glass-formation diagram is demonstrated by figure 1.1, where T_g is the glass-transition temperature and T_m the melting point.
The material can also be heated by light. Exposure of an amorphous material to a laser light (or an electrical heater) that heats it above the glass-transition temperature results in crystallization while short and intense laser pulses melt the material and (provided the heat-dissipation rate is fast enough) an amorphous recorded bit is formed. An ideal tool to investigate the local structure of a material and its changes on the atomic scale independent of the state of the material (crystalline or amorphous) is X-ray absorption fine-structure (XAFS)

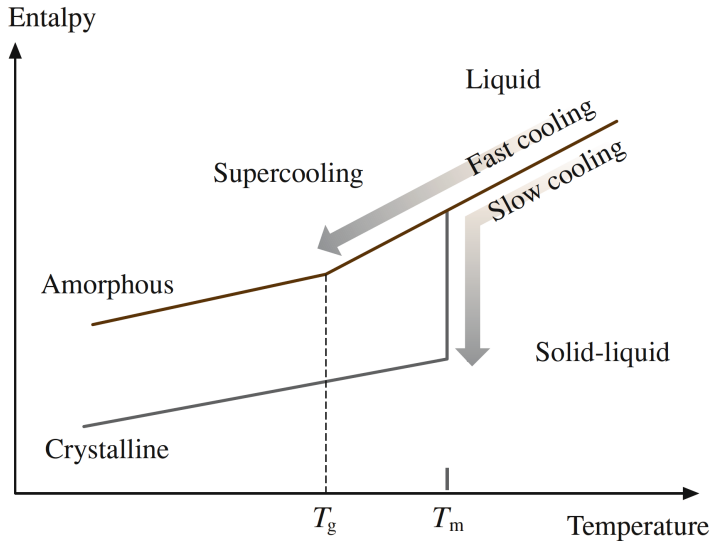

Figure 1.1: Schematic description of the phase-change process in chalcogenide materials.

spectroscopy.
Extended X-ray absorption fine structure (EXAFS) allows one to obtain information about the local structure around selected chemical species, such as the average coordination number, the bond lengths, the chemical nature of the neighboring species, as well as the bond-length disorder parameter, or mean-square relative displacement (MSRD). The technique is selective to the absorbing atom, which allows one to probe the local structure around different constituent elements independently.
X-ray absorption near-edge structure (XANES), which involves multiple scattering, additionally allows one to probe the local arrangement of atoms on a scale somewhat beyond the first-nearest neighbors, in particular, it is sensitive to the mutual arrangement of the neighboring atoms in space, i.e. includes bond-angle information. As XANES features are also a consequence of transitions from occupied core states to unoccupied conduction-band states, the spectra also contain information about the density of unoccupied conduction-band states. It is worth mentioning that recent advances in theory have made it possible to simulate EXAFS and XANES spectra with good accuracy [5].

1.1 Crystalline State

The stable crystal structure of GST is hexagonal [76, 53, 58]. Thin films, however, crystallize into a different structure. Recent X-ray diffraction (XRD) studies have lead to a conclusion that thin GST layers crystallize into the rock-salt structure with Te atoms occupying sites on one face-centered cubic (fcc) sublattice with Ge

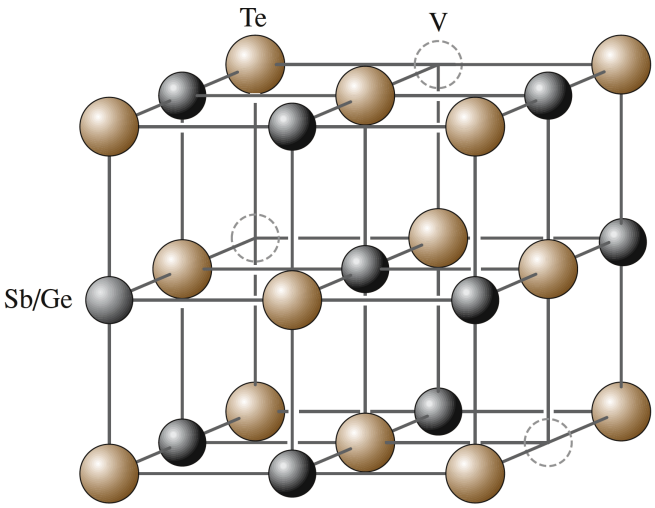

Figure 1.2: Schematic chemical structure of metastable crystalline Ge–Sb–Te as reported by X-ray diffraction measurements.

and Sb randomly forming the other fcc sublattice (20% of the sites being vacant) (Fig. 1.2). A lattice parameter of 6.02 Å was reported. The isotropic atomic displacements B_0, which is a measure of atomic displacements from the ideal crystallographic positions due e.g. to thermal vibrations, found via the fitting pro- cess were 1.2 $Å^2$ and 3.2 $Å^2$ for the Te, and Ge(Sb) species, respectively, which correspond to atomic dis- placements of 0.1 Å and 0.2 Å for the Te and Ge(Sb) species, respectively.

It was suggested that the cubic structure of GST (which is rather isotropic and hence more similar to the amorphous structure than any other crystal structure) was the reason for the high-speed switching and stable performance.

Here, the recent efforts to investigate the local structure of GST using XAFS are summarized. Measurements were performed at BL12C at the Photon Factory (Tsukuba, Japan) and BL01B1 at SPring8 (Hyogo-ken, Japan). The Fourier-transformed (FT) spectra for the Ge and Te edges of GST are shown in figure 1.1. It should be noted that the r -space data shown in figure 1.1 are not real-space radial distribution function data but the magnitude of the Fourier transforms (FTs) of the k-space EXAFS data. The peak positions in the figure are shifted from the actual interatomic distances toward lower r because of the photoelectron phase shift $\delta(k)$ in the phase factor of the EXAFS oscillations. The spectra measured at the Sb edge did not show any significant variation between the two states and are not shown here. Details of the data analysis can be found elsewhere [40]. The main results for crystalline GST are summarized below. Two types of bond lengths exist, namely shorter bonds and longer bonds for both Te–Ge and

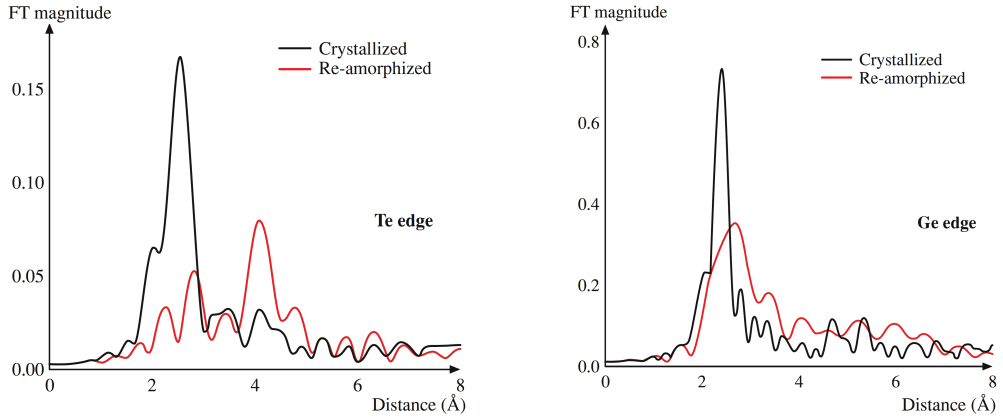

Figure 1.3: Fourier-transformed Ge and Te K-edge EXAFS spectra of Ge2Sb2Te5 measured for both the crystalline and amorphous states

Te–Sb (for Te–Ge: 2.83 ± 0.01 Å , and 3.2 ± 0.3 Å and for Te–Sb: 2.91 ± 0.01 Å and 3.2 ± 0.3 Å). It should be noted here that the observation of splitting of the bond lengths into two groups is very similar to the case of GeTe. The uncertainties for the longer bonds are rather large. For this reason no definitive conclusions could be drawn about the longer bonds. Thus, what follows shall exclusively concentrates on the shorter bonds. It should be noticed here that another commercially used material, AIST, also possesses subsets of shorter and longer bonds.

No Sb–Ge bonds were detected, in agreement with the fact that Sb and Ge do not intermix in the solid phase but a second-nearest-neighbor Te–Te peak at 4.26 Å has been clearly observed.

It is worth noting that the mean-square relative displacements (MSRD) of the Te–Ge bond length obtained in EXAFS are considerably lower (0.02 $Å^2$) than the isotropic atomic displacements of single atoms obtained from XRD (0.04 $Å^2$). This result demonstrates that Ge and Sb atoms do not deviate from the ideal rock-salt positions in a random way but in a strongly correlated manner with respect to the neighboring Te atoms, i. e. the crystalline structure is in fact a distorted rock-salt-like structure similar to the case of the ferro-electric GeTe. The off-center location of the Ge atoms means that there is a net dipole moment and suggests that GST is a ferroelectric material.

1.2 Amorphous State

It was found that both Te–Ge and Te–Sb bonds get shorter (2.61 Å and 2.85 Å respectively) and stronger upon amorphization, as evidenced by figure 1.1. At the same time, the Te second-neighbor peak becomes considerably weaker but does not disappear completely. The MSRD value de- creases from 0.02 $Å^2$ in the

crystalline state to 0.008 $Å^2$ in the amorphous state. Such a behavior is highly unusual for typical three- dimensional covalently bonded solids as, due to the anharmonicity of interatomic potentials, disordering typically results in an increase of the bond lengths and the bond-length disorder. The obtained results reminds one of the case of molecular solids where the presence of intermolecular and intramolecular bonds determines the crystallization–amorphization behavior. In the current case, a bond-strength hierarchy also exists and the following model of structural re- arrangement can be envisaged. Upon melting, the longer Te–Ge (and Te–Sb bonds) are broken and, as a result, the shorter bonds become even shorter and stronger, i.e. the amorphous phase is locally more ordered than the crystalline phase. Raman scattering experiments provided further grounds for this model, namely, the Raman measurements for both GeTe and GST showed that the spectra for the crystalline films are dominated by a peak located at lower wavenumbers, i.e. "mode softening" takes place upon crystallization. This situation can be compared with the case of Se or Te when the interchain interaction is weakened, giving rise to a Raman peak located at higher wave number. It should be mentioned that an increased local bond order in the amorphous phase was also observed for selenium.

To get further insight into the structure of the amorphous phase XANES simulations have been performed, founding that the best agreement with experiment is obtained when Ge is allowed to acquire its preferred tetrahedral surrounding in the amorphous phase. This structural transformation is illustrated in fugure 1.4 where a Ge atom is shown within the fcc sublattice formed by Te atoms. The Ge atoms occupy octahedral and tetrahedral symmetry positions in the crystalline and amorphous states, respectively. The stronger covalent bonds are shown with thicker lines than the weaker bonds (Fig. 1.4 left). An intense laser pulse induces rupture of the weaker bonds and the Ge atom flips into the tetrahedral position (Fig. 1.4 right). An alternative description of the structural transforma-tion upon melting is an umbrella-flip distortion resulting in disordering of the Ge sublattice. Notice, that the three covalent bonds remain intact. This conservation of the system of stronger covalent bonds is crucial: the material is not molten in a conventional sense.

Support for the aforementioned transformation comes from an estimate of the Ge–Te distance from the crystallographic data. Using a lattice parameter of GST obtained by X-ray diffraction, the Ge–Te distance (the Ge atoms being in a tetrahedral symmetry position) can be easily calculated to be 2.61 Å , i.e. exactly the value obtained from the EXAFS analysis. This consistency between the results obtained using two different structural techniques is the ultimate proof of the suggested structural modification as well as the generality of the structural modification in GeTe-based alloys.

It is interesting to note that very similar bond lengths for the crystalline and

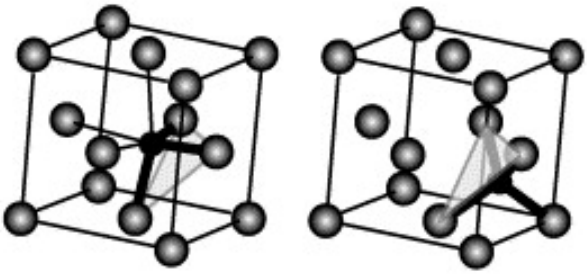

Figure 1.4: Structural modification of GST upon transformation from the crystalline (left) to amorphous (right) state.

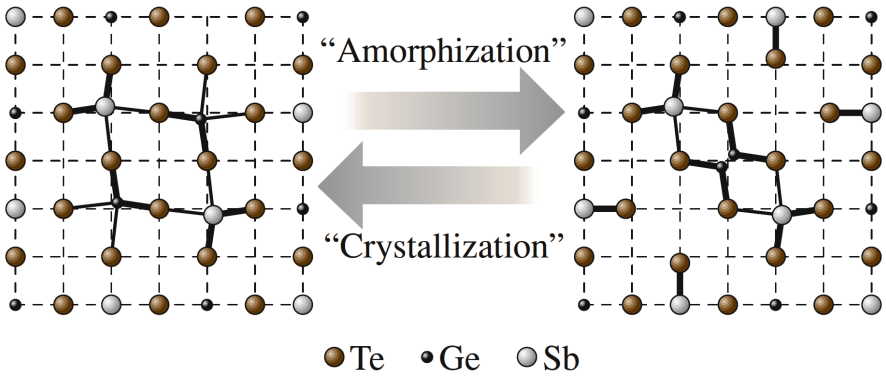

Figure 1.5: Intermediate-range-order crystallization–amorphization transition upon changes in GST.

amorphous states were also observed for the binary GeTe, indicating that it is the GeTe component of the quasibinary GeTe–Sb_2Te_3 that is mainly responsible for the observed phase transition.
Sb-edge XANES does not exhibit any significant changes upon amorphization (except for the Sb–Te bond shortening) implying that the local arrangement of atoms around Sb remains essentially unchanged in accordance with the above model. These results suggest that the Sb atoms mainly play the role of enhancing overall stability of the metastable crystal structure by participating in the overall electron balance.

1.3 Intermediate Structure Changes

The structural change on an intermediate-range-order scale can be viewed as illustrated in figure 1.5. After rupture of the weaker Ge–Te bonds the Ge atoms flip into the tetrahedral symmetry position forming the $GeTe_4$ tetrahedra. At the same time, the broken weaker Ge–Te bonds no longer counterbalance the Sb–Te

bonds on the opposite site and, as a result, the Sb–Te bonds become structure-determining.
The structure relaxes making the Sb–Te bonds shorter (just as in amorphous Se the intrachain bonds get shorter upon amorphization). The Sb–Te bond shortening upon amorphization has indeed been observed experimentally [40]. This can be interpreted as the local phase separation into GeTe and Sb_2Te_3 phases. Finally, the structure relaxation causes a distortion in the Te fcc sublattice. The well-defined local (single-state) structure, without long-range periodicity, of the amorphous state is the reason for the overall stability of the GST-based optical media.

Chapter 2

Transport Mechanism

Chalcogenide materials have recently been regarded as the most promising for implementing next-generation memory due to their ability to repeatedly transform between glassy (disordered) and crystalline (ordered) atomic structures. Thus, in a chalcogenide memory cell, the data can be stored in a flat chalcogenide layer, applying heat onto nanoscale memory grain. For example, optical memory disks use laser light to convert small portions of a thin chalcogenide film between the high and low reflective states. On the other hand, phase change memory (PCM) uses a voltage bias to convert the material between the high and low resistive states. PCM stores data in a smaller area and with higher speeds for both read and write processes than the optical memory disks.

PCM is an emerging nonvolatile memory technology with the capability of random access memory, it is sometimes referred as unified memory. Applications explored for this technology span from wireless, embedded systems [41] to solid state storage, [15] automotive, and space applications. Most recently, usage of PCM in computer applications was suggested as Storage Class Memory (SCM) [10].

Large, up to 1 gigabyte, memory arrays with PCM elements have been demonstrated for 180 nm, [8] 90 nm, [54, 57] and 45 nm [68] technology nodes. In PCM, each individual element is in series with an access/selector device. Both MOS-based and BJT/diode-based selectors have been integrated with PCM.

Recently, PCM was integrated with a chalcogenide based thin film selector to form PCMS arrays, opening a path for 3D stackable cross point phase change memory. Understanding and optimizing the material properties of chalcogenide nanoglasses in PCMS cells is a key enabler for this promising nonvolatile memory technology [34].

The operation of PCM depends on charge transport in their constituent inclu-

sions of chalcogenide glasses. When the device is in the reset state, the electrical conduction can be non-ohmic under practical voltages and temperatures. This non-ohmicity provides a way of supplying energy to the device faster than ohmic conduction and it needs to be properly understood in order to improve future device parameters. The goal of this chapter is to recall the established physics of chalcogenide glasses and convey a broad picture of different mechanisms that are relevant to the problem of non-ohmic conduction in these materials, providing a starting point for the additional studies that are required to better understand charge transport in PCM glasses.

The commonly observed non-linear current-voltage (IV) characteristics (above $\sim 10^3 - 10^4$ V/cm) are often attributed to the Poole-Frenkel (PF) effect after the classical work [30, 26, 62] suggesting their plausible interpretation. An experimental signature of PF conduction is a region of linearity in the plot of $\ln(I/I_0)$ vs. either $\sqrt{V}$ or V where I_0 is the pre-exponential factor. The underlying mechanism is commonly related to the field-induced increase in free carrier concentration, as reflected in [16, 43, 9, 74] (except Refs. [32, 31], which proposes hopping conduction).

Although there is general agreement about the observed PF-type of non-ohmicity and the fact that $I_0 \propto \exp(-E_a/kT)$, where E_a is the activation energy, k is the Boltzmann constant, and T is the ambient temperature, particular features observed and especially their interpretations vary dramatically between researchers. Some of them present the observed non-ohmicity as $\ln(I/I_0) \propto \sqrt{V}$ (e.g. Refs. [67, 16]) , while others describe their observations as $\ln(I/I0) \propto V$ (e.g. Refs. [43, 74, 32, 38, 3]). Furthermore, some of the latter articles ([38, 3]) point at two different domains in the IV data which exhibit different proportionality coefficients and temperature dependencies.

2.1 Survey of Conduction Mechanisms

Although the literature on transport phenomena in disordered materials is enormously rich, there are still many open questions in this field due to various problems specific to such materials. In contrast to ordered crystalline semiconductors with well-defined electronic energy structures consisting of energy bands and energy gaps, the electronic energy spectra of disordered materials can be treated as quasi-continuous. Instead of bands and gaps, one can distinguish between extended and localized states in disordered materials. In an extended state, the charge carrier wavefunction is spread over the whole volume of a sample, while the wavefunction of a charge carrier is localized in a spatially restricted region in a localized state, and a charge carrier present in such a state cannot spread out in a plane wave as in ordered materials. Actually, localized electron states are known in ordered systems too. Electrons and holes can be spatially localized

when they occupy donors or acceptors or some other impurity states or structural defects in ordered crystalline materials. However, the localized states usually appear as δ-like discrete energy levels in the energy spectra of such materials. In disordered semiconductors, on the other hand, energy levels related to spatially localized states usually fill the energy spectrum continuously. The energy that separates the extended states from the localized ones in disordered materials is called the mobility edge. To be precise, we will mostly consider the energy states for electrons in the following. In this case, the states above the mobility edge are extended and the states below the edge are localized. The localized states lie energetically above the extended states for holes. The energy region between the mobility edges for holes and electrons is called the mobility gap. The latter is analogous to the band gap in ordered systems, although the mobility gap contains energy states, namely the spatially localized states. Since the density of states (DOS), defined as the number of states per unit energy per unit volume, usually decreases when the energy moves from the mobility edges toward the center of the mobility gap, the energy regions of localized states in the vicinity of the mobility edges are called band tails. We would like to emphasize that the charge transport properties depend significantly on the energy spectrum in the vicinity and below the mobility edge (in the band tails). Unfortunately this energy spectrum is not known for almost all disordered materials. A whole variety of optical and electrical investigation techniques have proven unable to determine this spectrum. Since the experimental information on this spectrum is rather vague, it is difficult to develop a consistent theoretical description for charge transport ab initio. The absence of reliable information on the energy spectrum and on the structures of the wavefunctions in the vicinity and below the mobility edges can be considered to be the main problem for researchers attempting to quantitatively describe the charge transport properties of disordered materials.

There are several additional problems that make the study of charge transport in disordered materials more difficult than in ordered crystalline semiconductors. The particular spatial arrangements of atoms and molecules in different samples with the same chemical composition can differ from each other depending on the preparation conditions. Hence, when discussing electrical conduction in disordered materials one often should specify the preparation conditions. Another problem is related to the long-time relaxation processes in disordered systems. Usually these systems are not in thermodynamic equilibrium and the slow relaxation of the atoms toward the equilibrium arrangement can lead to some changes in electrical conduction properties. In some disordered materials a long-time electronic relaxation can affect the charge transport properties too, particularly at low temperatures, when electronic spatial rearrangements can be very slow. At low temperatures, when tunneling electron transitions between localized states dominate electrical conduction, this long-time electron relaxation can significantly

affect the charge transport properties.
In this section DC conduction in chalcogenide glasses has been analyzed, indicating the shortcomings in the current state of understanding, and suggesting avenues for further investigation. A brief overview of the pertinent experimental data to provide some context for the key observations will be presented, followed by a review of the physics of localized states that underlies the unique properties of chalcogenide glasses. This section will provide a survey of conduction mechanisms that may explain the observed non-ohmic IV data, including: 1) the original Poole-Frenkel mechanism; 2) Schottky decrease in interfacial barrier near device electrodes; 3) field-induced delocalization of shallow band tail states near the mobility edges; 4) space charge limited (injection) currents; and 5) field effects in hopping conduction. Here, the possible mechanisms of DC conduction in chalcogenide glasses will be discussed, including bulk materials and thin films down to the nanometer scale. Finally, the summary of the candidate mechanisms will be followed by the discussion of their validity and implications, along with new indicative facts that are required to further evaluate these mechanisms.

Table 2.1: Table of conduction mechanisms along with the related analytical expression and estimated field range of applicability. The current I is given in terms of the electric field $\mathcal{E}$, with the pre-exponential $I_0 \propto (-E_a/kT)$.

Mechanism	$\mathbf{\ln(I/I_0)}$	**Field Range (V/cm)**
Poole-Frenkel 1-center activation	$\frac{2}{kT}\sqrt{\frac{q^3\mathcal{E}}{\epsilon}}$	$10^4 - 10^5$
Poole-Frenkel 2-center activation	$\frac{aq\mathcal{E}}{kT}$	$< 10^4$
Poole-Frenkel 1-center tunneling	$\frac{\hbar q^2\mathcal{E}^2}{3m}\left(\frac{1}{kT}+\frac{1}{kT_{\rm ph}}\right)^2$	$> 10^5$
Schottky emission	$\frac{1}{kT}\sqrt{\frac{q^3\mathcal{E}}{kT}}$	N/A
Delocalization of tail states	$\left(\frac{\hbar q\mathcal{E}}{\sqrt{m}}\right)^{2/3}\left(\frac{1}{kT}-\frac{1}{E_0}\right)$	$\sim 10^5$

Continued on next page

Table 2.1 – continued from previous page

Mechanism	$\ln(I/I_0)$	**Field Range (V/cm)**
Space-charge limited currents	$\frac{\epsilon\mathcal{E}}{2\pi Lqgk T}$	$\sim 10^4$
Optimum channel hopping (thin films)	$-\sqrt{\frac{8L\lambda}{\alpha}} + 1.6\sqrt{\frac{q\mathcal{E}L}{kT}}$	$< \frac{E_F}{qL}$
Optimum channel field emission	$-\sqrt{\frac{8\lambda E_F}{\alpha q\mathcal{E}}}$	$\gg \frac{E_F}{qL}$
Percolation band conduction	$\eta\sqrt{\frac{L_c q\mathcal{E}}{kT}}$	$> 10^4$
Percolation band conduction in thin films ($L < L_c$)	$\eta\sqrt{\frac{L_c q\mathcal{E}}{kT}} + \frac{L_c - L}{2r_c}\left[\ln\left(\frac{2V_{\max}r_c}{kTL}\right) + 1\right]$	$> 10^4$
Crystalline inclusions – I	$\frac{2\epsilon}{kT}\sqrt{\left(\frac{r_x\Delta}{q}\right)^3\mathcal{E}}$	$10^5 - 10^6$
Crystalline inclusions – II	$\frac{\epsilon r_x^2\mathcal{E}\Delta}{qkT}$	$< 10^5$

The parameters are defined as follows: k is the Boltzmann constant, T is the temperature, q is the elementary charge, ϵ is the dielectric constant, a is the inter-center distance, $\hbar$ is the reduced Plancks constant, m is the effective carrier mass, $kT_{\text{ph}} \sim 0.01 - 0.03$ eV is the characteristic phonon energy, $g = g_0 \exp(-E/E_0)$ represents the characteristic decay of the density of tail states dependent on E_0, where E is the energy, L is thickness, $\lambda \approx -\ln(g_0 kTaL^2) \gg 1$ (here, g_0 is the density of localized states), α is the electron localization radius, E_F is the Fermi energy, $\eta \sim 1$ is a numerical factor, $L_c \sim 10$ nm is the percolation cluster correlation radius, r_c is the order parameter, r_x is the crystallite radius, $V_{\max}$ is the maximum percolation transport barrier, and $\Delta \sim 0.4$ eV is the band offset between crystalline and amorphous phases.

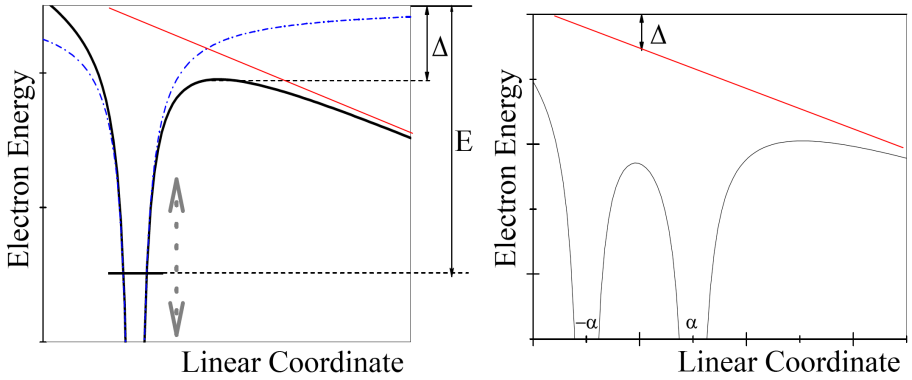

Figure 2.1: Left: Schematic illustration of the field induced decrease δ in activation energy of a coulombic center. Dashed lines show zero field case, tilted red line represents the electric potential of a uniform field. Gray arrow shows vibration of the electron energy E due to electron-phonon coupling. Right: Field induced decrease δ in activation energy of a pair of coulombic centers

2.1.1 Poole-Frenkel Effect

The originally suggested physics of the PF effect is the decrease in the ionization energy of a single coulombic potential well in the direction of an applied field (explaining $\ln I \propto \sqrt{V}$) or that of a pair of coulombic centers (explaining $\ln I \propto V$), as schematically illustrated in figure 2.1.1. The corresponding barrier change δ increases the center ionization rate, proportional to which are the free carrier concentration and the activated electric current $I/I_0 \propto \exp(\delta/kT)$. The underlying assumption of a coulombic attractive potential is justified by its ability to give the required decrease in the ionization energy $\delta \propto \mathcal{E}$ or $\delta \propto \sqrt{\mathcal{E}}$. It is worth noting that as originally proposed [34, 30], this mechanism was meant to explain the data on noncrystalline materials. Surprisingly, the data on non-ohmic conduction in doped crystalline semiconductors are typically described by other dependencies [2], despite the fact that the coulomb nature of the defects therein is well established. Therefore, the empirically observed relevance of PF-type dependencies to noncrystalline materials may suggest that their nature is more related to disorder effects rather than individual or pairs of coulomb centers. From that point of view, the PF mechanism may be significantly over-emphasized.
For the case of two centers separated by distance $2a$ in the electric field of strength $\mathcal{E}$, the electron energy along the axis is given by

$$U(x) = -\frac{q^2}{\epsilon(a-x)} - \frac{q^2}{\epsilon(a+x)} - \mathcal{E}qx\,, \tag{2.1}$$

where q is the electron charge and ϵ is the dielectric permittivity. The position of the lowest barrier maximum, $\mathrm{d}U/\mathrm{d}x = 0$ is determined from the equation

$$\widetilde{x} = \widetilde{\mathcal{E}}\left(\widetilde{x}^2 - 1\right)^2 \qquad \text{where} \quad \widetilde{x} = \frac{x}{a}, \quad \widetilde{\mathcal{E}} = \frac{\mathcal{E}}{q/4a^2\epsilon}\,. \tag{2.2}$$

The original PF result $x = \sqrt{q/\epsilon\mathcal{E}}$, $\delta = \sqrt{4q^3\mathcal{E}/\epsilon}$ follows from Eqs. 2.1 and 2.2 when $\widetilde{\mathcal{E}} \gg 1$ (i.e. $F \gg q/4\epsilon a^2$); however, it remains approximately valid numerically even at $\widetilde{\mathcal{E}} = 1$. The characteristic field is $q/4a^2\epsilon \sim 10^4$ V/cm for the typically assumed [51, 32, 31] center concentration of $\sim 10^{18}\mathrm{cm}^{-3}$.

In the opposite limiting case of 'weak' fields, $\mathcal{E} \ll q/4\epsilon a^2$, Eqs. 2.1 and 2.2 yield $x = a$ and $\delta = q\mathcal{E}a$, corresponding to the so called modified PF effect with $\ln(I/I_0) \propto V$ emphasized in Ref. [32, 31].

The critical field $q/4\epsilon a^2$ also implies that the notion of 'weak' or 'strong' fields can be replaced by condition of low or high defect density (as related to a). Thus, for a given field, the PF effect is dominant for a high defect concentration while the modified PF effect pertains to a low defect concentration. In any event, it has been observed that significant deviations from the standard PF results can be expected under low fields $\mathcal{E} \ll 10^4$ V/cm. This significantly narrows the application of the modified PF mechanism in Refs. [32, 31] and [46], also ruling out its role in the switching field region of $\mathcal{E} \gtrsim 10^5$ V/cm.

The two-center model that predicts $\ln(I/I_0) \propto V$ remains critically vulnerable to effects of fluctuations. It is worth noting in this connection that the work in Refs. [32, 31] and [46] was limited to a system of equidistant coulombic centers. Random fluctuations in their concentration (present in all systems of centers in solids so far explored) will generate random variations of activation energies translating into exponentially broad distributions of ionization rates; variations in center energies will make this distribution even broader. This results in local carrier concentrations that vary exponentially between different locations. A proper framework for analyzing these types of systems would be percolation theory [71], which is yet to be applied to PF-type conduction (cf. however Ref. [39]).

Quantum tunneling imposes limitations on the activation PF effect. The corresponding analysis by Hill [30] neglects the role of atomic vibrations on tunneling. A more recent analysis [2] that accounts for electron-phonon interactions results in a picture where the electron energy level moves up and down following oscillations of the atomic system to which it is coupled. As a result, the electron tunneling becomes most likely when the electron energy is significantly above its average position (Fig. 2.1.1), and the chief exponential term in non-ohmic current can be written as follows

$$\ln(I/I_0) = \frac{\mathcal{E}^2 q^2 \hbar}{3\left(kT^*\right)^2 m} \qquad \text{with} \quad \frac{1}{kT^*} = \frac{1}{kT} + \frac{1}{kT_{\mathrm{ph}}}\,, \tag{2.3}$$

where m is the effective mass of a localized charge carrier, which is taken close to the true electron mass for simplicity [45] and kT_{ph} is on the order of the

characteristic phonon energy ($\sim 0.01 - 0.03$ eV).
It was shown [2] that the standard PF results becomes invalid and the effect is better described by Eq. 2.3 when

$$\mathcal{E} > \mathcal{E}_t \equiv \sqrt{\frac{2mE}{\hbar^2}} \frac{kT^*}{q} \left(\frac{kT^*}{E} \right)^{1/3} \quad , \tag{2.4}$$

where E is the ionization energy (≈ 0.4 eV in $Ge_2Sb_2Te_5$). Using the above numerical parameters, one can estimate $\mathcal{E}_t \sim 10^5$ V/cm. The dependence in Eq. 2.3, rather than the standard PF law, was experimentally confirmed for many crystalline semiconductors even for fields below 10^5 V/cm (see Chapter 10 in Ref. [2]).
Overall, we conclude that, for the case of GST glasses, the standard PF expression $\ln(I/I_0) \propto \sqrt{\mathcal{E}}$ can apply in the field range of $10^4 - 10^5$ V/cm. For weak fields, $\mathcal{E} \ll 10^4$ V/cm, the modified PF effect $\ln(I/I_0) \propto \mathcal{E}$ can give a more adequate description, however, the effects of fluctuations in the local concentration of centers must be taken into account. For the high field region, $\mathcal{E} > 10^5$ V/cm, quantum effects lead to $\ln(I/I_0) \propto \mathcal{E}^2$, predicting an increase in non-ohmicity in the vicinity of the switching field. The above boundaries can be numerically different for other chalcogenide glasses; however, the hierarchy of regimes remains the same, as illustrated in figure 2.1.1. Experimental data [29, 69, 14] has exhibited a sharp increase in current when the field is very close to its switching value 3×10^5 V/cm, however, it would be premature at this stage to attribute it to Eq. 2.3. Experimental verification of the temperature dependence in Eq. 2.3 could clarify this issue.

2.1.2 Schottky Emission

The Schottky effect [73] originates from the image force induced lowering of the interfacial energy for charge carrier emission when an electric field is applied. This leads to

$$\ln\left(I/I_0\right) = \frac{1}{kt}\sqrt{\frac{q^3\mathcal{E}}{\epsilon}} \qquad \text{with} \quad I_0 \propto \exp\left(-\Phi/kT\right) , \tag{2.5}$$

where Φ is the interfacial barrier height between the semiconductor and the contact metal.
The dependence in Eq. 2.5 was experimentally verified in the field range $\sim 10^4 - 10^5$ V/cm for various junctions of crystalline semiconductors with metals. However, on empirical grounds, it is hard to believe that it can apply to the case under consideration because of the established $\ln I_0 \propto (-E_a/kT)$, where E_a is half the mobility gap in the chalcogenide material and is independent of contact properties. Some studies reveal that the current is independent of polarity and electrode material, which is additional evidence against the Schottky mechanism [16].

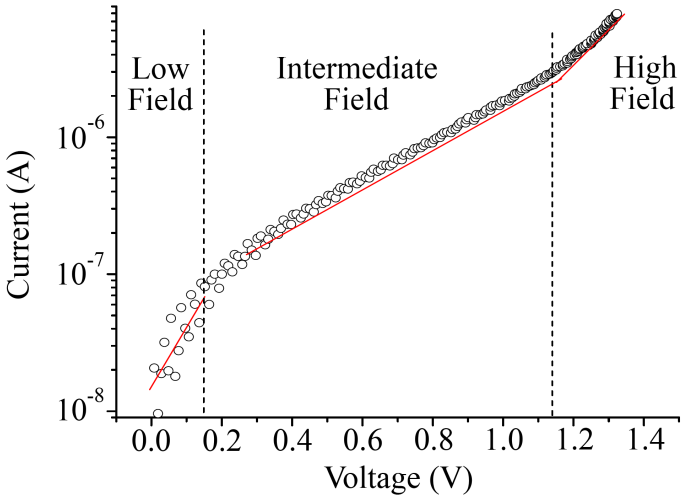

Figure 2.2: The figure shows the three typical regions of the IV characteristic of an unspecified chalcogenide PCM device that is representative of the results discussed in the survey of conduction mechanisms. The low-field region is usually described as ohmic, but in some cases of thin samples it is described as $\ln I \propto V$. The intermediate region has exponential dependence described as either $\ln I \propto V$ and/or $\propto \sqrt{V}$. Near and below room temperature, two slopes are often observed in the intermediate region. The high field region corresponds to a stronger dependence, possibly $\ln I \propto V^2$.

2.1.3 Field-Induced Delocalization of Tail States

Similar to the PF mechanism of decreasing the ionization energies of coulombic centers, the electric field can decrease energies of localized tail states in the mobility gap and even destroy them if they are shallow enough. Transforming localized into delocalized states is tantamount to narrowing the mobility gap; this exponentially increases the free carrier concentration and electric conductivity.
The latter mechanism, suggested in Ref. [44], is specific to noncrystalline materials where the presence of band tails is well established. Tail states are related to intrinsic structural disorder of amorphous materials rather than to any specific defects. The disorder creates microscopic variations in the electric potential generated by different structural units in a material and felt by electrons or holes. Some combinations of these microscopic variations form effective potential wells capable of localizing charge carriers.
It was assumed in Ref. [44] that each fluctuation potential well has the same radius r_0 regardless of the energy of its localized state, thus governed only by the well depth. Correspondingly, the condition of the electric field induced delocalization was given in the form $E < E_D \equiv \mathcal{E} q r_0$. Assuming also a simple phenomenological representation of the density of tail states, $g(E) = g_0 \exp(-E/E_0)$,

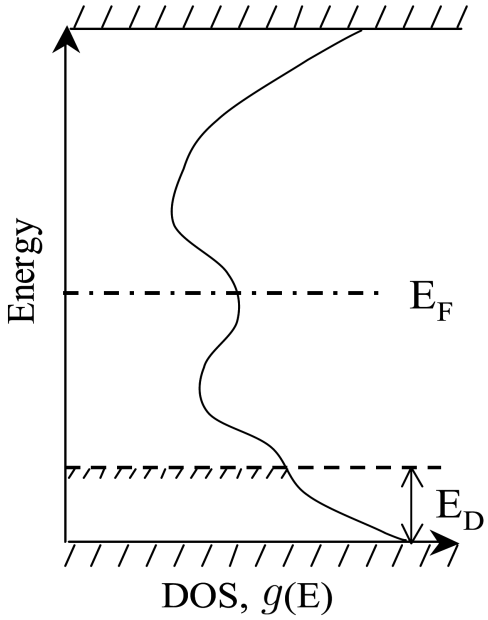

Figure 2.3: Density of states (DOS) in the mobility gap of a chalcogenide glass. The electric field shifts the mobility edge for holes up by energy E_D (similar effect is verified for electrons)

the field-induced increase in concentration of charge carriers becomes $n(\mathcal{E}) \propto g(E_D)\exp(E_D/kT)$, where the first multiplier describes the decrease in activation energy by E_D, as illustrated in Fig. 2.1.3. As a result, the conductivity increases with field as,

$$\sigma(\mathcal{E}) = \sigma_0 \exp\left[\mathcal{E}qr_0\left(\frac{1}{kT} - \frac{1}{E_0}\right)\right], \tag{2.6}$$

where it is assumed that $E_0 > kT$. The observed temperature dependence in Ref. [44] was consistent with that in Eq. 2.6.

The above model could be refined by taking into account that the characteristic size of the localized state of energy E is $\hbar/\sqrt{mE}$ and so is that of its corresponding potential well [49], as illustrated in figure 2.1.3. As a result the condition of delocalization, approximately $\mathcal{E}q\hbar/\sqrt{mE} = E$, gives the characteristic delocalization energy $E_D = (\hbar q\mathcal{E}/\sqrt{m})^{2/3}$ and, similar to Eq. 2.6,

$$\sigma(\mathcal{E}) = \sigma_0 \exp\left[\left(\frac{\hbar q\mathcal{E}}{\sqrt{m}}\right)^{2/3}\left(\frac{1}{kT} - \frac{1}{E_0}\right)\right]. \tag{2.7}$$

This prediction is in a numerically relevant range yielding $E_D \sim 0.1$ eV when $\mathcal{E} \sim 10^5$ V/cm.

Further implementations of the theory of disordered systems [49] calls upon using

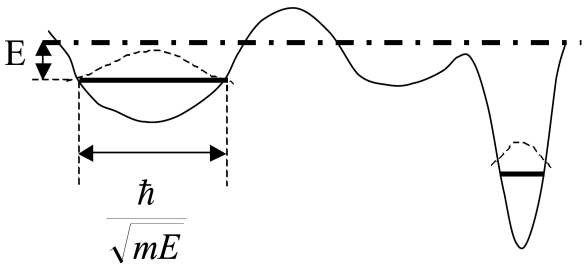

Figure 2.4: Localized tail states for the electrons below the mobility edge (shown as dash-dot line) have linear dimensions decreasing with energy E in the mobility gap.

the density of tail states in the form,

$$g\left(E\right) = g_0 \exp\left[-\frac{E}{E_0}^{\alpha}\right], \tag{2.8}$$

where $\alpha = 1/2$ and $\alpha = 2$ for the cases of uncorrelated and strongly correlated disorder corresponding respectively to the energies $E \ll \hbar^2/mr_c^2$ and $E \gg \hbar^2/mr_c^2$. If the correlation radius r_c is identified with that of the medium range order in a glass [17], then $r_c \sim 1$ nm and $\hbar^2/mr_c^2 \sim 0.1$ eV. Using Eq. 2.8 will obviously modify the results in Eqs. 2.7 and 2.6 without changing them qualitatively.
Overall, it may be very difficult to experimentally discriminate between the shapes predicted by Eqs. 2.7 and 2.6 or their modifications. What is important is that these predictions pertain to a numerically relevant range $E_D \sim 0.1$ eV when $\mathcal{E} \sim 10^5$ V/cm, ensuring strong enough non-ohmicity to explain the observed effects. Also, this model, in contrast to the PF model, gives a natural explanation of why PF-type non-ohmicity ($\ln\left(I/I_0\right) \propto \sqrt{\mathcal{E}}$ or $\mathcal{E}$) is typically observed in glasses rather than in crystalline materials.

2.1.4 Space Charge Limited Current

The exponential current-voltage characteristic can be explained by space charge limited current in a system with almost energy independent density of states [42]. This model is represented in Fig. 2.1.4 in the coordinate and energy spaces. Due to low mobility, the charge carriers accumulate in a system (the logarithm of their density is also shown in Fig. 2.1.4 as the quasi-Fermi level) and create the potential barrier further slowing down their transport. In energy space, charge carriers occupy a layer of certain width δE near the Fermi energy (E_F). Therefore, their charge density is estimated as $\rho = g(E_F)q\delta E$. The corresponding electrostatic potential is $V \approx 2\pi\rho L^2/\epsilon$ where L is the sample thickness. Expressing from here δE through V and taking into account that the activation energy of conduction

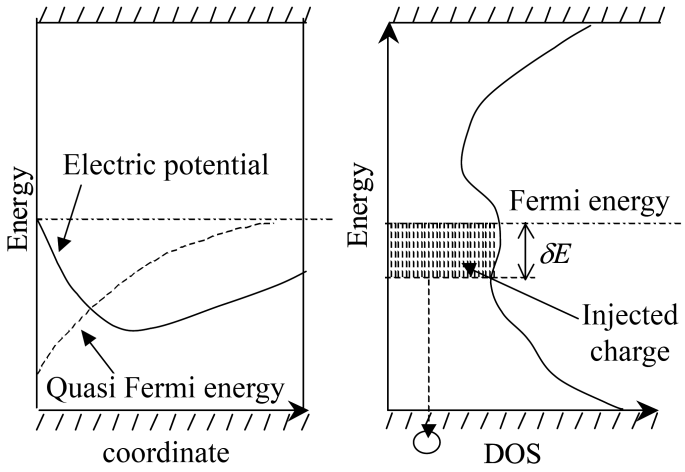

Figure 2.5: Localized tail states for the electrons below the mobility edge (shown as dash-dot line) have linear dimensions decreasing with energy E in the mobility gap.

is by δE lower than in the ohmic regime, one gets

$$\sigma(\mathcal{E}) = \sigma(0) \exp\left(\frac{\mathcal{E}}{\mathcal{E}_0}\right) \qquad \text{with} \quad \mathcal{E}_0 = \frac{2\pi gqLkT}{\epsilon} \tag{2.9}$$

Assuming realistic $g = 10^{17}\text{cm}^{-3}\ \text{eV}^{-1}$ and $L = 100$ nm yields a relevant field scale of the non-ohmicity $\mathcal{E}_0 \sim 10^4$ V/cm; however that scale strongly depends on the system thickness and density of states, which can make $\mathcal{E}_0$ too large and irrelevant to the observed non-ohmicity in some chalcogenide glasses. The explanation of space charge limited current was put forward in Ref. [38] where $\mathcal{E}_0$ linear in L was observed below room temperature. Near and above room temperature, $\mathcal{E}_0$ was found to be thickness independent [38, 65, 14]. This data may suggest that space charge limited transport mechanisms play an important role in thicker samples ($L > 1\mu$m) below room temperature. Additional verifications of the space charge limited mechanism of room temperature conduction in chalcogenide glasses could be obtained from the data on $1/f$ noise measurements. Results show that the corresponding Hooge parameter increases with bias, contrary to what is expected for the space charge limited currents [36].

2.1.5 Hopping Conduction

The intent of this section is not to provide a complete description of hopping conduction, since thorough reviews are available elsewhere [51]. Here, we provide a brief explanation as to why hopping conduction was not observed experimentally in chalcogenide glasses [51, 50].

A high density of localized states g_F at the Fermi level (E_F) in non-crystalline

semiconductors can give rise to hopping transport. The mechanism is based on electronic tunneling ('hops') between localized states that are randomly distributed in real space and energy space [51, 44]. In materials where hopping does occur, it dominates at low temperatures (T) and is described by the Mott law [51],

$$\sigma\left(T\right)=\exp\left[-\left(T_0/T\right)^{1/4}\right] \qquad \text{with} \quad T_0=\beta/kg_F\alpha^3\,, \tag{2.10}$$

where α is the localization radius of the electron wave function, and $\beta\sim 1$ is a numerical factor. However, at room or higher T of practical interest, the primary transport mechanism in bulk materials is typically band conduction.

It has long been established that room temperature conduction in chalcogenide glasses is dominated by band transport [51]. One piece of evidence is that in all chalcogenide glasses the activation energy of conduction is close to half the mobility gap, $E_a\approx G/2$, identified with the Fermi level pinned at that position. The lack of hopping is explained by the abnormally strong polaron effect for localized charge carriers [51, 4, 59], requiring electron transitions to be accompanied by the inter-center transfer of atomic deformations (polaron cloud), which exponentially suppresses the probability of hopping. The strong polaron effect makes chalcogenide glasses significantly different from other amorphous semiconductors, such as a-Si, where hopping conduction was experimentally observed [51, 37].

On a more quantitative level, we note that the polaron effect on hopping conduction was explicitly taken into account in Ref. [7]. It was shown (in Eq. (24) of that work) that in the high temperature regime the exponent of conductivity contains both the well known Mott term [51] $(T_0/T)^{1/4}$ and the polaron related term $W/2kT$ with the polaron shift W being close to $G/4$. The latter combination cannot be reduced to the observed activation conductivity exponent $\approx G/2$.

Finally, a simple estimate can show how hopping cannot provide the high current densities $j\sim 10^4$ A/cm^2 observed in the glassy state of modern PCM:

$$j\sim\frac{q\nu}{R^2}\exp\left(\frac{-E_a}{kT}\right)\sim 5 \quad \text{A/cm}^2\,, \tag{2.11}$$

where $\nu\sim 10^{13}\text{s}^{-1}$ is the frequency of attempts, inter-center distance $R\sim 10$ nm, and $E_a=0.4$ eV. For comparison, the devices of area 10^{-10} cm^2 with average current of 1 μA used in Ref. [32, 31], correspond to a current density of 10^4 A/cm^2, decades higher than expected for hopping from Eq. 2.11.

The latter estimate can be put in a more standard perspective using Motts criterion of band conduction [51], according to which the thermally activated conduction $\sigma=\sigma_0\exp(-E/kT)$ should have a pre-exponential in the range $\sigma_0=150-600\Omega^{-1}\text{cm}^{-1}$.

Contrary to the above understanding, the authors of Refs. [32, 31] and [46] proposed that conductivity in chalcogenide glasses is due to an altered form of hopping.

In that work it was assumed that electrons move without tunneling between equally spaced centers. The same hopping-without-tunneling mechanism was originally proposed for ionic conduction, i.e. for heavy (atomic) classical particles that possess continuous energy spectrum above the barrier[6, 56]. For the case of light quantum particles, such as electrons or holes, the spectrum is discrete and may have no quantum states between the barrier and the mobility edge.
The continuous energy spectrum needed for the purely activated transitions assumed in Refs. [32, 31] and [46] starts at the mobility edge. Therefore, the 'no-tunneling' activated electronic transitions between the nearest neighbours would have to go via intermediate states at the mobility edge. However, allowing the electron or hole to utilize the states at the mobility edge is inconsistent with hopping conduction. Indeed, carriers at the mobility edge would attain the band mobility, which is well above that of hopping, thus giving rise to band transport and the nearest neighbor concept would not apply. In other words, having activated to the mobility edge, the charge carrier would become free and capable of traveling considerable distances to other (far from the nearest) traps or even to the device terminals. The above reasoning explains why the hopping-without-tunneling mechanism has never been included in the existing theory of hopping conduction in semiconductors. The work in Refs. [32, 31] and [46] interpreted $E_a \approx G/2$ as the activation energy of hopping to the nearest center, assuming a transition through an intermediate state. In addition, it was assumed that all the inter-center distances are the same, thereby neglecting fluctuations in center concentration and activation energy, which are known to have exponentially strong effects on hopping conduction and determine the temperature and field dependence [71].

2.1.6 Optimum Channel Hopping

Optimum channel hopping describes the gigantic transverse conduction that has been observed [61] in thin amorphous films. A thorough review of the related work is provided in Ref. [64]. Similar to classical hopping conduction discussed in section 2.1.5, optimum channel hopping involves tunneling between localized states but it differs from the classical mechanism in the following ways: i) optimum channel hopping does not occur on the macroscopically isotropic percolation cluster but, rather, through untypical and nearly rectilinear hopping chains of spatially close localized states; ii) it is characterized by laterally nonuniform (or pinhole) current flow; and iii) it can dominate over typical band transport in systems that are thin enough or subject to sufficiently strong electric fields. For chalcogenides, we consider the possibility that optimum channels can be comprised of localized states that are not subject to strong polaron effects.
Following the approaches in Refs. [61] and [64] the analysis will concentrate on optimum channel hopping through short distances via favorable yet sparse clus-

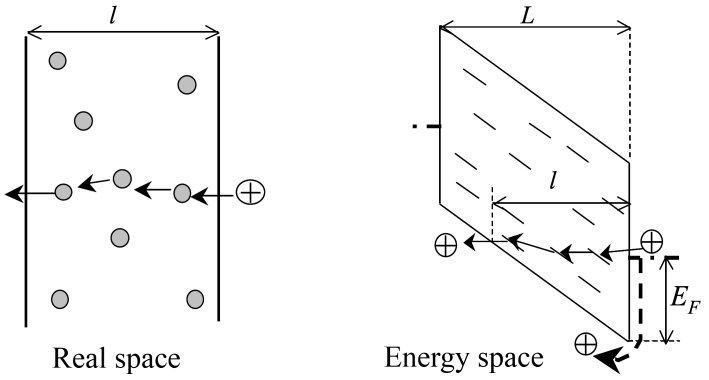

Figure 2.6: Left: field emission via hopping through an optimum chain; circles represent localized states. Right: same in the energy space.

ters of rather rigid localized states that form efficient transport pathways (see Fig. 2.1.6). The conductivity will be dominated by optimum pathways that are a compromise between a high transmission rate and not too low probability of finding the pathways being considered. For the case of thin amorphous films, it was shown [64, 48] that optimum channel hopping leads to a transverse conductivity given by

$$\sigma \approx \exp\left(-\frac{8L\lambda}{\alpha}\right), \tag{2.12}$$

where L is the thickness, α is the localization radius, $\lambda \approx -\ln(g_0 kT\alpha L^2) \gg 1$, and g_0 is the density of localized states. Because Eq. 2.12 is not widely known to the microelectronic community, its simplified derivation will be mentioned. Consider a hopping pathway formed by N-center chain of almost equidistant centers. The probability of finding such a chain is estimated as $p^N = \exp(-\lambda N)$, where $\lambda \equiv \ln(1/p)$ and p is the probability of finding one center in the pathway. The probability of hopping through a distance L/N (between two nearest centers in the chain) can be written in the form $\exp(-2L/N\alpha)$, where α is the localization radius on the center. The product of these probabilities $\exp(-N\lambda - 2L/N\alpha)$ gives a partial current through an N-center chain. Optimizing it with respect to N determines the most efficient chains and results in Eq. 2.12; expressing λ through the density of states takes a more accurate approach [64].

Optimum channels in thin films

For the case of thin amorphous films subject to moderate fields ($\mathcal{E} < E_F/qL$, where E_F is the Fermi level), it was shown [64, 48] that optimum channel hopping leads to a transverse conductivity given by

$$\sigma \approx \sigma_0 \exp\left(-\sqrt{\frac{8L\lambda}{\alpha}} + 1.6\sqrt{\frac{q\mathcal{E}L}{kT}}\right), \tag{2.13}$$

where the parameters are the same as in Eq. 2.12. Polaron effects are neglected in Eq. 2.13 and, therefore, in chalcogenide glasses this form of hopping conduction cannot rely on the typical electronic states near the Fermi level. However, these channels through extremely thin films or in the presence of strong fields can be formed by untypical spatially close states, for which the effects of polaron cloud are less significant, or they can be formed by states far from the Fermi level having much smaller polaron shifts; for the case of chemically imperfect thin films, hopping in optimum channels could be due to extraneous states formed by certain impurities.

Optimum channel field emission

The standard interpretation of field emission is based on the model of electron tunneling through a triangular potential barrier with a slope $\mathcal{E}$ due to an electric field [73]. The model discussed in this section proceeds from the premise of a continuous energy spectrum of localized states in the mobility gap, typical of amorphous materials and capable of giving rise to hopping conduction. Such states lie high enough above the Fermi level that they can not be affected by the strong polaron effect that suppresses hopping. The possibility of hopping transport through such 'rigid' states far from the Fermi level is fully compatible with the above-described suppressed hopping at the Fermi level.
For the case [48] of strong fields, $\mathcal{E} \gg E_F/qL$, Eq. 2.12 remains valid with the substitution $L \to l = E_F/q\mathcal{E}$ (see Fig. 2.1.6 right). As a result, one obtains

$$\sigma \approx \sigma_0 \exp\left(-\sqrt{\frac{8E_F\lambda}{\alpha q\mathcal{E}}}\right), \tag{2.14}$$

which is significantly different from the standard field emission conduction with $\ln(\sigma/\sigma_0) \propto -1/\mathcal{E}$. One qualitatively distinctive feature of the above considered field emission is that it is significantly nonuniform and occurs through rare optimum channels (as opposed to the standard uniform Fowler-Nordheim emission from contacts [73, 27]; this may lead to local heating, facilitating structural transformations in chalcogenide glasses. Another feature related to such lateral nonuniformity is that very small area devices, $A \lesssim \alpha L \exp(\sqrt{E_F\lambda/\alpha q\mathcal{E}})$ may not have an optimum channel with certainty, in which case their resistances will be determined by the most efficient of available random channels; hence, there will be strong variations between the conductances of nominally identical cells.
Overall, it should be noted that the field emission mechanism can be expected to show up in very thin structures where the hopping resistance corresponding to Eq. 2.14 is not blocked by a significantly larger resistance of the film in series.

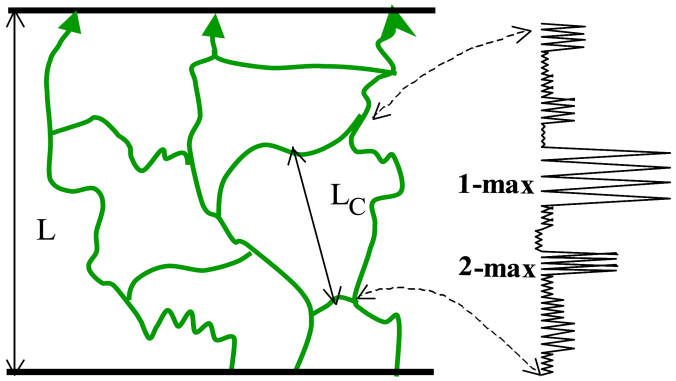

Figure 2.7: Left: Fragment of percolation cluster with mesh size L_c in a material of thickness L. Right: equivalent circuit of a filament of the percolation cluster where exponentially different resistors in series are depicted by resistors of different sizes; the first and second maximum resistors are marked for illustration.

2.1.7 Percolation Conduction

In general, conductivity in randomly nonuniform materials is described in terms of percolation [71]. This concept includes both the hopping conduction and band conduction in a medium where charge carrier concentration exponentially varies between different locations due to spatial variations in the electron potential energy. The concept of spatially varying mobility edge can be derived based on the theory described in section 2.1.3 where a glass band structure is represented by a set of random potential wells with localization/delocalization effects leading to the mobility edges. Some regions will contain predominantly deeper than the average or shallower than the average potential wells corresponding to local variations in the envelope electronic potential in the form of smooth wells or barriers. The latter variations translate into the electric conductivity exponentially varying in space.

Percolation conduction evolves on a mesh built of material regions with conductivity below a certain critical value $\sigma_c \equiv \sigma_0 \exp(-\xi_c)$ such that the mesh enables a connection between two flat electrodes, regardless of distance L between them. Such a mesh is called an infinite percolation cluster and is characterized by the correlation (mesh) radius $L_c < L$, as shown in Fig. 2.1.7. The topology of the percolation cluster can be pictured as arising from a multitude of sites where the nearest neighbors can be connected with random resistors $R = R_0 \exp(\xi)$. Here ξ is a random parameter. For example, $\xi = E_F/kT$ for the case of band percolation conduction, where E_F represent a random energy distance between the band edge (which is spatially modulated) and the Fermi level. As another example, $\xi = 2\Delta r/\alpha + \Delta E/kT$ for hopping conduction, where Δr and ΔE are the distances

between the two centers in the real and energy space respectively (α being the localization radius on the center). The cluster forming connection proceeds in sequence starting from the minimum resistor ($\xi = 0$) and adding larger ones up to $\xi = \xi_c$, until the everywhere connected cluster is formed. The mesh structure illustrated in figure 2.1.7 is built of filaments obtained by the series connection of random resistors where the maximum resistor is close to $R = R_0 \exp(\xi_c)$ for each of the filaments.

Following a theory of high-field percolation conduction [70] each cell of the percolation cluster accommodates voltage $V_c = VL_c/L$. Because the resistors that constitute the filament are exponentially different, the latter voltage almost entirely concentrates on the strongest, first maximum resistor (1-max in Fig. 2.1.7). That voltage, concentrated locally, affects the resistance of the element across which it drops. The mechanism of the latter action can depend on the specific system under consideration: changes in center occupation numbers for the case of hopping, or field-induced ionization for the case of band transport. The field affected maximum resistor in the filament decreases its resistance down to the second maximum (2-max in Fig. 2.1.7), after which the voltage distributes evenly between the two resistors (1-max and 2- max), modifying both of them, and then extending to the third maximum resistor, and so on. Such equalization will sequentially take place in a number of resistors having ξ_i from the maximum one (ξ_c) down to $\xi_0(V)$ defined by the condition

$$\sum_{\xi_0}^{\xi_c} \xi_i = \frac{qV_c}{kT} \,. \tag{2.15}$$

Approximating the sum by the integral gives $(\xi_c - \xi_0)^2/2\xi_{\max} = qV_c/kT$, where it is assumed that the random parameter ξ is uniformly distributed in the interval from 0 to $\xi_{\max} \sim \xi_c$. As a result, the effective conduction is described by

$$\sigma \propto \exp\left(-\xi_0\right) = \exp\left(-\xi_c + \sqrt{\frac{2\xi_{\max} qV_c}{kT}}\right) . \tag{2.16}$$

Substituting here the definition $V_c = VL_c/L$ and $\mathcal{E} = V/L$ one finally obtains

$$\sigma\left(\mathcal{E}\right) = \sigma\left(0\right) \exp\left(\eta\sqrt{\frac{q\mathcal{E}L_c}{kT}}\right) , \tag{2.17}$$

where $\eta \sim 1$ is a numerical coefficient.

Thus, the conductivity depends on electric field in a manner very similar to the original PF result. Furthermore, assuming that each resistor has a linear dimension of the medium range order parameter r_c, L_c can be numerically estimated as $r_c(\delta E_a/kT) \sim 10 r_c \sim 10$ nm, where δE_a is interpreted as the amplitude of variations of the activation energy of conduction. It is estimated as the valence

band offset between the most conductive (close to crystalline GST) and least conductive amorphous GST regions: $\delta E_a \approx 0.4$ eV. With the above estimate in mind, Eq. 2.17 predicts significant non-ohmicity starting from $\mathcal{E} \sim 3 \times 10^4$ V/cm, in reasonable agreement with observations.

Finally, in the case of very thin films ($L < L_c$) the transversal conduction will be determined by rare, most conductive channels formed by random regions of relatively high carrier concentration, rather than the percolation cluster of mesh size L_c. Assuming that the resistors with $R = R_0 \exp(\xi)$ and $\xi < \xi_L$ are involved, the probability of finding the number $L/2r_c$ of such resistors forming a chain through the film between the electrodes can be written as $\exp[(L/2r_c)\ln(\xi_L/\xi_{\max})]$. Dividing the latter by that chain resistance $R_0 \exp(\xi_L)$ gives the partial conductance of chains with $\xi \leqslant \xi_L$. Optimizing the exponent of the latter ratio with respect to ξ_L gives the optimum chain parameter $\xi_L = L/2r_c$. As a result, the conductance of the film can be estimated as

$$\sigma \propto \exp\left\{-\frac{L}{2r_c}\left[\ln\left(\frac{V_{\max}}{kT}\frac{2r_c}{L}\right)+1\right]\right\}. \tag{2.18}$$

In the latter equation, one can impose the condition $\sigma = \sigma_\infty \equiv \sigma_0 \exp(-E_a/kT)$ when $L = L_c$, where σ_∞ has the meaning of the bulk conductivity. As a result, the effective conductivity of thin structures ($L < L_c$) can be written in the form

$$\sigma = \sigma\,(calE)\exp\left\{\frac{L_c - L}{2r_c}\left[\ln\left(\frac{V_{\max}}{kT}\frac{2r_c}{L}\right)+1\right]\right\}, \tag{2.19}$$

where $\sigma(\mathcal{E})$ is given by Eq. 2.18. Here we have neglected the difference between logarithmic terms evaluated at L_c and L and have taken into account that $\xi_m athrmmax = V_{\max}/kT$, where $V_{\max}$ is the maximum transport barrier.

One prediction of Eq. 2.19 is that the effective activation energy of conduction $E_a = |d\ln(\sigma)/d(1/kT)|$ will decrease as the film thickness decreases below $L = L_c$. Another prediction refers to the case of extremely small devices with area below $A_c \sim r_c^2 \exp\{-(L/2r_c)\ln[(2r_c/L)(V_{\max}/kT)]\}$ so that the above defined optimum channel is unlikely to be found within the device area. For such devices, conductance will be determined by the most efficient of the available channels, which will differ between samples; hence, there will be strong fluctuations in conductance between nominally identical devices. According to a rough estimation, that might occur well below the 10 nm scale.

2.1.8 Conduction Through Crystalline Inclusions in Amorphous Matrix

It is known that the reset pulse in chalcogenide PCM melts the material which then cools down fast enough to freeze in the amorphous phase, forming a dome (sometimes called a 'mushroom') as sketched in figure 2.1.8. This melting-to-freezing transition is believed [69, 28] to result in a number of crystalline particles

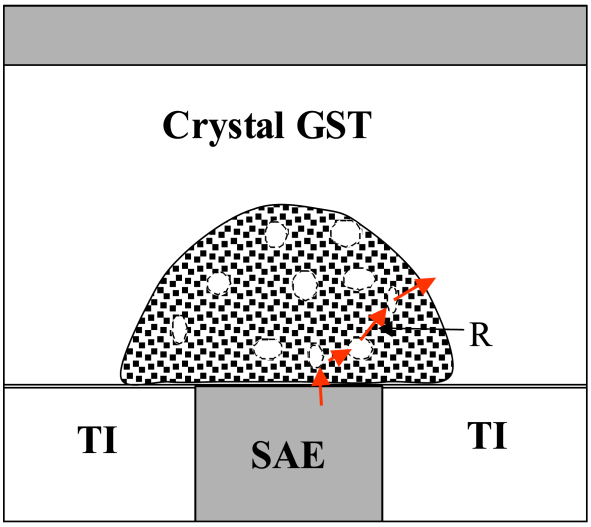

Figure 2.8: Amorphous dome with crystalline inclusions as part of the typical PCM structure including a small area electrode (SAE) and thermal insulator (TI). R is the average distance between crystallites. Arrows represent the current flow utilizing a path of minimum resistance.

embedded in the amorphous matrix. The latter scenario results in an interesting possibility that the system conductance will be governed by potential fluctuations created by the embedded crystallites. The presence of embedded crystallites follows from the standard thermodynamic consideration for the case of any glass possessing a crystalline counterpart of lower chemical potential. The model is based on the known valence band offset $\Delta \approx 0.4$ eV between the amorphous and crystalline phases (see Fig. 2.1.8). According to the standard principles of heterojunction physics, this offset is accommodated by the system through electrostatic screening. The screened potential is described by the standard Poisson equation $\nabla^2\phi = -4\pi\rho$ where the charge density is in turn related to the potential ϕ. That relation depends on the density of electron states $g(E)$, which, following the approach in Ref. [51], is assumed constant. This gives $\rho = \phi q^2 g$ and the Poisson equation reduces to

$$\nabla^2\phi = -\phi/r_s^2 \qquad \text{with} \quad r_s = 1/\sqrt{4\pi q^2 g}\,, \tag{2.20}$$

where r_s has the physical meaning of the screening radius. The solution of Eq. 2.20 for a spherically symmetric case is well known, $\phi \propto r^{-1}\exp(-r/rs)$. The coefficient in front of it is determined by the boundary condition $q\phi(r_x) = \Delta$, where r_x is the crystallite radius. As a result each crystallite creates a potential

$$\phi\,(r) = \Delta\frac{r_x}{qr}\exp\left(\frac{r_x - r}{r_s}\right) \qquad \text{when} \quad r > r_x\,; \tag{2.21}$$

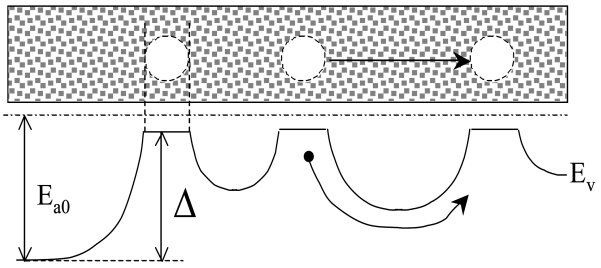

Figure 2.9: Top: a fragment of amorphous matrix with embedded crystallites. Bottom: energy band diagram showing valence band edge E_v in the crystalline and amorphous matrix (with offset Δ) and the activation energy E_{a0} is an amorphous phase without crystallites. Dot-dashed line represents the chemical potential. Arrows show the current flow between two crystallites.

$r_s \geqslant 100$ nm in the typical chalcogenide glasses. We note that the above assumption of constant density of states is not very restrictive as long as we are interested in distances shorter than r_s that is $\phi(r) \approx \Delta r_x/qr$; this can be readily verified for another standard case of a single-level density of states often used for crystalline semiconductors.
The potential in Eq. 2.21 is the same as that of a coulombic center with effective charge

$$Zq = \frac{r_x \epsilon \Delta}{q} \sim 10q\,. \tag{2.22}$$

Therefore, one can use the entire wealth of results known for systems of charged centers in semiconductors to derive the following implications:

- Fluctuations of the electrostatic potential energy exist with the characteristic screening radius rs and amplitude [71] $\delta U = Zq^2\sqrt{n_c r_s^3}/(\epsilon r_s)$, where the square root represents the fluctuation in the number of charged crystallites of concentration n_c in a volume of radius r_s. Taking into account the above definition for Z, one can write,

$$\delta U \approx \Delta\sqrt{v\frac{r_s}{r_x}}\,, \tag{2.23}$$

  where $v \equiv n_c r_x^3$ is the volume fraction occupied by crystalline particles. Using the above mentioned parameters it can be rather significant, $\delta U \gg kT$.

- The average decrease in the mobility edge, $\delta E_m \approx Zq^2(n_c)^{1/3}/\epsilon$ representable as

$$\delta E_m \approx \Delta v^{1/3}\,, \tag{2.24}$$

can be significant as well. The total decrease in activation energy of conductivity due to percolation can be estimated as

$$\delta E_a = \delta E_m + \nu \delta U \,, \tag{2.25}$$

where ν is a numerical multiplier of order unity. It is dominated by its fluctuation component δU as long as the average distance between crystallites is shorter than the screening radius, $R < r_s$.

- The Poole-Frenkel effect appears here without any additional assumptions about the presence of coulombic centers in a material. The consideration in section 2.1.1 will apply with corresponding renormalizations of the centers charge, $q \to Zq$. For example, the critical field of interplay between the regimes of one- and two-center field ionization regimes will become $Ze/4\epsilon a^2$; numerically, it is $\sim 10^5$ V/cm when the distance between crystallites is $a \approx 10$ nm. The two-center ionization effect results in the current

$$I = I_0 \exp\left(\frac{\epsilon r_x a \mathcal{E} \Delta}{qkT}\right) , \tag{2.26}$$

and the one-center effect becomes

$$I = I_0 \exp\left\{\frac{2\epsilon}{kT}\sqrt{\left(\frac{r_x \Delta}{q}\right)^3 \mathcal{E}}\right\} . \tag{2.27}$$

- All the implications of the percolation conduction mechanism in section 2.1.7 will be applicable here. One specification is that the correlation length L_c [see Eq. 2.17] for a system of charged particles becomes equal to the screening radius rs. In the case of very small devices with size $L < r_s$, the size will play the role of screening radius [52]. In the latter case, Eq. 2.1.7 reduces to $\sigma(V) = \sigma_0 \exp(\eta\sqrt{qV/kT})$. Overall, the mechanism described in this subsection suggests the important role of the reset characteristics that determine the shape and composition of the amorphous dome in PCM devices.

2.2 Models Comparison and Recent Theories

A general theory about transport processes in amorphous materials was developed by Mott using the Miller and Abrahams rate equation for hopping events via tunneling. This theory represents a milestone in the analysis of amorphous materials, and has been widely applied since the 1960s. Nevertheless, classes of amorphous materials such (e.g., the chalcogenide glasses) feature an electrical switching behavior when a threshold field is reached. This electrical behaviour cannot be explained by the pure Mott theory.

The first model that tried to give an explanation was that of Adler and coworkers in the early 1980s [1]. Amorphous materials like chalcogenide glasses are characterized by charged defective states, a.k.a. valence alternation pairs (VAPs), that act as recombination centers. Positive defects can be neutralized by acquiring an electron ($C_3^+ + e \rightarrow C_3^0$), whereas negative centers can combine with holes ($C_1^- + h \rightarrow C_1^0 \rightarrow C_3^0$), even though this second reaction is slower than the first one. The equilibrium reaction $2C_3^0 \leftrightarrow C_3^+ + C_1^-$ must hold true at any time and at any place. Electrons and holes are generated via impact ionization, so that extra pairs of carriers are generated along the material and can interact with VAPs. In the OFF state (high resisitivity), the generation and recombination rates for holes and the equation describing the kinetics of equilibrium hold true and a local equilibrium is always present. However, when the electrical field reaches a critical value, a great concentration of holes is generated near the anode and the material can switch to the ON state (low resistivity). The holes neutralize C_1^- traps in the bulk, leaving there and excess of positive defects. Then, according to the kinetics of equilibrium, these defects react with electrons (from the cathode), leaving an excess of negative charges, that are compensated by positive charges from the anode. When the new equilibrium is established, since the majority of VAPs are now neutral, a conductive filament where electrons can transit without being trapped is created, and the conductivity is greatly enhanced. In the ON region high fields are sustained by depletion layers close to the anode and the cathode, keeping the VAPs in the bulk neutral.

The ideas of Adler have been questioned in the last 10 years, when the interest for chalcogenide glasses has been growing since their exploitation in the field of non-volatile memories. The main skepticism on the Adler's interpretation was about the size of the filament featuring the ON state, whose radius is expected in the micrometer range. More recent experimental investigation have shown that the switching behavior is present also in smaller devices, this giving origin to alternative interpretations.

The non-ohmic conduction mechanisms previously described are listed in Table 2.1 along with their characteristic relations and corresponding domains of applicability. Based on the experimental data, the only ones that can be excluded outright are Schottky emission and classical hopping conduction.

More than one non-ohmic domain with different temperature and thickness dependencies is typically observed, with a faster growing current in the pre-switching region. Each model presented here is able to fit the IV characteristics in a particular operative domain. These observations indicate that IV data fitting alone may not be conclusive enough to identify the most adequate model of transport in chalcogenide glasses.

Due to this lack of certainties about models validity, new theories have been worked out until now. The model proposed by Lacaita and coworkers [60] still

relies on VAPs and impact ionization, but they are modeled within the more common framework of semiconductor band transport.
VAPs give origin to minibands inside the band gap and close to the band edges, while neutral defects originate a tail on top of the valence band, this reducing the mobility gap of the material. Defect states are crucial to describe the carrier generation-recombination mechanisms, which are modeled by means of a capture cross-section following the SHR theory. According to this model, the generation mechanism must also be dependent on the electric field in order to describe the subthreshold exponential behavior of the $I(V)$ characteristics, and on the carrier density in order to achieve the switching point. These considerations suggest impact ionization as the main transport scheme of the model, where traps act like a pillar of a bridge between the valence and the conduction bands. At low currents generation via impact ionization and recombination via trap centers balance each other. As the current increases, traps are more and more filled since the generation rate is high. The recombination process instead is weakly dependent on the bias, so that a critical point where recombination cannot balance recombination any longer is found. The unique way to establish a new equilibrium is obtained by reducing the bias, thus the generation rate. Since the currents are high, this condition must be accompanied by an increased concentration of carriers with high mobility in the conduction band.
Two arguments can be opposed to this model. The first deals with the generation mechanism. Though favored by trap states within the band gap that reduce the energy differences, carries still must acquire a large energy before ionizing, which becomes possible only if the mean free path is long, unless a broad distribution of the defects on the energy scale is considered. Next, impact ionization does not account for the activation energy that stems from the analysis of experimental data taken at different temperatures, and the correct dependence on temperature can only be obtained with appropriate temperature-dependent coefficients.
The latter consideration on the activation energy opens the way to two other models, that are currently still debated. One, proposed by Karpov and coworkers [35, 72], stems from the system free-energy balance and brings back the idea of crystalline filaments surrounded by an amorphous matrix proposed by Ovshinsky.
Crystalline nuclei can form inside the chalcogenide amorphous matrix due to local energy dissipation, mainly in the region close to the cathode where the dissipation is higher. Due to their high conductance, crystalline particles concentrate the electric field, which is a key condition for the reduction of the system free-energy. As a consequence, a local stronger field favors the creation of further crystalline nuclei at the particle edges. As the switching point is approached, a crystalline rod is formed and new nuclei add up to the rod itself. The elongation of the rod makes the field even more intense, this self-sustaining the nucleation

and growth mechanism. Eventually, the initial rod spans across the whole device shunting the electrodes and percolate paths can also form. The presence of high conductive crystalline filaments surrounded by an amorphous matrix makes it possible a large increase in the current without a significant effect on (or a small reduction of) the potential drop.
The second model relies on the idea of switching as a result of an electronic process and is due to Ielmini and coworkers [32, 31]. Contrarily to Karpov, who used the energy to activate the nucleation process, in the Ielmini's model the activation energy refers directly to the transport mechanism, being the energy required by a carrier to reach the bottom of the conduction-band mobility-edge [ammesso che si dica cos]. According to this theory, transport can be described as a sequence of thermally-assisted hops between traps (a generic descriptions of the defectiveness of the system), resulting in a trap-limited conduction scheme. Since an applied field bends the mobility edge, given a pair of traps, the forward and the backward fluxes are differently influenced by the field with an exponential dependence. If the current, thus the field, is low, the difference can be neglected and the conventional Ohmic behavior is found. For higher fields, the exponential dependence of the energy barrier on the field makes one flux much larger than the other one and the exponential regime of the $I(V)$ characteristic is recovered. The presence of a large field let also carriers access trap states closer to the conduction-band mobility edge that were inaccessible due to their high energy, thanks to thermal emission of direct ballistic tunneling. The energy gain from the field is counterbalanced by a relaxation process, but, eventually, a heated population is found sufficiently far from the cathode. The switching condition stems from the balance between the electric field, field-induced energy gain and energy relaxation, and is always accompanied by the non-uniformity of the electric field along the device. Even though the Ielmini's model is not free from oversimplifying hypotheses, such as a fixed carrier concentration which prevents any self-consistency with the Poisson equation and does not match the filling of the traps along the device, it proved to be successful in interpreting a high number of experimental evidences.

2.3 Alternative Charge Transport Model

Classical concepts like carrier concentration, average velocity, and current density are used for describing the carrier collective motion. The symbols N, n, and n_T will denote the concentrations of traps, band electrons, and trap electrons, respectively. The band electrons are free to move along the device and may also undergo scattering processes with the lattice. When this happens they exchange part of their energy with the lattice, without necessarily becoming trapped. In turn, trap electrons are able to move from one trap to another by tunnel effect,

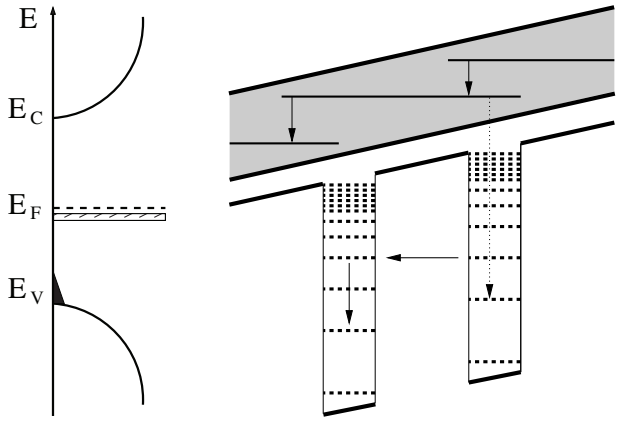

Figure 2.10: (Left) Schematic band diagram showing the position of the valence- and conduction-band edges, Fermi level, and ground state of the traps. A tail of the valence band due to structural defects is also shown. (Right) Schematic description of the electron transitions.

possibly assisted by thermal excitation, or by thermionic emission. They may also be scattered by exchanging phonons with the lattice and moving among the localized energy levels of a trap. The traps are neutral when filled. Also, it is assumed that each trap can release one electron at most, because the energy necessary for the second ionization of the trap is too large.
The effects described here are schematically illustrated in figure 2.3. The distance between the traps is large enough to make the electron wave functions localized within each trap, hence discrete energy states exist. The horizontal arrow indicates a tunnel transition between traps. The mobility of the trap electrons in the analytical model is related to the probability of such transitions. As shown later, it is influenced by the electric field.
Trap electrons also scatter to different energy states (e.g., vertical arrow in the left trap). A small population of high-mobility electrons belong to the band states (grey region). They exchange energy due to collisions (vertical arrows within the band). A band electron may also be scattered back into a trap (dotted vertical arrow in the right trap).
Letting $0 \leq P_T \leq 1$ denote the occupation probability of the traps, it is $n_T = NP_T$, with $0 \leq n_T \leq N$, while the concentration of empty traps is $p \doteq N\,(1 - P_T) = N - n_T$, also with $0 \leq p \leq N$. Instead of describing the current across the traps as due to the average motion of the electron concentration n_T, one might picture it as the result of the motion of the hole concentration p in the opposite direction. This representation is useful for adapting a standard semiconductor-device simulator to the numerical analysis of the device at hand. In the spatially-uniform case (N, n, $n_T = \text{const}$) the charge density

$$\varrho = -q(n + n_T - N) = q(p - n) \tag{2.28}$$

of the material vanishes everywhere because the positive charge of the ionized traps compensates the negative charge of the band electrons at the same spatial position.
In the equilibrium condition the trap-occupation probability P_T reduces to the Fermi statistics with Fermi level E_F,

$$P_T^{\mathrm{eq}} = \frac{1}{(1/d_T)\,\exp\left[(E - E_F)/(k_B T_L)\right] + 1}\,, \tag{2.29}$$

where k_B is the Boltzmann constant, T_L the lattice temperature, and d_T the degeneration coefficient. In particular, for $T_L \to 0$ all traps are filled while the band states are empty, namely, $n^{\mathrm{eq}} = 0$, $n_T^{\mathrm{eq}} = N$. At $T_L > 0$, trap-to-band transitions occur due to phonon absorption, and the traps involved in the phenomenon become positively ionized. At room temperature the population of the band electrons is much smaller than that of the trapped electrons.
If a perturbation is applied to the device, e.g., through a voltage or current generator connected to the external leads, both populations contribute to the total current density $\boldsymbol{J}$ (see Fig. 2.3) where the transport mechanism in the high-field induced condition is described. The contribution of the band electrons is modeled by the standard drift-diffusion expression

$$\boldsymbol{J}_n = q\mu_n n\boldsymbol{\mathcal{E}} + qD_n \operatorname{grad} n\,, \tag{2.30}$$

where μ_n, $D_n = (k_B T_L/q)\mu_n$ are the mobility and diffusivity of the band electrons and $\boldsymbol{\mathcal{E}}$ the electric field. The latter must be calculated by solving a Poisson equation where the charge density is given by (2.28). The contribution of the trap electrons to $\boldsymbol{J}$ is obtained by an equation similar to (2.30), where n, μ_n, D_n are replaced with n_T, μ_T, $D_T = (k_B T_L/q)\mu_T$, respectively. Combining the definitions of the current density $\boldsymbol{J}_T$ and mobility μ_T,

$$\boldsymbol{J}_T = -qn_T\boldsymbol{v}_T\,, \qquad \boldsymbol{v}_T = -\mu_T\boldsymbol{\mathcal{E}}\,. \tag{2.31}$$

The average velocity $\boldsymbol{v}_T$ of the trap electrons in (2.31) can be obtained from a Monte Carlo calculation as in [12], running the code in the spatially-uniform case. Then, mobility is derived from $\boldsymbol{v}_T = -\mu_T\boldsymbol{\mathcal{E}}$. Drift is considered as the only contribution to the trap-electron current density because trap electrons do not interact among each other.

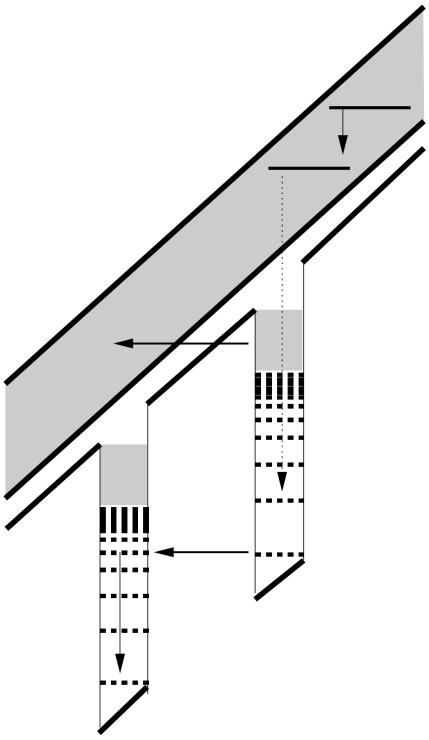

Figure 2.11: Schematic description of electron transitions in a high-field case. The distance between the traps is large enough to keep the electron wave functions at lower energies localized within each trap. However, because of the bending of the trap edge due to the external field, the states at higher energies become continuous (grey regions within the traps). The probability of tunnel transitions between traps is still low. Trapped electrons also scatter to different energy states (e.g., vertical arrow in the left trap). The population of high-mobility electrons strongly increases with respect to the low-field case due to trap-to-band tunneling (horizontal arrow from the grey region of the right trap to the band). Band electrons exchange energy due to collisions (vertical arrows within the band). Their probability of being scattered back into a trap is small (dotted vertical arrow in the right trap).

Chapter 3

Generation-Recombination Mechanism

The main mechanisms that produce the electron transitions between the traps and the band are discussed in this section. They are thermal generation and recombination, Auger recombination, impact ionization due to the interaction between a high-energy band electron and a trap electron, field emission, and the cooperative electron-electron interaction between the low-energy band electrons and a trap electron.

3.1 Thermal Generation and Recombination

The net thermal-recombination rate is given by

$$U_{\text{th}} = \alpha_n n \left(N - n_T\right) - e_n \, n_T \,, \tag{3.1}$$

where $\alpha_n > 0$ is the electron-transition coefficient from the band to an empty trap, and $e_n > 0$ the electron-emission coefficient from a trap to the band. One notes that (3.1) is identical to that used in the standard semiconductor theory for describing the net thermal recombination assisted by traps. However, an important difference is that in the standard theory the above equation must be supplemented with a companion one describing the transitions between the traps and the valence band. Such an equation is not necessary here. The combination of the two equations shows that in the standard theory both populations (electrons in the conduction band and holes in the valence band) are able to simultaneously increase. In contrast, (3.1) alone makes the population of the band electrons to increase at the expense of that of the trap electrons, and viceversa. Remembering

(2.29) and letting

$$n_B \doteq \frac{1}{d_T}\, n^{\mathrm{eq}} \exp\left[\left(E_0 - E_F\right)/(k_B T_L)\right] , \tag{3.2}$$

where E_0 is the ground level of the traps, the following relation holds due to the detailed balance:

$$e_n^{\mathrm{eq}} = n_B\, \alpha_n^{\mathrm{eq}} . \tag{3.3}$$

In the non-degenerate condition it is $n^{\mathrm{eq}} = N_C \exp[(E_F - E_C)/(k_B T_L)]$, where N_C, E_C are the effective density of states and bottom energy of the conduction band, respectively. It follows

$$n_B = N_C \exp\left[\left(E_0 - E_C\right)/(k_B T_L)\right] . \tag{3.4}$$

3.2 Impact Ionization and Auger Recombination

In the standard semiconductor theory both electrons and holes are able to induce such transition processes. Here, Auger recombination induced by holes does not occur because the traps can not ionize twice. Similarly, impact ionization induced by holes does not occur because the maximum hole energy equals the ground state of the trap, hence it can not become very large. As for the transitions induced by electrons, the net recombination rate due to the Auger recombination and impact ionization reads

$$U_{AI} = c_n n^2 \left(N - n_T\right) - b_n\, n\, n_T , \tag{3.5}$$

where $c_n > 0$, $b_n > 0$ are the transition coefficients for the Auger recombination and impact ionization, respectively. In particular, b_n strongly increases when the electric field $\boldsymbol{\mathcal{E}}$ increases. The second term at the right hand side of (3.5) is different from the corresponding expression used in the standard semiconductor theory. This is due to the constraint $0 \le n_T \le N$. The same reasoning leading to (3.3) provides also $b_n^{\mathrm{eq}} = n_B\, c_n^{\mathrm{eq}}$. For Auger recombination induced by electrons to occur it is necessary that n^2 be very large. This, however, happens only in heavily-doped materials because the band concentration becomes very large. Therefore, Auger recombination can be considered negligible in materials like the one examined in this thesis.

Impact ionization is a typical non-equilibrium process which requires a large electric field. An electron (or hole) in the conduction (or valence) band gains its energy by external electric fields and becomes so highly energetic that it can create an electron-hole pair by colliding with an electron in the valence band and exciting it to the conduction band.

In GST memory devices impact ionization may occur because, even in the equilibrium condition, some electrons make a trap-to-band transition by absorbing a phonon. As the current generator is switched on, the increase in the potential

drop inside the device makes the kinetic energy of the band electrons to increase as well. If a collision occurs between a high-energy band electron and a trap electron, the latter may absorb enough energy from the collision to make a transition to the band possible. In this way the number of band electrons becomes larger. For the phenomenon to occur it is necessary that the electron originally in the band *i)* travels for a distance long enough to acquire a sufficient energy from the external field and, *ii)* does not interact with the phonons in the meanwhile. If such an interaction occured, the energy gained from the field would in fact be released to the phonons. From the above description it follows that impact ionization is a non-uniform phenomenon. For instance, the energy of the band electrons near the injection contact is close the bottom of the band. As a consequence, impact ionization can not occur near the injection contact, while it may occur near the other contact. In turn, non uniformity implies that the charge density is different from zero.

3.3 Field Emission

Field emission occurs because the field that is produced by the application of the external current bends the upper edge of the potential-energy profile of the traps. Due to this, a trapped electron has a non-negligible probability to tunnel out of the trap and become a band electron. As the field grows the tunneling distance shortens, so the tunnel probability sharply increases. In this way the number of band electrons becomes larger. In contrast with the case of impact ionization, when the electric field is uniform the field-emission phenomenon has the same probability of occurring regardless of the trap's position. Numerical simulations carried out using the Synopsys TCAD tools show that the electric field is indeed uniform when the trap distribution is such. As noted above, the device considered here is current driven: it follows that when a high-field effect promotes trapped electrons to the band, the increase in conductivity makes the field to die out. As a consequence, the explanation of the snap-back phenomenon should not be based on impact ionization or field emission. On the other hand field emission enhances the subthreshold mobility. The phenomenon is thus important for explaining the shape of the $V(I)$ curve in the subthreshold region but cannot always provide a self-sustained feedback mechanism, as required for the negative-differential resistance to occur.

3.4 Electron–electron Interaction

This mechanism is similar to impact ionization, but involves only low-energy band electrons. It seems a promising candidate to explain the feed-back effect

[11],[20].
Macroscopic models describing the generation process induced by the Coulomb interaction of a trapped electron with band electrons make use of a generation rate. To derive the latter from first principles a numerical approach [11] has been used, exploiting a solver of the two-electron, time-dependent Schrödinger equation. Basing on this approach one evaluates the detrapping probability as a function of the current density in terms of the number of band electrons at a given initial energy.
While in [21],[20] a single trap level was considered (the ground state), here the analysis is generalized to the case of several levels. The restriction of assuming that the band electrons have the same energy is removed as well. The analysis confirms the dependence of the snap-back phenomenon on the driving current.
It also shows that the feed-back process is actually made of the combination of two mechanisms.
Letting f_k be the filling fraction of the kth level E_k of a trap, in the equilibrium condition the Fermi statistics for f_k holds, which keeps the majority of traps filled and makes the population of the band and of the upper trap levels negligible. An external perturbation (typically produced by a current generator) results in an increase in the band population. The electron concentration n of the band is described through a modified Fermi statistics in which the Fermi level E_F is replaced with the quasi-Fermi level E_n. This is equivalent to shifting the statistics along the energy axis. This description is acceptable because in the typical operating conditions the band electrons do not become significantly hot [21]. The higher number of band electrons increases the probability of the trap-to-band transitions per unit time due to the cooperative effect. Such a probability is the largest for the highest trap level (E_M in figure 3.1) because the transition energy $E_C - E_M$ (with E_C the bottom of the band) is the smallest. However, as the population of E_M is initially negligible, so is the number of electrons that are promoted to the band. On the other hand the cooperative effect induces transitions among all pairs of trap levels; such transitions, in turn, tend to equalize the level populations, including that of E_M. The increased population of E_M provides a larger supply of electrons that can be promoted to the band, this providing one of the two contributions to the feed-back mechanism. Finally, the larger concentration of band electrons makes the cooperative effect stronger, this providing the other contribution to feed-back. As more current is injected into the device, n keeps increasing at the expense of the population of the trap levels. The two contributions to feed-back are investigated in the next paragraphs.

3.4.1 Transition Probabilities: General Theory

The $E_s \leftrightarrow E_k$ transition probabilities per unit time between the levels of indices s, k combine the effects of the phonon stimulated-emission/absorption and electron

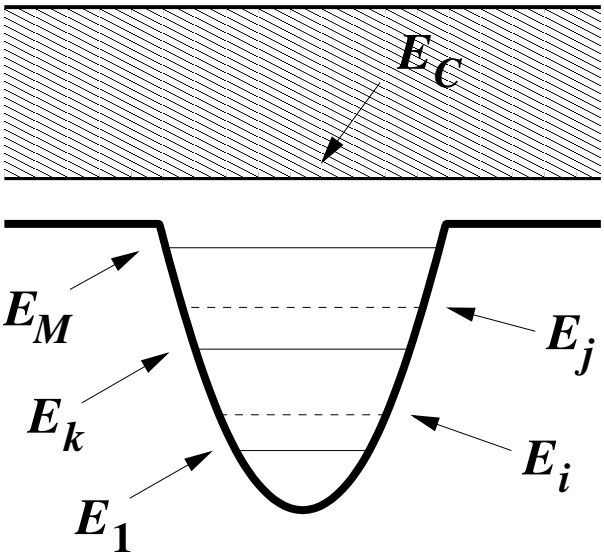

Figure 3.1: Schematic view of a trap with energy levels $E_1 < E_2 \ldots < E_M$. The grey area above indicates the energy band, whose minimum energy is E_C.

interactions, $\dot{P}_{ks} = \dot{P}_{sk} = \dot{P}^P_{sk} + \dot{P}^E_{sk}$. These terms do not include the spontaneous emissions, which are treated separately. The rate $\dot{P}^E_{sk}$ has been obtained adopting the same approach as that used in [22],[19],[18] to model the degradation phenomena related to interface traps; namely, indicating with γ the density of states per unit volume of the band, with f the filling fraction of the band states, with $u = u(E_e)$ the angular average of the group velocity of the band electrons, and letting $\Delta_{sk} = |E_s - E_k|$, one has

$$\dot{P}^E_{sk} = \int_{\Delta_{sk}}^{\infty} \gamma\, u\, \sigma\, f\, \mathrm{d}E_e\,. \tag{3.6}$$

In the above,

$$\sigma = \sigma_0 \left(\frac{E_e - \Delta_{sk}}{E_0} \right)^r, \qquad E_e \geq \Delta_{sk}\,, \quad r > 0\,. \tag{3.7}$$

is the Keldysh-like cross section of the interaction between the trap electron belonging to level E_k and the band electrons, while E_e is the band-electron energy relative to the minimum E_C of the band and E_0 a constant.
The discussion focuses on the integrand of (3.6), where all factors in it are non negative. The energy dependence of the product γu, albeit complicated, is fixed by the lattice structure; the cross section σ is a sharply increasing function of energy because the exponent r is large. In fact, in the problem of [22] the value $r = 11$ is used; in the fully quantum-mechanical approach of [20], a power of the order of a few tens enters the probability that an electron leaves the trap due to multiple scattering with band electrons. For a power law of the type of (3.6), with

$r \sim 10$, the sharp increase of σ starts at the threshold energy $E_{sk}^{\rm th} = \Delta_{sk} + E_0$. As the filling fraction f has an exponentially-decreasing tail, the product σf is expected to have a peak, whose value depends on the position of the tail along the energy axis. As discussed in the introduction, such a position shifts when the device is driven into a non-equilibrium condition by the application of an external current.

The product σf is shown in figure 3.2; as expected, the curves exhibit a peak, whose value turns out to depend strongly on the shift of the quasi-Fermi level E_n. In the figure, the shift in the Fermi distributions is obtained by changing $\eta_n = (E_n - E_C - \Delta_{sk})/(k_B T_L)$ by one unit (k_B is the Boltzmann constant, T_L the lattice temperature).

In contrast, the dependence of the peaks' position on η_n is much weaker: solving $r \exp(\eta_n - \eta) = \eta - r$ for η with $r = 11$ shows that a change $\Delta\eta_n = 2$ moves the peak by $\Delta\eta \simeq 0.02$; in the more realistic case $r = 15$ one needs $\Delta\eta_n \simeq 5.5$ to obtain the same $\Delta\eta$.

As a consequence, the integration domain in (3.6) is not changed appreciably by the shift of E_n. This is important for the purpose of the present discussion, because in the calculation of the integral one leaves the structural factor γu unchanged when E_n changes. As a consequence, the changes in σf are not masked by the local features of γu, and the exponential-like dependence of σf on E_n is inherited by the integral. To further discuss the properties of $\dot{P}_{sk}^E$ we recall the analysis of [19], that shows that σ can also be approximated by a step function

$$\begin{aligned} \sigma &= 0\,, \qquad E_e < \Delta_{sk} \\ \sigma &= \sigma_0\,, \qquad E_e > \Delta_{sk} \end{aligned} \tag{3.8}$$

whose two branches are connected by an exponential. Using this form in (3.6) yields

$$\dot{P}_{sk}^E \simeq \sigma_0 \int_{\Delta_{sk}}^{\infty} \gamma\, u\, f\, {\rm d}E_e = \frac{\sigma_0}{q}\, J_n(\Delta_{sk})\,, \tag{3.9}$$

with $J_n(\Delta_{sk}) \geq 0$ the current density of the band electrons having $E_e > \Delta_{sk}$.

Transition Probabilities: Approximation

In the case of a density of state (DOS) with parabolic-dispersion the transition probability can be approximated and one can obtain an analytical expression.

Letting $E - E_F \leftarrow E - E_F - q\varphi \leftarrow E - E_n - q\varphi = E_e - q(\varphi - \varphi_n)$, with $E_e = E - E_C$ and $-q\varphi_n = E_n - E_C$, and considering the following Fermi function f, the DOS in the parabolic-dispersion case γ and the modulus of the group velocity of the band electrons u:

$$1/f = 1 + \exp\left[\frac{E_e - q(\varphi - \varphi_n)}{k_B T_L}\right], \tag{3.10}$$

$$\gamma = \frac{\sqrt{2}}{\pi^2 \hbar^3} m_e^{3/2} \sqrt{E_e}\,, \tag{3.11}$$

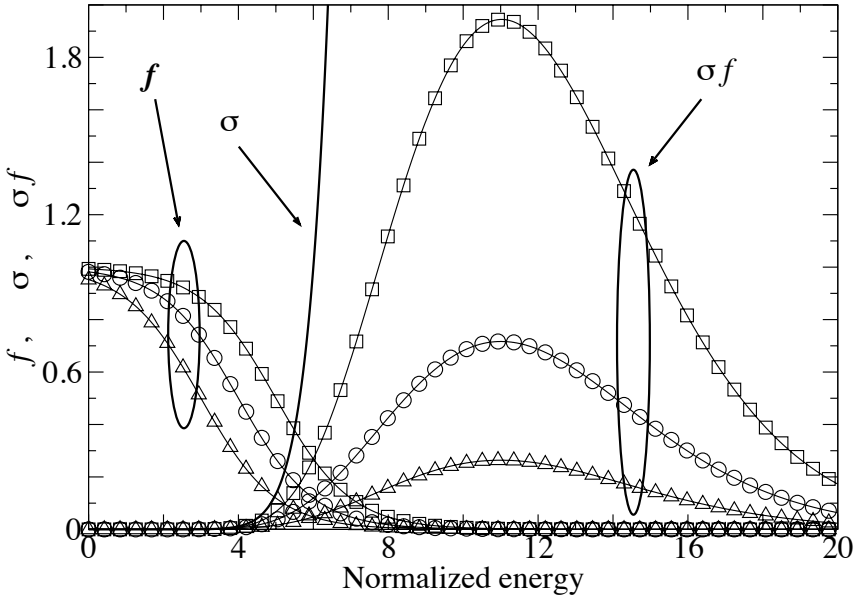

Figure 3.2: The continuous line shows the interaction cross section σ calculated by letting $\sigma_0 = 1$, $r = 11$ in (3.6). Using the normalized energy $\eta = (E - \Delta_{sk})/(k_B T_L)$ yields $\sigma = \eta^r$. Each bell-shaped curve shows the product of σ by the shifted Fermi distribution $1/[\exp(\eta - \eta_n) + 1]$ indicated with the same symbols on the left part of figure (η_n is defined in the text). The shift in the Fermi distributions is obtained by changing $\eta_n = (E_n - E_C - \Delta_{sk})/(k_B T_L)$ by one unit. The corresponding shift in the peak value of the bell-shaped curves is found by solving $r \exp(\eta_n - \eta) = \eta - r$ for η. The area of each bell-shaped curve is $\Gamma(r+1)\Phi_r(\eta_n)$, thus its dependence on η_n is the same as that of the Fermi integral. In the classical limit it becomes $\Gamma(r+1)\exp(\eta_n)$.

$$u = \sqrt{\frac{2}{m_e} E_e}\,, \tag{3.12}$$

the transition probability can be expressed as follows:

$$\dot{P}^E_{MB} \simeq \int_0^\infty \frac{\sqrt{2}}{\pi^2 \hbar^3}\, m_e^{3/2} \sqrt{E_e}\, \frac{\sqrt{2}}{\sqrt{m_e}}\, \sqrt{E_e}\, \sigma_0 \left(\frac{E_e - \Delta_{MB}}{E_0}\right)^r f \, \mathrm{d}E_e\,. \tag{3.13}$$

Here $\Delta_{MB} = E_M - E_C$, where the indexes M and B refers to the highest energy level of a trap (E_M) and the conduction band energy level E_C (see Fig. 3.1). It will be shown in section 3.4.3 that $\dot{P}^E_{MB}$ is the only relevant transition rate. Defining

$$x = \frac{E_e}{k_B T_L} - \frac{\Delta_{MB}}{k_B T_L}\,, \qquad \xi = \frac{q}{k_B T_L}\,(\varphi - \varphi_n)\,, \qquad \delta = \xi - \frac{\Delta_{MB}}{k_B T_L}\,, \tag{3.14}$$

The expression of $\dot{P}^E_{MB}$ can be rewritten as

$$\dot{P}^E_{MB} = \frac{\sqrt{2}}{\pi^2\hbar^3} m_e^{3/2} \frac{\sqrt{2}}{\sqrt{m_e}} \sigma_0 (k_B T_L)^2 \left(\frac{k_B T_L}{E_0}\right)^r \int_0^\infty \left(x + \frac{\Delta_{MB}}{k_B T_L}\right) \frac{x^r}{\exp(x-\delta)+1} \mathrm{d}x \,.$$

In the non-degenerate limit, when $\delta \ll 0$ holds, the transition probability can be approximated as

$$\dot{P}^E_{MB} \simeq \frac{\sqrt{2}}{\pi^2\hbar^3} m_e^{3/2} \frac{\sqrt{2}}{\sqrt{m_e}} \sigma_0 (k_B T_L)^2 \left(\frac{k_B T_L}{E_0}\right)^r r! \left(r + 1 + \frac{\Delta_{MB}}{k_B T_L}\right) \exp(\delta) \,. \quad (3.15)$$

Following the previous definitions the band-electron concentration results:

$$\begin{aligned} n = \int_0^\infty \gamma f \, \mathrm{d}E_e &= \frac{\sqrt{2}}{\pi^2\hbar^3} m_e^{3/2} \int_0^\infty \sqrt{E_e} \, f \, \mathrm{d}E_e = \quad (3.16) \\ &= \frac{\sqrt{2}}{\pi^2\hbar^3} (m_e k_B T_L)^{3/2} \int_0^\infty \frac{\tilde{x}^{1/2} \, \mathrm{d}\tilde{x}}{\exp(\tilde{x}-\xi)+1} \simeq \\ &\simeq \frac{\sqrt{2}}{\pi^2\hbar^3} (m_e k_B T_L)^{3/2} \frac{\sqrt{\pi}}{2} \exp(\xi) \,, \end{aligned}$$

with $\tilde{x} = E_e/(k_B T_L)$. Finally, from 3.15 and 3.16 the expression of the transition probability is found:

$$\dot{P}^E_{MB} \simeq \sigma_0 \, v_r \, n \, \exp[-\Delta_{MB}/(k_B T_L)] = \frac{\sigma_0}{q} J_n \left(\Delta_{MB}, r\right) \,, \quad (3.17)$$

where v_r can be interpreted as the electrons drift velocity and is defined as

$$v_r = 2 \left(r + 1 + \frac{\Delta_{MB}}{k_B T_L}\right) r! \left(\frac{k_B T_L}{E_0}\right)^r \left(\frac{2 k_B T_L}{\pi m_e}\right)^{1/2} . \quad (3.18)$$

In conclusion, in the parabolic-dispersion case the transition probability results to be proportional to the current density related to band-electrons at high energies (above the threshold energy Δ_{MB} as it will be described in the next section). On the other hand, the current density shows a strong dependence on r justifying the abrupt transition from the high resistive state to the high conductive state above threshold.

3.4.2 Threshold Condition

It will be shown in section 3.4.3 that the kinetic energy that defines the onset of the feed-back mechanism (that is, the threshold switching condition of the device) is $\Delta_{MB} = E_C - E_M$ (for the symbols refer also to figure 3.1). It follows that, at threshold, the states of the conduction band with energy $0 \leq E_e \leq \Delta_{MB}$ are filled, whereas those with $E_e > \Delta_{MB}$ are empty. The current density at threshold J_n^{th} can be approximated as

$$J_n^{\mathrm{th}} \simeq \int_0^{\Delta_{MB}} q\gamma \, u \, \mathrm{d}E_e \,. \quad (3.19)$$

In the spatially-uniform case considered here, the relation between the total current density J and the band-electron current density J_n is [21, Eqs. (17,18)]

$$\frac{J_n}{J} = \theta(n)\,, \qquad \theta(n) = \frac{\mu_n n}{\mu_n n + \mu_T (N-n)}\,, \tag{3.20}$$

where μ_n, μ_T are the band and trap mobility, respectively. The total current density at threshold $J^{\rm th}$ turns out to be

$$J^{\rm th} = \frac{\mu_n n^{\rm th} + \mu_T (N - n^{\rm th})}{\mu_n n^{\rm th}}\, J_n^{\rm th}\,, \tag{3.21}$$

where $n^{\rm th}$ is the concentration of the band electrons at threshold. Its value could be calculated using an approximation similar to (3.19). However, it will be determined later from another expression. In turn, the concentration of the trapped electrons at threshold is $N - n^{\rm th}$. When the current generator provides a current density J larger that the threshold one, some states with energy above Δ_{MB} become populated, whence

$$J_n = J_n^{\rm th} + J_n(\Delta_{MB}) > J_n^{\rm th}\,. \tag{3.22}$$

As a consequence, the coefficient $\dot{P}^E_{MB}$ activates due to (3.9).

3.4.3 Band Population

The derivation of the balance equations for the energy levels is formally the same as, e.g., in laser theory. All traps are equal to each other and provide a set of M energy levels $E_1 < E_2 < \ldots < E_M$. The trap concentration is N, while $N_k = N f_k$ is the concentration of traps whose E_k level is filled. The time variation of N_k due to the $E_i \leftrightarrow E_k$ transitions is $R_{ik} = \dot{P}_{ik}\,(N_i - N_k) - N_k\,(1 - f_i)/\tau_{ki}$, with $1 < k < M$, $E_i < E_k$, and τ_{ki} the lifetime of spontaneous phonon emission. The expression for the $E_k < E_i$ case is found by exchanging i with k.
The exchange rate between E_k and the band has a slightly different form because empty band states are always available. It reads $R_{kB} = (\dot{P}^P_{kB} + \dot{P}^E_{kB})N_k - \alpha_{Bk} n N (1 - f_k)$, where $\dot{P}^P_{kB}$, $\dot{P}^E_{kB}$ are the trap-to-band emission coefficients for the phonon and electron interactions, and α_{Bk} the band-to-trap transition coefficient including the effect of spontaneous phonon emission. An Auger-like term is not included in the above expression; this approximation does not violate the microscopic-balance condition because (3.9) vanishes at equilibrium. In this case from $R_{kB} = 0$ one finds

$$[\dot{P}^P_{kB}\, f_k]^{eq} = [\alpha_{Bk} n (1 - f_k)]^{eq}\,, \tag{3.23}$$

with f_k^{eq} the Fermi statistics. It follows

$$\left[\dot{P}^P_{kB}/\alpha_{Bk}\right]^{eq} = n^{eq}\, d\, \exp\left(\frac{E_k - E_F}{k_B T_L}\right)\,, \tag{3.24}$$

where d is the degeneracy coefficient.
The form of the exchange rates simplifies considerably if one assumes that the transitions occurring between neighboring levels are dominant. This is justified by the observation that in this case the energy required to induce the transition is minimum. If, in addition, the electron-interaction perturbation is large enough to make $\dot{P}^E_{rs}$ dominant with respect to the phonon-related coefficients $\dot{P}^P_{rs}$ and $1/\tau_{sr}$, expressions similar to (2a,b,c) of [22] are reached. It follows that in steady state the level populations N_k equalize, $N_1 = \ldots = N_M$, as is ascertained easily starting from the balance equation for the ground level E_1 and continuing with those for $E_2, E_3, \ldots$. Due to the form of the balance equation for level E_M, the equalization makes the exchange rate R_{MB} to vanish. From this, the expression of the common value of the populations is found to be

$$N_1 = \ldots = N_M = \frac{nN}{n + b_M}\,, \quad b_M = \frac{\dot{P}^P_{MB} + \dot{P}^E_{MB}}{\alpha_{BM}}\,. \tag{3.25}$$

In the uniform case the charge density

$$\varrho = q(N - n - \sum_k N_k) \tag{3.26}$$

vanishes; still considering the situation where $\dot{P}^E_{rs}$ is dominant, the vanishing of ϱ coupled with the equalization of the level populations yields

$$N - n - M\frac{nN}{n + b_M} = 0\,. \tag{3.27}$$

Then, letting $\nu = b_M + (M-1)\,N$, the band concentration is found to be

$$n = \sqrt{\nu^2/4 + Nb_M} - \nu/2\,. \tag{3.28}$$

Note that (3.28) holds only above threshold, because the equalization of the level population is implied in its derivation. This, in turn, holds only when the electron-interaction perturbation is dominant. Combining (3.28) with the second of (3.25) and with (3.9) provides a relation between n and $J_n(\Delta_{MB})$. On the other hand, due to (3.22), it is $J_n(\Delta_{MB}) = J_n - J_n^{th}$. As a consequence, the relation thus found has the form $n = n(J_n)$. The threshold value for the band concentration is then found as $n^{th} = n(J_n = J_n^{th})$.
If the trap levels are grouped into a single one, then $M = 1$, $\nu = b_M$ and the expression for n simplifies to (14) of [21]. To date, the available experimental data are not sufficient for providing a reliable fit for the two parameters b_M and N appearing in the definition of ν above. However, the aim of this section is to estimate the sharpness of the dependence of the band-electron concentration on the current density. To this purpose we proceed by letting $M = 1$, so that

$$\nu = b_M = n_B + \beta\, J_n(\Delta_{MB})\,, \tag{3.29}$$

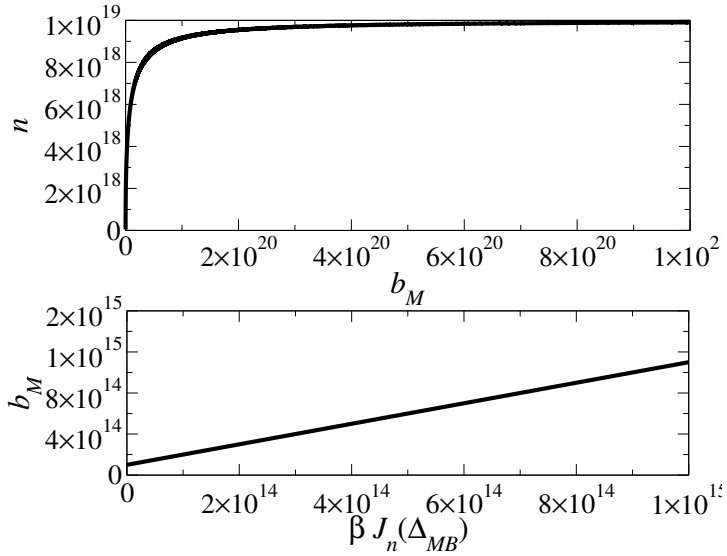

Figure 3.3: The relation $n = n[J_n(\Delta_{MB})]$ for $n \geq n_{th}$, as found from (3.28). It is $J_n(\Delta_{MB}) = J_n - J_n^{th}$. The definition of β is given in (3.30).

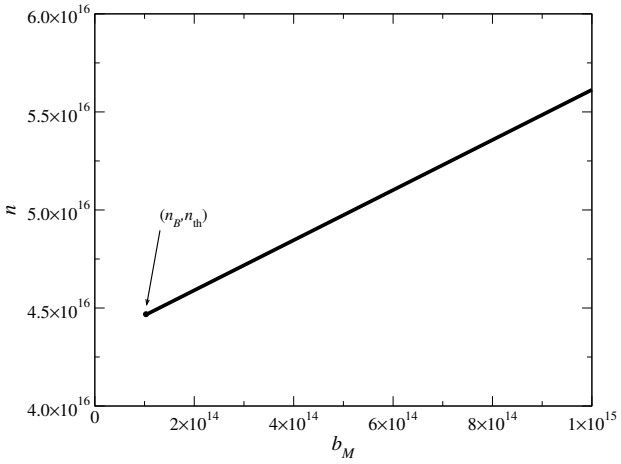

Figure 3.4: Zoom of the $n(b_M)$ graph of figure 3.3 near threshold.

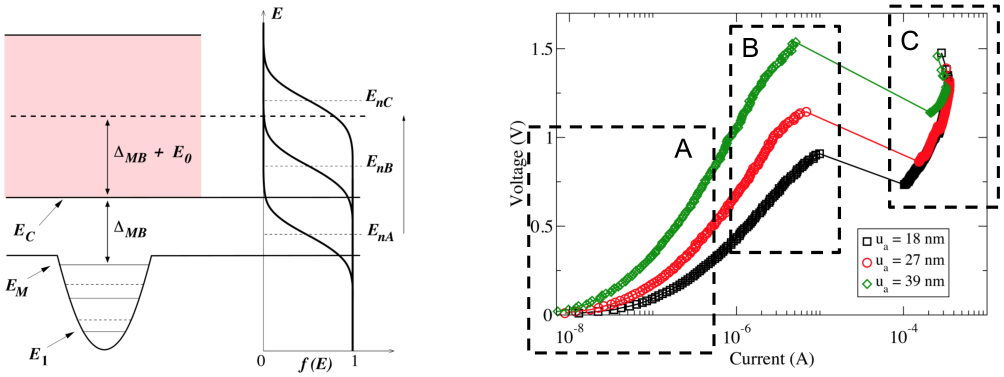

Figure 3.5: The figure describes the three phases of the gradual transition from a charge transport mainly due to hopping processes through localized states to a conduction governed by band electrons only: A) the band-electron concentration is negligible and the charge transport is mainly due to hopping processes through localized states ($E_M < E_{nA} < E_C$); B) Conduction due to the electrons occupying extended states starts acting in parallel to the contribution of the hopping processes ($E_C < E_{nB} < E_C + \Delta_{MB} + E_0$); C) after the snap-back event the conduction is mainly due to the band electrons ($E_{nC} > E_C + \Delta_{MB} + E_0$). Threshold condition: $\Delta_{MB} + E_0 = E_C - E_M + E_0$.

with

$$n_B = \frac{\dot{P}^P_{MB}}{\alpha_{BM}}\,, \qquad \beta = \frac{\sigma_0}{q\alpha_{BM}}\,. \tag{3.30}$$

The definition of n_B in (3.30) is the same as in [21, Eqs. (5,6)]. The form of $n = n[J_n(\Delta_{MB})]$ is shown in figure 3.3. Following [21], the values of the parameters have been fixed to $n_B = 10^{14}$ cm^{-3}, $N = 10^{19}$ cm^{-3}. After an initially sharp increase, the concentration of the band electrons saturates at N. A qualitative analysis of the threshold condition is shown in figure 3.4.3 where the alternation between hopping- and band-transport is described.

In the spatially-uniform case considered here, the relation between the total current density J and the band-electron current density J_n is [21, Eqs. (17,18)]

$$\frac{J_n}{J} = \theta(n)\,, \qquad \theta(n) = \frac{\mu_n n}{\mu_n n + \mu_T(N-n)}\,, \tag{3.31}$$

where μ_n, μ_T are the band and trap mobility, respectively.
Inserting the expression $n(J_n - J_n^{th})$ worked out above into (3.31) provides an intrinsic relation $J_n(J)$. After calculating J_n for each value of the bias current density J, one determines the corresponding concentration n. Then, the electric field $\mathcal{E}$ for each bias point is found from $J_n = q\mu_n n\mathcal{E}$. In this way the branch of the $V(I)$ characteristic above threshold is determined.

Finally, the total current density at threshold J^{th} is determined from

$$J^{th} = \frac{\mu_n n^{th} + \mu_T (N - n^{th})}{\mu_n n^{th}} J_n^{th} . \tag{3.32}$$

Part II

TRANSPORT MODEL: IMPLEMENTATION AND VALIDATION

Chapter 4

Physical Model

The electron-electron interaction between the low-energy band electrons and the trap electrons has recently been tackled from the microscopic viewpoint in a fully quantum-mechanical approach [11]. In this chapter, the phenomenon, previously described, is simply illustrated in the thermodynamical aspects, considering traps with a single energy level and the three systems $\{n\}$, $\{n_T\}$, $\{B\}$ made, respectively, of the band electrons, trap electrons, and lattice. The generator injects the current I and provides a power $P = VI$, where V is the voltage drop across the device. Such a power is absorbed by the band and trap electrons. The two systems in turn exchange energy between each other via electron-electron interactions, and with the lattice via phonon exchange. In a non-equilibrium situation the net flow of energy makes the average energy of the trap electrons to increase. This was already pointed out, e.g., in [33], to show that the energy absorption by the trap electrons increases the probability of a transition from a trap to another. The investigation of [11] has shown that such an absorption is also able to provide trap-to-band transitions. Macroscopically, this is described as a generation process induced by the Coulomb interaction of a trap electron with a number of band electrons. This type of interaction does not produce a recombination process because a band electron can not occupy an already filled trap. It follows that the net recombination rate describing the phenomenon is

$$U_J = -e_J \, n_T \,, \tag{4.1}$$

where the emission coefficient $e_J \geq 0$ depends on the current density $\boldsymbol{J}_n$ of the band electrons. The current density $\boldsymbol{J}_T$ of the trap electrons may also contribute to the phenomenon. If so, the emission coefficient is further enhanced. In order to preserve the microscopic-balance principle, the dependence on the current density is such that $e_J^{eq} = 0$. With reference to the discussion above, in equilibrium it is $P = 0$ and the exchanges of energy balance independently for each pair of systems

$\{n, n_T\}$, $\{n, B\}$, $\{n_T, B\}$. The emission coefficient in (4.1) strongly increases with the current density. As shown in section 4.1, the phenomenon does provide a negative differential resistance.
For the sake of simplicity, the discussion about the analytical model carried out here assumes a one-dimensional, uniform current density. In this case each current is proportional to the corresponding current density, and the emission coefficient becomes a function of the band-electron current I_n. The validation shown in section 4.3 is based, instead, on the general three-dimensional model. From the above discussion it follows that, taking the steady-state case and neglecting Auger recombination, impact ionization, and field emission, the continuity equations for the band electrons and trap electrons read

$$\operatorname{div} \boldsymbol{J}_n = qU_{th} + qU_J \,, \quad \operatorname{div} \boldsymbol{J}_T = -qU_{th} - qU_J \,. \tag{4.2}$$

The total current is $\boldsymbol{J} = \boldsymbol{J}_n + \boldsymbol{J}_T$, with $\operatorname{div} \boldsymbol{J} = 0$. Equations (4.2) are coupled with the transport equations (given by (2.30) for $\boldsymbol{J}_n$, and the like for $\boldsymbol{J}_T$) and with the Poisson equation $-\epsilon\nabla^2\varphi = \varrho = q(N - n - n_T)$. Due to the considered one-dimensional and spatially-uniform case the concentration N is constant. The band-electron concentration n and the trap electron concentration n_T are constant as well. This rules out the diffusive contribution to carrier transport. The need to solve the Poisson equation is ruled out as well, because the scalar electric field $\mathcal{E}$ (albeit unknown) is constant. As the device is globally neutral, spatial uniformity implies charge neutrality whence, from (2.28),

$$n_T = N - n \,, \qquad N \geq n_T \,, n \,. \tag{4.3}$$

and the expression (2.30) for the band-electron current reduces to the drift-only case,

$$J_n = q\mu_n n\mathcal{E} \,. \tag{4.4}$$

In turn, (4.2) combine into $J = J_n + J_T = \text{const}$. Still due to spatial uniformity the left hand sides in (4.2) are equal to zero independently from each other. It follows that, in the one-dimensional, steady-state condition it is $U_{th} + U_J = 0$, namely, using (3.1), (4.1), and (4.3),

$$\alpha_n n^2 = (e_n + e_J)\ (N - n) \,, \tag{4.5}$$

which expresses the balance between recombination and generation events. Letting $b \doteq (e_n + e_J)/\alpha_n$, one extracts n from (4.5):

$$n = \sqrt{\frac{b^2}{4} + Nb} - \frac{b}{2} \,. \tag{4.6}$$

Thanks to spatial uniformity the current through the device is given by $I = AJ$, where A is the cross-sectional area. As anticipated in chapter 3, in the worst

case (that is, when the trap-electron current density does not contribute to the emission process) the emission coefficient e_J can be considered a function of $J_n = I_n/A$. The band-electron concentration n attains the upper value when e_J, hence b, becomes very large. It is easily found that $\lim_{b\to\infty} n = N$, as is apparent also from (4.5). The minimum of n corresponds to the equilibrium case of (4.6) where, remembering (3.3) and the definition of b given above, it is $b^{eq} = b(e_J = 0) = n_B$.
Approximating the ratio e_n/α_n with its equilibrium value n_B and letting $e_J/\alpha_n \doteq n_C\, r(J_n, J_T)$, with $n_C > 0$, yields

$$b = n_B + n_C\, r(J_n, J_T)\,, \qquad r \geq 0, \tag{4.7}$$

with n_B and n_C concentrations. The worst-case expression of $r(J_n, J_T)$ is

$$r = \exp(J_n/J_K) - 1\,, \tag{4.8}$$

with J_K a fitting parameter. Expression (4.8) derives from the microscopic analysis of [11] and fulfills the condition $e_J^{eq} = 0$ stated above. Indicating with L the length of the amorphous chalcogenide-GST material and using $J = J_n + J_T$, $I = AJ$ one finds the expressions relating the field and current with the material's conductance $G_C = G_T + G_n$:

$$J = G_C \frac{L}{A}\mathcal{E}\,, \quad G_T = q\frac{A}{L}\,\mu_T n_T\,, \quad G_n = q\frac{A}{L}\,\mu_n n\,, \tag{4.9}$$

with $n_T = N - n$. The conductance G_C depends on J_n through (4.6,4.7,4.8). It is readily expressed in terms of J by dividing $J_n = G_n\, L\mathcal{E}/A$ by the first of (4.9), to find an intrinsic relation $J_n(J)$ of the form

$$\frac{J_n}{J} = \frac{\mu_n n}{\mu_T n_T + \mu_n n}\,. \tag{4.10}$$

The analysis of the conductance starts from the observation that in equilibrium it is $n \ll n_T = N - n$. When a current I is injected into the device, n increases at the expense of n_T; however, as long as the perturbation with respect to equilibrium is small, the contribution of $\mu_T(N - n) = \mu_T n_T$ to the conductance still prevails. When I further increases, n eventually becomes equal or larger than n_T. On the other hand it is always $\mu_T < \mu_n$ because the trap electrons move only by hopping from a trap to another. It follows that G_C increases with I because n increases with I_n. Eventually G_C must saturate: this occurs in the limiting case when all initially-trapped electrons have become band electrons.
The model for μ_T is important for the above analysis. The conductance G_C, obtained using the parameters listed in section 4.3, is drawn in normalized form in figure 4.1 with $\mu_T = \mu_{T0} = \text{const}$ (solid line), and with (4.14) as mobility model (dashed line). To make the difference between the two curves more visible, J has

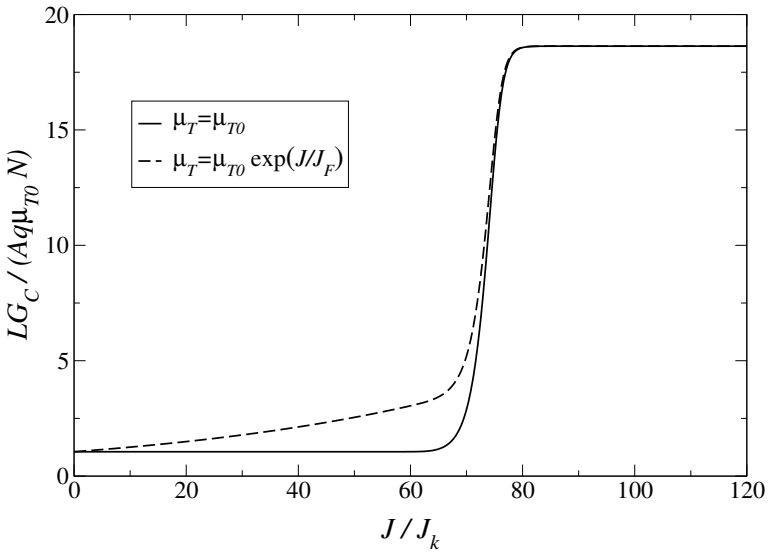

Figure 4.1: Graph of the normalized conductance $LG_C/(Aq\mu_T N)$ vs. normalized current as obtained using the parameters listed in section 4.3. The difference between the two curves is explained in the text.

been used in place of J_n in (4.8). The derivative of r with respect to the current density determines the sharpness of the transition between the low- and high-conductance condition.

It must be remarked that G_C is not the only contribution to the conductance of the whole device. Rather, the device is better described as the series of the amorphous material and of a constant resistance R_S due to the heater, crystalline cap, and upper contact. The structural details mentioned here are visible, e.g., in [13]. The total resistance is thus $R = R_S + 1/G_C$, and the voltage drop across the whole device is

$$V = \left(R_S + \frac{1}{G_C} \right) I \,. \tag{4.11}$$

Using in (4.11) the parameters listed in section 4.3 yields a $V(I)$ curve with an N-shaped form, that corresponds to a snap-back behavior in the $I(V)$ representation. The central portion of the curve exhibits a negative differential resistance. Finally, the first of (4.9) provides the electric field in terms of the current density. As a consequence, any model that expresses the concentration of the band electrons as a function of the current density is readily converted into a model based on the electric field.

4.1 Feedback and Scaling Properties

The $V(I)$ relation (4.11) is non linear because of the dependence of G_C on the current. The non-linearity is such that in a region of operation the total device resistance $R = R_S + 1/G_C$ decreases as I increases. The phenomenon thus possesses an intrinsic feedback mechanism that may give rise to a negative differential resistance. It is useful to remind why bulk-material devices may exhibit such a behavior. In voltage-controlled devices the phenomenon is due the formation of high-voltage regions (domains, see, e.g., [73, Ch. 14.2]), whereas in the current-controlled ones the phenomenon is due to the formation of high-current regions (filaments, same reference).
As the device under investigation is very thin, the formation of spatial filaments is unlikely. The concept of filament may however be kept, if one considers that the two sets of band electrons and trap electrons can be viewed as filaments separated in energy rather than in space. Another observation is that the condition $\mathrm{d}R/\mathrm{d}I < 0$ is not sufficient to produce the negative differential resistance. The condition for it, in fact, is

$$\frac{\mathrm{d}V}{\mathrm{d}I} < 0 \quad \Longrightarrow \quad \frac{\mathrm{d}G_C}{\mathrm{d}I} > \frac{G_C}{I}\left(1 + R_S G_C\right) . \tag{4.12}$$

The type of feedback in terms of the sharpness of the trap-to-band transition is described with the aid of figure 4.2, where current and voltage have been normalized to dimensionless quantities. If the conduction were due to the trap electrons only, the conductance would be low, corresponding, e.g., to a $v(i)$ relation given by the line from the origin through the points A and G. If the conduction were due to the band electrons only, the conductance would be high, corresponding to a $v(i)$ relation given by the line from the origin through the points $B \ldots F$. Actually, the conductance remains low in the current interval from $i = 0$ to the current corresponding to point A. Here the device makes a transition to the high-conductance case. The sharpness of the transition determines the type of feedback.
An example of a situation where the negative differential resistance occurs is the $v(i)$ characteristic that goes from the origin to A, then from A to C, and finally to $D \ldots F$. The voltage decrease due to the increase of the conductance prevails over the voltage increase due to the current increase. As consequence, the portion of the $v(i)$ characteristic after point A has a negative differential resistance. This happens in the realistic cases as shown by the experiments.
The currents corresponding to the threshold and holding voltages are the roots of $\mathrm{d}V/\mathrm{d}I = 0$, and fix the boundaries of the interval over which the snap-back occurs. Remembering (4.12) one finds that the equation to be solved is

$$1 + R_S G_C = \frac{\mathrm{d}G_C/G_C}{\mathrm{d}I/I} = \frac{\mathrm{d}G_C/G_C}{\mathrm{d}J/J} . \tag{4.13}$$

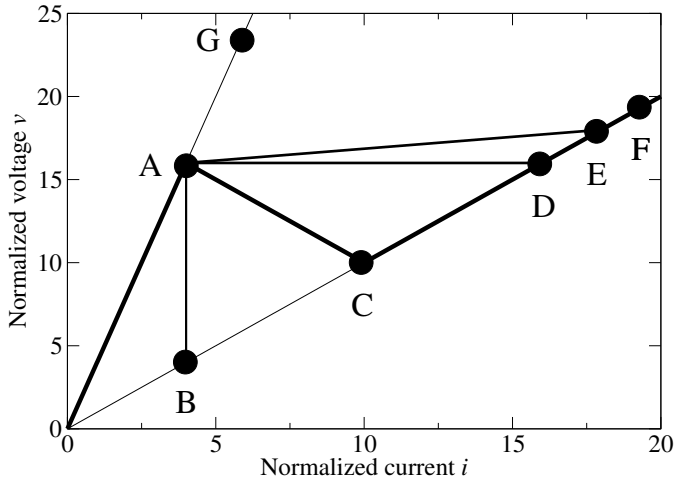

Figure 4.2: Schematic voltage vs. current relations used to illustrate the different types of feedback. The curve from the origin through points $ABCDEF$ describes an abrupt transition (at A all electrons move from the traps to the band). The curves from the origin through points $ADEF$ and AEF describe the cases where the voltage increase due to the current increase is or is not compensated by the voltage decrease due to the increase of the conductance.

The second form of (4.13) is more convenient for discussing the scaling properties, because G_C embeds the generation function (4.8) that depends on a current density. Despite the possible complicacies involved in its actual solution, equation (4.13) provides some hints about how the threshold and holding currents scale when the device geometry is changed. In fact, the right hand side is invariant with respect to the physical and geometrical scaling factors of G_C and (independently) of J. The result shows that in this model the threshold and holding currents densities are invariant with respect to such scaling factors, in agreement with experimental results [32]. In contrast, (4.13) does not provide information about the scaling properties of the threshold and holding voltages themselves. Clearly the observations about the scaling properties are based on the one-dimensional, uniform model considered in this section, and must be corroborated by a more general analysis that solves the full model numerically. The result of such an analysis is shown in section 4.3.

4.2 Experimental Measurements Setup

The model presented here has been validated against experimental data acquired using individual carbon nanotubes (CNTs) as nanoscale heaters to induce ultra-

narrow phase change regions in GST, while applying currents on the order of 10 μA. The CNTs used here were grown by chemical vapor deposition (CVD) with Fe catalyst particles on SiO_2/Si substrates. The as-grown CNTs span Ti/Pd (0.5/40 nm)metal contacts with 1 to 5 mm of separation (see Fig. 4.2) and then created nanoscale gaps in the CNTs through electrical breakdown in air or under Ar flow. This simple approach yielded a wide range of nanogaps (from $\sim$ 20 to 300 nm), which was essential for the subsequent scaling study.

The nanogap is typically near the middle of the CNT, consistent with the electrical breakdown location and with negligible Pd contact resistance. Then, a $\sim$10-nm GST film was sputtered over the device surface, with settings previously found to preserve the good electrical characteristics of CNTs. This deposition fills the CNT nanogaps, creating selfaligned lateral PCM bits. Such devices can be readily switched and examined by atomic forcemicroscopy (AFM); however, a $\sim$5-nm SiO_2 capping layer deposited after the GST without breaking vacuum is used to prolong the switching lifetimes.

GST sputtering is compatible with CNT devices, with conformal deposition and little apparent damage to the CNT. The low currents needed to induce phase change are a result of the excellent thermal stability (up to $>$ 1000 °C) and extremely small diameter ($<$5 nm) of the CNT heaters.

CNT devices are grown directly on SiO_2 and contacted with Pd electrodes as described in Refs. [75]. Both single-wall and small diameter ($<$5 nm) multiwall CNTs can be obtained and used to induce phase change in GST. A 10 nm amorphous film of GST has been sputtered on top of the CNT devices, as shown in figure 4.2. Atomic force microscope (AFM) measurements confirm the thin GST is conformal, and surface roughness is minimally increased from $\sim$0.3 nm (bare SiO_2) to $\sim$0.5 nm (after GST deposition) [75]. Moreover, electrical measurements of the CNT before and immediately after GST sputtering indicate only $\sim$20% change in CNT resistance, suggesting little damage to the nanotube from the sputtering process.

After GST sputtering several compliance-limited DC current sweeps has been performed, while monitoring the voltage across the device. Although the thin GST film spans between the two electrodes, its amorphous resistivity is very high ($\sim$100 Ω·cm), and the current is entirely carried by the CNT during the initial sweep. Subsequent sweeps to higher currents lead to increasing conductivity with voltage snapback, attributed to a gradual transition of the GST surrounding the CNT from amorphous to crystalline phase. At higher currents the temperature of the CNT increases significantly, and a low-resistance crystalline GST "sleeve" begins to form around the CNT. Once the phase transition occurs, the crystalline state of GST is preserved generating hysteresis loops where each forward sweep follows the previous backward sweep.

The current compliance limit has been gradually increased in 20 μA increments.

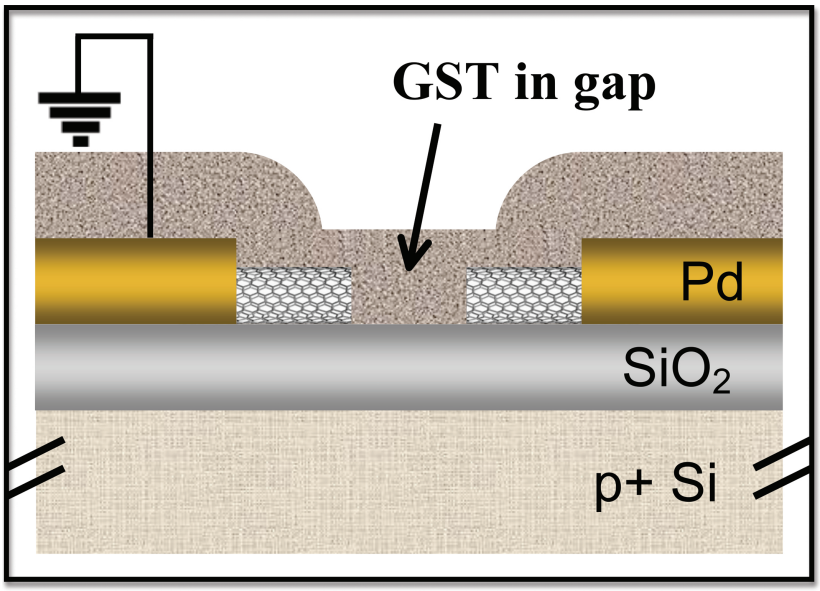

Figure 4.3: Schematic description of the device under test.

Consequently, the resistance of the CNT-GST structure has been reduced by more than an order of magnitude, as an increasing volume of GST surrounding the CNT gradually heats up and crystallizes, introducing a parallel current flow path. Once the current reached ∼160 μA the GST is irreversibly damaged, but the measured IV returned along the original path, indicating the CNT itself was still conducting, unchanged, and undamaged. The last point highlights the resilience of CNTs even under the most extreme conditions, and their durability as nanoscale GST heaters. We note the heating current at which GST phase transition first occurs (∼25 μA) is much lower than in conventional PCM, although voltages are higher due to the relatively long, resistive CNT (∼400 kΩ). Shorter CNTs (¡1 μm) with good contacts have resistance an order of magnitude lower, and would yield effective heating at voltages that are proportionally decreased as well.

4.3 Extension of the Model and Validation

The low-current branch of the $V(I)$ curve (namely, from equilibrium to snap back) is independent of the band-electron mobility. In fact, the concentration of band electrons is negligible in that region, hence the current is essentially due to the motion of the trap electrons. Also, in the model discussed so far the branch is linear because the mobility of the trap electrons is kept independent of the field. On the other hand, the experiments show that the low-current branch is linear only near the origin, whereas at relatively higher currents it exhibits an

exponentially-increasing behavior. The model must then be improved. Observing that at low currents the band electrons do not contribute to the transport, the model is changed by making the mobility of the trap electrons to increase with the electric field. This is consistent with the description of the transport by trap electrons as due to the hopping between traps, as illustrated in chapter 3. In fact, although the field is not high enough to make the trap-to-band transition possible, an increase in the field makes the trap-to-trap hopping easier, hence the mobility becomes larger.

The dependence of the mobility on the field due to this effect is of the exponential type, as shown by the investigations in [33] on tunneling and Poole-Frenkel emission. Moreover, below snap back the relation between field and current is monotonic because the contribution of the band electrons to transport is negligible. Thus the mobility of the trap electrons may be made to depend exponentially on the current instead of field. This is more consistent with the fact that the model must account for the property of the device of being current driven. The following expression has been assumed for the mobility of the trap electrons before snap-back,

$$\mu_T = \mu_{T0} \exp(J/J_F)\,, \tag{4.14}$$

with J_F a parameter. It is also consistent with the interpretation of the subthreshold current as due to a conduction of the Poole-Frenkel type [33] (in this case J_F depends on temperature). Clearly an unlimited increase in μ_T is unphysical. However, at snapback the vanishing of the trap-electron concentration occurs, which makes the contribution of the conductance G_T irrelevant. In the numerical simulations the expression (4.14) is used only up to the snap-back current, then a fixed value is assumed.The use of (4.14) before snap-back only, and the extraction of the parameters μ_{T0} and J_F are detailed in the explanation of the fitting procedure given below.

The electron-transition coefficient from the band to an empty trap is estimated from the relation $\alpha_n = \sigma_n u_{th}$, where the capture cross section is set to $\sigma_n \sim 5 \times 10^{-15}$ cm^2 and, at room temperature, the thermal velocity is set to $u_{th} \sim 2 \times 10^7$ cm/s. The trap concentration is fixed to $N = 10^{19}$ cm^{-3}, in line with the findings of other works (e.g., [33]).

Using the analytical model, the best fit of the experiments is carried out as follows. First, the products $\mu_{T0}N$ and $\mu_n N$ are determined from the slope of the $V(I)$ characteristic near the origin and, respectively, in the after-snap-back region.

The dependence of (4.14) on J is neglected in this phase because the threshold condition is not influenced by it. Next, the ratio n/N is tackled which, due to (4.6,4.7,4.10), is expressed in terms of the parameters n_B/N, n_C/N, and J_K. The latter are found by a best fit of the snap-back and after-snap-back portions of the $V(I)$ characteristic. Using n_B/N in (4.6) one may also determine the ratio

n^{eq}/N. The last parameter J_F is then found by fitting the subthreshold region with (4.14) while leaving the previously-determined parameters unchanged. The best-fit curve resulting from the procedure depicted above is the continuous line in figure 4.4.

The parameters of the trap mobility (4.14) are found to be $\mu_{T0} = 1.22$ cm^2/(Vs), $J_F = 4.18 \times 10^6$ A/cm^2. The value of the band-electron mobility turns out to be $\mu_n = 22.74$ cm^2/(Vs). It is easily found that the condition $\mu_n > \mu_T$ used in the discussion of chapter 4 always holds. Finally, the best fit of the snap-back region provides the following optimal values for the parameters of (4.15): $n_B = 10^{14}$ cm^{-3}, $n_C = 5.12 \times 10^{-14}$ cm^{-3}, $J_K = 7.65 \times 10^4$ A/cm^2. The model demonstrates a fair agreement with experiments despite the sharpness of the snap-back transition. The quality of the fitting at different temperatures and size of the samples is similar.

The model illustrated in this paper has been implemented into the D-2010.03-SP1 version of Synopsys' Sentaurus T-CAD©. Both the analytical form described in sections 4, 4.1 and the general form described in sections 2.3, 3 have been compared with experimental $V(I)$ curves. The fabrication of the GST layers and the measurements have been carried out at the Micro- and Nanotechnology Laboratory of the University of Illinois at Urbana-Champaign [24]. As shown in [75] the conductivity of the carbon nanotubes that form the device contacts is much higher than that of the GST layer. The length of the latter is thus equal to the gap between the nanotubes. Side effects of the current flux within the GST are possible. They may produce variations in the fitting parameters, but do not alter the structure of the model.

Preliminary results about the analytical model have already been shown in [66]. Here the discussion will focus on the general model, with the aid of figure 4.4 that shows Sentaurus T-CAD's outcomes (lines) along with experimental results (symbols). The length and diameter of the device used in the experiments are 110 nm and 4.3 nm, respectively. The model has been implemented into the code by describing the empty traps as holes (namely, $p = N - n_T$ as anticipated in section 2.3) and using the recombination-generation function $U = U_{th} + U_J$ described in chapter 3. The expression of U is rewritten below in terms of the parameters introduced in chapter 4:

$$U = \alpha_n \left[np - (n_B + n_C\, r)\,(N - p) \right] . \tag{4.15}$$

The architecture of Sentaurus T-CAD is such that the mobility and recombination-generation models can be defined by the user, whereas the transitions involving the traps are not accessible. As a consequence, the use of the general model within the code requires an additional step, namely, the decrease of the hole mobility in the region after snap back, in accordance with the discussion carried out earlier. This is achieved by eliminating the exponential factor in (4.14).

The model has been tested against experimental data. GST layers have been

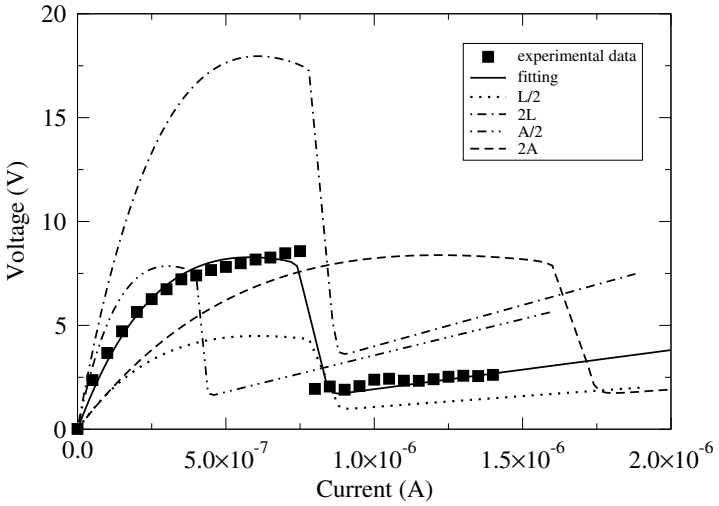

Figure 4.4: Comparison of the model with the experimental curve at $T = 295$ K. The device is a 10-nm GST layer deposited over a 110-nm gap opened within a 4.3 nm-diameter carbon nanotube [24]. The symbols show the experiments, while the continuous line has been calculated by Sentaurus T-CAD using the best-fit parameters described in the text. The other curves also show Sentaurus T-CAD outputs sharing the same parametrization.

deposited using the method described in section 4.2, which makes use of carbon nanotubes (CNTs) as electrodes.

An example of the fitting is shown in figure 4.5, demonstrating a fair agreement despite the sharpness of the snap-back transition. The quality of the fitting at different temperatures and size of the samples is similar (see Fig. 4.6).

The general model in the region below snap back has also been used to test the dependence of the threshold and holding currents on the device geometry. After completing the best fit, the $V(I)$ curve has been calculated again after varying the cross-sectional area or the length of the device, leaving the fitted parameters unchanged. The results are shown in figure 4.4. They show that increasing or decreasing the length leaves the threshold current unchanged, whereas increasing or decreasing the cross-sectional area leaves the threshold voltage unchanged, this in line with the discussion of section 4.1 based on the analytical model.

Another feature of the model is the agreement of the temperature dependence of $G_C = G_T + G_n$ with the experiments. The discussion of this aspect is based on (4.9). In the equilibrium condition the electrons distribute in the energy states according to the Fermi statistics and, if the temperature T_L becomes larger, the concentration n of the band electrons increases as well. Also, it is $\mu_T \to \mu_{T0}$ when $J \to 0$. As the dependence of n on T_L is much stronger than that of μ_n,

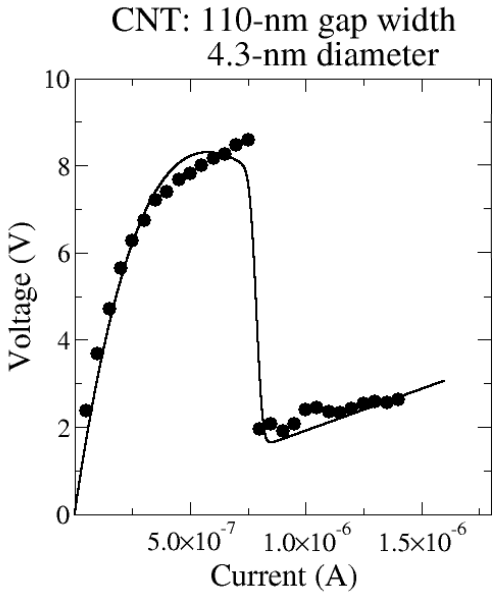

Figure 4.5: Fitting of the model to the experimental curve ($T = 295$ K). The device is fabricated as described in [75]. The best fit yields $n_M \sim N = 5 \times 10^{18}\text{cm}^{-3}, n_m = 10^{-4}N, n_M \sim N, \mu_n/\mu_{T0} = 20.26, I_C = 0.79\mu\text{A}, I_K = 0.01\mu\text{A}, I_F = 0.58\mu\text{A}$.

μ_{T0}, it follows (assuming for simplicity a non-degeneracy condition)

$$G_C(T_L) = G_{C0} + G_{C1} \exp[-E_a/(k_B T_L)]\,, \tag{4.16}$$

with G_{C0}, G_{C1}, E_a parameters that depend weakly on temperature. G_{C1} is dominant over G_{C0} because of the high μ_n/μ_{T0} ratio. Furthermore, as the data in figure 4.7 have been extracted from the linear region of the experimental results of [32] and [25], E_a in (4.16) represents the low-field limit of the activation energy. Figure 4.7 shows a comparison between (4.16) and the experimental results. The value of parameter E_a is 0.33 ± 0.01 eV in both cases. The agreement with experiments of the temperature dependence of the conductance near equilibrium provides a sensible indication supporting the existence and nature of the extended states in the material.

4.4 Implementation of the cooperative electron-electron interaction model on Sentaurus TCAD ©

Charge transport in amorphous chalcogenide-GST used for memory devices is modeled by means of two contributions: hopping of trapped electrons and motion of band electrons. The former constitutes the main contribution to conduction in the subthreshold region while the latter becomes relevant only after the snapback

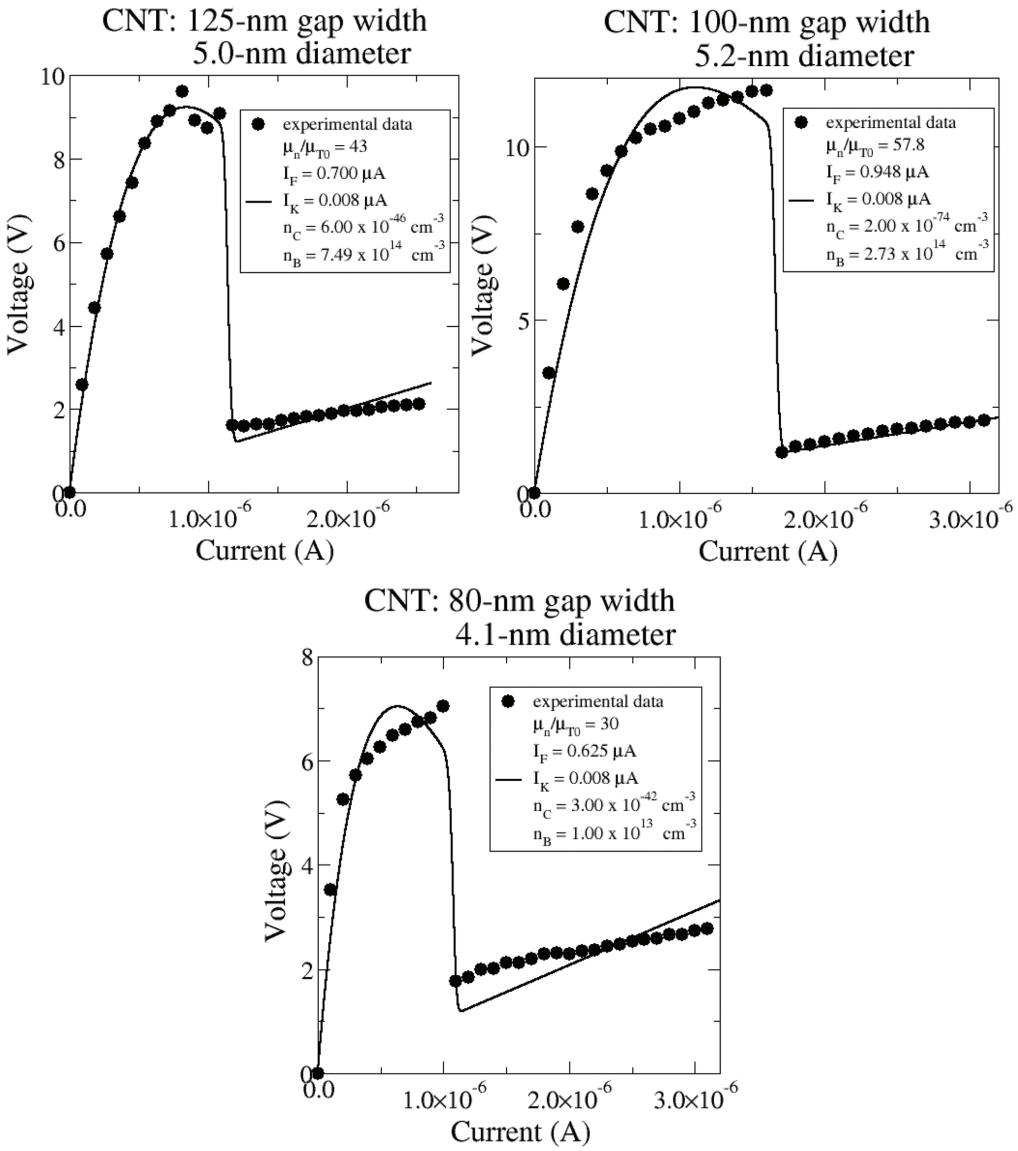

Figure 4.6: The figure shows other fittings of the experimental curves for different sizes of the device under test.

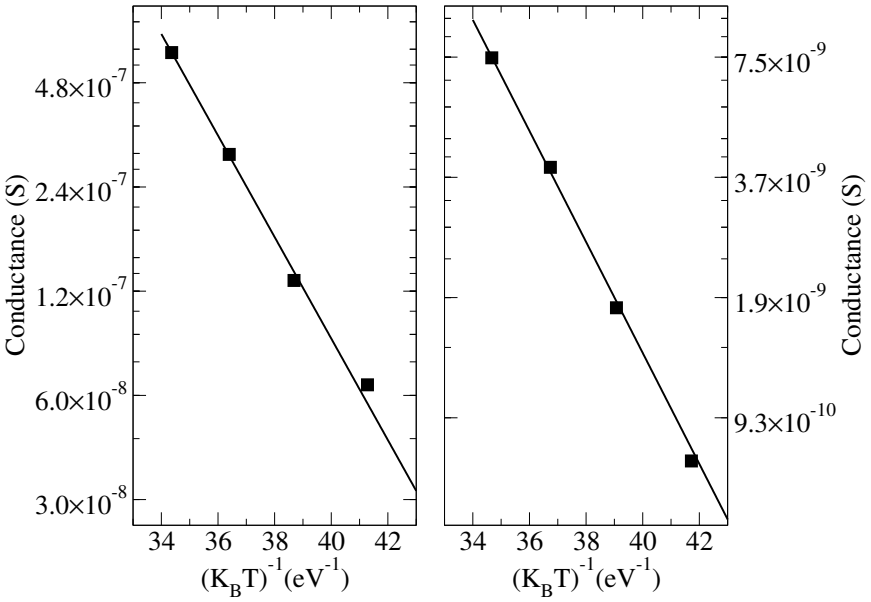

Figure 4.7: Arrhenius plots at small fields of the $G_C(T_L)$ relation (continuous lines) compared with the experimental results (symbols) of [32] (left) and [25] (right).

event occurs. As a consequence, the total current density J is expressed in terms of the current density J_n, related to the band electrons, and the current density J_T of the trap electrons:

$$J = J_n + J_T = \text{const}\,, \tag{4.17}$$

where $J = \text{const}$ because the device is current driven. The model has been implemented into the code by describing the filled traps as holes ($p = n_T$, thus $J_p = J_T$). In order to separate the contributions of the charge carriers in the two regions (below and above threshold), donor and acceptor traps have been included.

In the equilibrium case the donor traps are empty while the acceptor are filled. The hole concentration in the valence band depends on the p-type doping concentration that determines the quasi-Fermi level position (see Fig. 4.8).

Above threshold the population of high-mobility electrons strongly increases with respect to the low current case due to the cooperative electron-electron interaction. This physical behavior has been reproduced adopting symmetrical capture and emission rates for the two types of traps, such that above threshold the holes are captured by the donor traps while the electrons are injected in the conduction band through the acceptor traps. Due to these processes the quasi-Fermi level shifts below the conduction band energy E_C. In this case the hole concentration becomes negligible and the total current is mainly due to the band electrons.

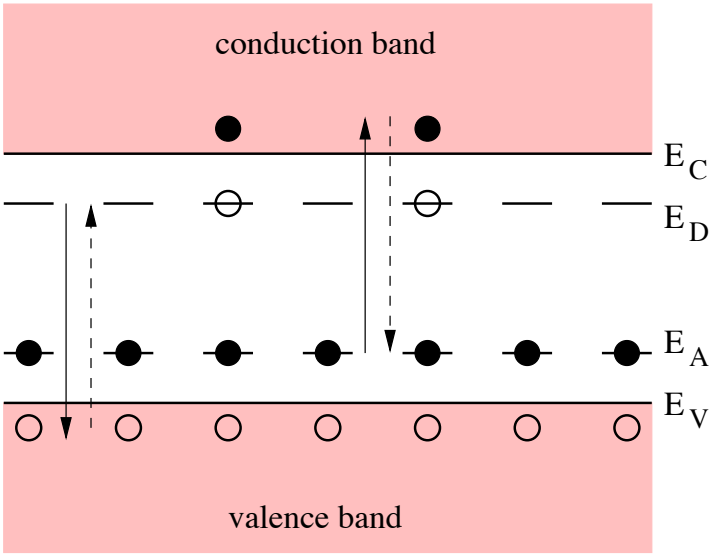

Figure 4.8: Schematic description of the traps position and carriers transitions. Here, E_C, E_V, E_A, E_D indicates the energy levels of the conduction band, valence band, acceptor traps and donor traps, respectively. The dotted arrows refer to phonon-assisted transitions while the other arrows denotes the transitions due to electron-electron interactions.

4.5 Electrostatic potential and Fermi statistics

Due to the configuration depicted above, the electrostatic potential ϕ is the solution of the following Poisson equation:

$$\nabla \cdot \epsilon \nabla \phi = -q\,(p - n - N_A) - \rho_{trap}\,, \tag{4.18}$$

where ϵ is the electrical permittivity, q the elementary electronic charge, n and p the electron and hole densities, N_A the concentration of ionized acceptors and ρ_{trap} the charge density contributed by traps, which will be discussed in the next section.
Electron and hole densities can be computed from the electron and hole quasi-Fermi potentials, and vice-versa. If Fermi statistics is assumed, the formulas read:

$$\begin{aligned} n &= N_C\, F_{1/2}\left(\frac{E_{F,n} - E_C}{kT}\right), \\ p &= N_V\, F_{1/2}\left(\frac{E_V - E_{F,p}}{kT}\right), \end{aligned} \tag{4.19}$$

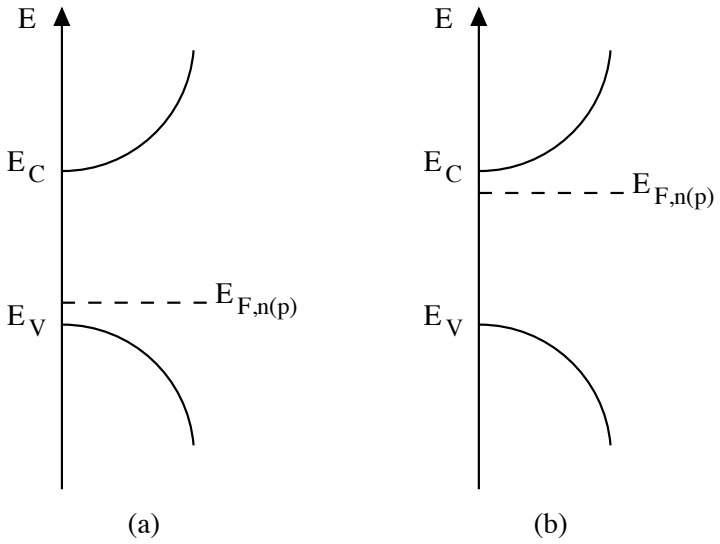

Figure 4.9: Schematic band diagram showing the position of the valence- and conduction-band edges and quasi-Fermi levels, in the equilibrium case (a) and at high current (b).

where $F_{1/2}$ is the Fermi integral of order 1/2.
Alternatively, the equations (4.19) can be rewritten as follows:

$$\begin{aligned} n &= \gamma_n N_C \exp\left(\frac{E_{F,n} - E_C}{kT}\right), \\ p &= \gamma_p N_V \exp\left(\frac{E_V - E_{F,p}}{kT}\right), \end{aligned} \tag{4.20}$$

where γ_n and γ_p are the functions of η_n and η_p:

$$\eta_n = \frac{E_{F,n} - E_C}{kT}, \quad \eta_p = \frac{E_V - E_{F,p}}{kT}, \tag{4.21}$$

$$\gamma_n = \frac{n}{N_C}\exp\left(-\eta_n\right), \quad \gamma_p = \frac{p}{N_V}\exp\left(-\eta_p\right), \tag{4.22}$$

In the equilibrium condition the quasi-Fermi levels are close to the valence band energy E_V and move below the energy level E_C when the current increases due to the electrons injection from traps (see Fig. 4.9).

4.6 Trap occupation dynamics

4.6.1 Acceptor traps

Acceptor traps are uncharged when unoccupied and they carry the charge of one electron when fully occupied.
The capture rate c^n for an empty trap and the emission rate e^n for a full trap are defined as follows:

$$\begin{aligned} c_C^n &= \alpha_n \cdot n \cdot (N - p) \,, \\ e_C^n &= \alpha_n \cdot [n_B + n_C \cdot r(I)] \cdot p \,, \end{aligned} \tag{4.23}$$

where the subscript C denotes the conduction band as the reservoir of carriers. The acceptor traps are coupled with the conduction band only. This is necessary to control the electrons concentration avoiding the generation of holes during the snapback event. As a consequence, $c_V^n = e_V^n = 0$.
The electron occupation f^n of an acceptor trap is a number between 0 and 1, and changes due to the capture and emission of electrons:

$$\frac{\partial f^n}{\partial t} = \sum_i r_i^n \,, \tag{4.24}$$

$$r_i^n = (1 - f^n)\, c_i^n - f^n e_i^n \,, \tag{4.25}$$

where the index i denotes the reservoir.
For the stationary state, the time derivative in eq. (4.24) vanishes. The occupation becomes:

$$f^n = \frac{\sum c_i^n}{\sum (c_i^n + e_i^n)} \,, \tag{4.26}$$

Replacing the equations (4.23) in (4.26), one finds:

$$f^n = \frac{\alpha_n \cdot n \cdot (N - p)}{\alpha_n \cdot \{n \cdot (N - p) + [n_B + n_C \cdot r(I)] \cdot p\}} \,. \tag{4.27}$$

In the equilibrium case with $r\,(I) = 0$ when $I = 0$ the occupation becomes:

$$f^n = \frac{n\ (N - p)}{n\ (N - p) + n_B \cdot p} \,. \tag{4.28}$$

In the subthreshold region the band electron concentration n is negligible compared to the hole concentration p, thus the coefficient n_B must be calibrated to obtain a trap electron concentration equal to p. The latter must be close, but not equal, to the total trap concentration N to ensure $f^n > 0$.
Above threshold $r\,(I) \gg 0$ and $e_C^n \gg c_C^n$, thus f^n becomes equal to zero, as expected, due to the injection of electrons from the traps to the band.

4.6.2 Donor traps

Donor traps are uncharged when unoccupied and they carry the charge of one hole when fully occupied.
The capture and emission rates are symmetrical to those described above for the acceptor traps and can be obtained replacing n with p and vice-versa:

$$\begin{aligned} e_V^p &= \alpha_p \cdot p \cdot (N - n) \,, \\ c_V^p &= \alpha_p \cdot [p_B + p_C \cdot r(I)] \cdot n \,, \end{aligned} \tag{4.29}$$

where the subscript V denotes the valence band as the reservoir of carriers. The donor traps are coupled with the valence band only. This is necessary to reduce the holes concentration during the snapback event and to mimic the emptying of the chalcogenide material's traps. As a consequence, $c_C^p = e_C^p = 0$.
The electron occupation f^n for donor traps is found to be:

$$f^n = \frac{\alpha_p \cdot p \cdot (N - n)}{\alpha_p \cdot \{p \cdot (N - n) + [p_B + p_C \cdot r(I)] \cdot n\}} \tag{4.30}$$

In the equilibrium case with $r\,(I) = 0$ when $I = 0$ the occupation becomes:

$$f^n = \frac{p\ (N - n)}{p\,(N - n) + p_B \cdot n} \tag{4.31}$$

At low current the band electron concentration n is negligible compared to the hole concentration p, thus the capture term always prevails on the emission term. As a consequence, in the subthreshold region $f^n \sim 1$, which means that the hole occupation f^p is equal to zero.
At high current $r\,(I) \gg 0$ and $e_C^n \gg c_C^n$, thus f^n becomes equal to zero ($f^p \sim 1$), as expected, due to the capture of holes from the valence band to the traps.

4.7 Results and improvement of the TCAD code

The $V(I)$ relation found by the present model, in a 1-D uniform case, is N-shaped, this corresponding to the expected snap-back behavior of the $V(I)$ curve (see Fig. 4.10). The latter is obtained by fixing the following values for the parameters of (4.23) and (4.29): $N = 10^{19}\,\mathrm{cm}^{-3}$, $N_A = 10^{18}\,\mathrm{cm}^{-3}$, $n_B = n_C = 10^{-2}\,\mathrm{cm}^{-3}$, $p_B = 6\,\mathrm{cm}^{-3}$, $p_C = 10^{-20}\,\mathrm{cm}^{-3}$, $\alpha_p = \sigma_p u_{th,p}$ and $\alpha_n = \sigma_n u_{th,n}$, where the capture cross sections are set to $\sigma_n = \sigma_p \sim 5 \times 10^{-17}\,\mathrm{cm}^2$, and, at room temperature the thermal velocities are set to $u_{th,n} \sim 2 \times 10^7\,\mathrm{cm/s}$ and $u_{th,p} \sim 1.6 \times 10^7\,\mathrm{cm/s}$. The trap mobility is set to $0.04\,\mathrm{cm}^2/\,(\mathrm{Vs})$ while the threshold current $I_K = 0.1 \times 10^{-7}\,\mathrm{A}$.
As shown in Fig. 4.11 and Fig. 4.12, the code is able to reproduce the alternation

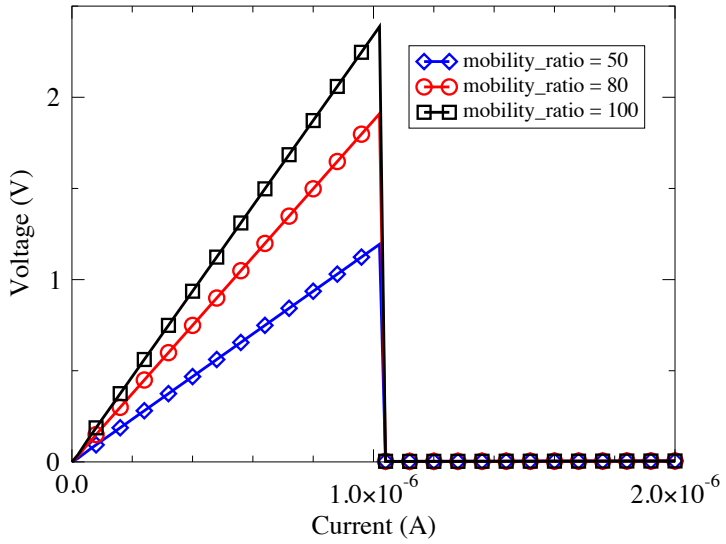

Figure 4.10: $V(I)$ characteristics for different values of the hole mobility.

of two different charge carriers, the holes in the subthreshold region and the band electrons after the snapback. The former can be treated as trapped electrons by enabling one of the built-in TCAD mobility models, such as the Poole-Frenkel model, or creating an ad-hoc PMI which fits the experimental $V(I)$ characteristics behavior.

Another feature of the code is the capability to represent the quasi-Fermi level shift during the current sweep (see Fig. 4.13), depending on the function $r(I)$ and the parameters n_C and p_C.

In the previous code (version TCAD D-2010 described in section 4.3) the traps were not included and the model was implemented through a PMI for the definition of the generation-recombination rate.

Due to the electron-hole pair generation during the snapback event, it was necessary to limit the charge carrier concentration considering the holes as empty traps and decreasing their mobility after the snapback. As a consequence, in the subthreshold region the hole concentration was low, while became close to N at high current. However, J_p was made negligible with respect to J_n through the PMI mobility model. This unphysical issue has been overridden in the new code where, at snapback, the vanishing of the trap-electron concentration (described by holes) occurs, which makes its contribution to the total current density irrelevant.

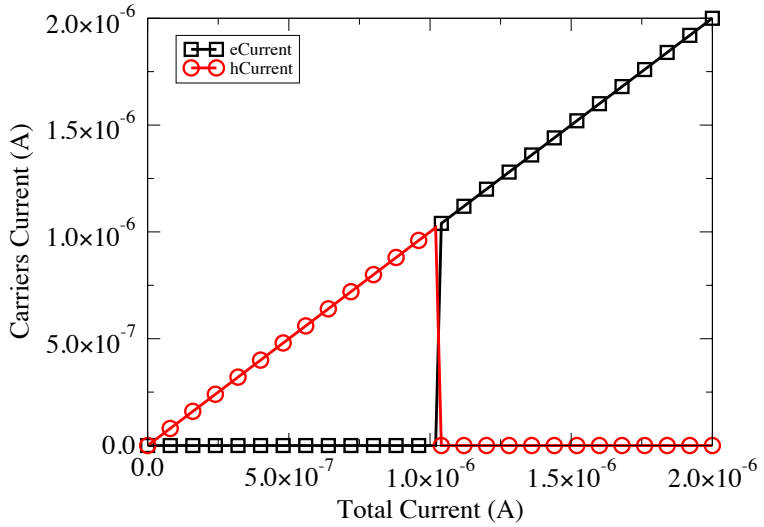

Figure 4.11: The figure shows the alternation of two different contribution to the total current: the hole current in the subthreshold region and the electron current above snapback.

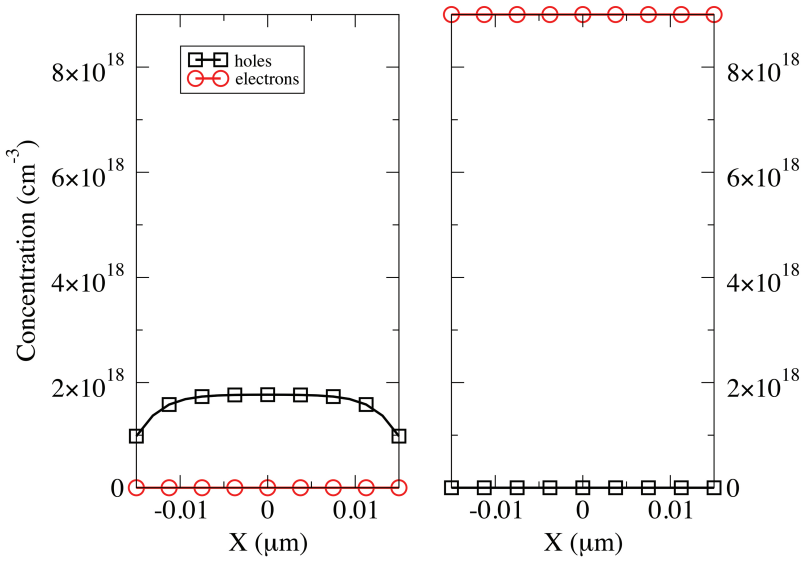

Figure 4.12: Electron and hole concentration at the equilibrium for $I = 0$ (left) and at high current (right).

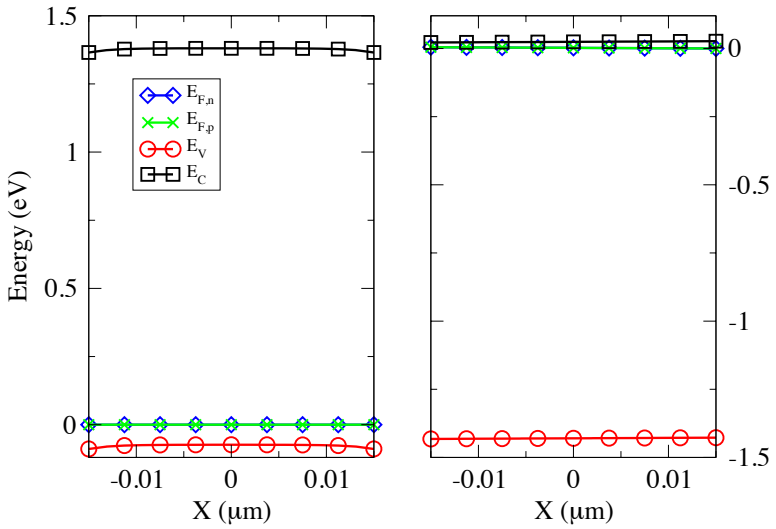

Figure 4.13: The figure shows the position of the valence- and conduction-band edges and quasi-Fermi levels, in the equilibrium case (a) and at high current (b)

Conclusion

An overview of different DC transport mechanisms based on the established physics of chalcogenide glasses has been presented. Several models are capable of accounting for the various observed exponential field dependencies of the conductivity. Unfortunately, almost all the considered mechanism are candidate explanations. Only Schottky emission and classical hopping conduction can be ruled out. It is difficult to identify a particular mechanism through the analysis of IV data alone and further studies are required to discriminate between the different mechanisms.

At this purpose, the overview has been followed by the introduction of a new transport model that is able to physically explain the electrical behaviour of the device in each operative region, not only in a defined domain. The feedback mechanism that produces the snap-back phenomenon in amorphous-GST memory devices is described as a filamentation in energy: electrons that belong to low-energy states within the traps move by phonon-assisted hopping among traps, while electrons belonging to higher-energy, extended states move within the conduction band. The former group of carriers has a much smaller mobility that the latter. Trap-to-band transitions are induced mainly by the Coulomb interactions of a trap electron with a number of band electrons; phonon absorption and emission also play a role. The different types of transitions are modeled by a net recombination-generation rate including a term describing the effects of the collective Coulomb interactions. The analysis of the feedback shows that the snap-back effect is determined by both the sharpness of such a term and the difference in mobility between the trap and band electrons.

Thus, the heuristic expression of [21] for the J_n dependence has been replaced here by a physical derivation through equation (3.9) combined with the analysis of the band population carried out in this thesis.

The effect of the many-level transitions induced by the cooperative interactions between band and trap electrons has been investigated inthis work. The main results are *i)* the role of the power-like energy dependence of the cross section σ has been clarified:the parameters Δ_{sk}, E_0, and r fix the threshold energy and

the sharpness of the behavior of $\dot{P}^E_{sk}$ around threshold. *ii)* The dependence of $\dot{P}^E_{sk}$ on the external perturbation is due to the form of the energy distribution of the bandelectrons; the estimate of the integral (3.6) confirms that $\dot{P}^E_{sk}$ is an exponentially-increasing function of E_n, which in turn explains the positive feed-back mechanism in the transport process [21]. *iii)* The analysisalso shows that two mechanisms contribute to the feed-back: they arethe tendency of the level populations to equalize and the increase in$\dot{P}^E_{sk}$ with the band population; the first one provides alarger supply of electrons able to make a transition from E_M to theband; then, the second one makes n to further increase at theexpense of the traps' population. *iv)* In the uniform case thedependence $n = n(\dot{P}^E_{rs})$ is worked out explicitly.

The transport model is completed by coupling the continuity equations for trap and band electrons, incorporating the new recombination-generation rate, with the transport and Poisson equations. The model has been applied in two ways: first, in a version that lends itself to an analytical expression of the device conductance, second in the full version implemented into a state-of-the-art device-simulation code. The analytical version is useful to discuss the feedback mechanism and the scaling properties of the device. Despite its simplicity, the analytical model proved able to exhibit the snap-back behavior even in the case of one-dimensional, uniform structures. The implementation into the device-simulation code corroborates the findings obtained from the analytical version, and provides the basis for investigating device architectures featuring non-uniform physical properties and more complex geometries.

Curriculum Vitae

Fabio Giovanardi was born in Rimini, Italy, on September 13, 1984. He received his 1-st and 2-nd level Master Degree (with honours) in Electronic Engineering in 2006 and 2009, respectively. In 2010 he joined the Department of Electronics Computer Science and Systems (DEIS) of the University of Bologna as Ph.D. student, working on a project focused on the microscopic analysis of the structural and transport features affecting the electrical threshold of amorphous GST. From June 2011 to February 2012 he was visiting researcher at Stanford University, CA, USA, during an internship at Intel Corp. as part of a joint project on PCMs. He is currently working with the ARCES device modeling and simulation group.

List of Publications

Conference Publications

[1] M. Rudan, F. Giovanardi, E. Piccinini, F. Buscemi, R. Brunetti and C. Jacoboni, "A new hopping model for transport in chalcogenide glasses", ISDRS 2009 Proceedings, The University of Maryland, College Park, MD, USA, December 9-11, 2009.

[2] M. Rudan, F. Giovanardi, T. Tsafack, F. Xiong, E. Piccinini, F. Buscemi, A. Liao, E. Pop, R. Brunetti and C. Jacoboni, "Modeling of the Voltage Snap-Back in Amorphous-GST Memory Devices", SISPAD 2010 Proceedings, Bologna, ITA, September 6-8, 2010.

[3] F. Buscemi, E. Piccinini, F. Giovanardi, M. Rudan, R. Brunetti and C. Jacoboni, "Quantum Electronic Trap-to-Band Transitions in Chalcogenides Induced by Electron-Electron Interaction", SISPAD 2011 Proceedings, Osaka, JAPAN, September 8-10, 2011.

[4] M. Rudan, F. Buscemi, G. Marcolini, F. Giovanardi, A. Cappelli, E. Piccinini and R. Brunetti, "Many-Level Trap-to-Band Transitions in Chalco-

genide Memories", SISPAD 2012 Proceedings, Denver, Colorado, USA, September 5-7, 2012.

Journal Publications

[1] M. Rudan, F. Giovanardi, E. Piccinini, F. Buscemi, R. Brunetti and C. Jacoboni, "Voltage Snap-Back in Amorphous-GST Memory Devices: Transport Model and Validation", IEEE Trans. on Electron Devices, vol. 58, Issue 12, p. 4361–4369, December 2011

Bibliography

[1] D. Adler et al. Threshold switching in chalcogenide-glass thin films. *J. Appl. Phys.*, 51(6):3289, 1980. [cited at p. 33]

[2] V. Abakumov, V. Perel, and I. Yassievich. Nonradiative Recombination in Semiconductors. *Modern Problems in Condensed Matter Science*, 33, 1991. [cited at p. 16, 17, 18]

[3] D. Allsopp and M. J. Thompson. High-field effects in chalcogenide switching glasses. *J. Phys. D: Appl. Phys.*, 9:2075, October 1976. [cited at p. 12]

[4] P. W. Anderson. Model for the electronic structure of amorphous semiconductors. *Phys. Rev. Lett.*, 34:953–955, Apr 1975. [cited at p. 23]

[5] A. L. Ankudinov, B. Ravel, J. J. Rehr, and S. D. Conradson. Real-space multiple-scattering calculation and interpretation of x-ray-absorption near-edge structure. *Phys. Rev. B*, 58:7565–7576, Sep. 1998. [cited at p. 4]

[6] B.G. Bagley. The field dependent mobility of localized electronic carriers. *Solid State Communications*, 8(5):345 – 348, 1970. [cited at p. 24]

[7] S. D. Baranovskii and V. G. Karpov. *Sov. Phys. Semiconductors*, 20:1137, 1986. [cited at p. 23]

[8] F. Bedeschi, R. Bez, C. Boffino, E. Bonizzoni, E. C. Buda, G. Casagrande, L. Costa, M. Ferraro, R. Gastaldi, O. Khouri, F. Ottogalli, F. Pellizzer, A. Pirovano, C. Resta, G. Torelli, and M. Tosi. 4-mb mosfet-selected mu;trench phase-change memory experimental chip. *Solid-State Circuits, IEEE Journal of*, 40(7):1557 – 1565, july 2005. [cited at p. 11]

[9] N.A. Bogoslowsky and K.D. Tsendin. Nonlinearity of current-voltage characteristics of chalcogenide glassy semiconductors, caused by multiphonon tunnel ionization of negative-U-centers. *Semiconductors*, 43:1338–1342, 2009. [cited at p. 12]

[10] Geoffrey W. Burr, Matthew J. Breitwisch, Michele Franceschini, Davide Garetto, Kailash Gopalakrishnan, Bryan Jackson, Bülent Kurdi, Chung Lam, Luis A. Lastras, Alvaro Padilla, Bipin Rajendran, Simone Raoux, and Rohit S. Shenoy. Phase change memory technology. *Journal of Vacuum Science & Technology B: Microelectronics and Nanometer Structures*, 28(2):223–262, 2010. [cited at p. 11]

[11] F. Buscemi, P. Bordone, and A. Bertoni. Entanglement dynamics of electron-electron scattering in low-dimensional semiconductor systems. *Phys. Rev. A*, 73:052312, 2006. [cited at p. 42, 55, 57]

[12] F. Buscemi, E. Piccinini, R. Brunetti, M. Rudan, and C. Jacoboni. Monte Carlo simulation of charge transport in amorphous chalcogenides. *J. Appl. Phys.*, 106:103706, 2009. [cited at p. xviii, 37]

[13] D. C. Kau et al. A stackable cross point phase change memory. In *IEDM Technical Digest*, pages 617–620, 2009. [cited at p. xvii, 58]

[14] H.J de Wit and C Crevecoeur. The electrical conduction of glassy As_2Se_3 at high fields. *Journal of Non-Crystalline Solids*, 8–10(0):787 – 792, 1972. Amorphous and Liquid Semiconductors. [cited at p. 18, 22]

[15] S. Eilert, M. Leinwander, and G. Crisenza. In *Proc. of the IEEE International Memory Workshop, IMW 2009*, pages 1–2, Monterey, CA, 2009. [cited at p. 11]

[16] M.M El-Samanoudy. Modified Poole-Frenkel mechanisms in $Ge_25Bi_xSb_{15--x}S_60$ thin films. *Applied Surface Science*, 207(1–4):219 – 226, 2003. [cited at p. 12, 18]

[17] S.R. Elliott. Medium-range order in amorphous materials: documented cases. *Journal of Non-Crystalline Solids*, 97–98, Part 1(0):159 – 162, 1987. [cited at p. 21]

[18] A. Bravaix et al. Hot-carrier acceleration factors for low power management in DC-AC stressed 40 nm NMOS node at high temperature. *Proc. of Int. Reliab. Phys. Symp.*, 531, 2009. [cited at p. 43]

[19] C. Hess et al. The Physics of Determining Chip Reliability. *Circ. Dev. Mag.*, 33, May 2010. [cited at p. 43, 44]

[20] F. Buscemi et al. Quantum Electronic Trap to Band Transitions in Chalcogenides Induced by Electron-Electron Interaction. In *Proc. SISPAD-2011*, volume 231, Osaka, 2011. [cited at p. 42, 43]

[21] M. Rudan et al. Voltage Snapback in Amorphous-GST Memory Devices: Transport Model and Validation. *IEEE Trans. on Electron Devices*, 58(4361), 2011. [cited at p. 42, 47, 48, 50, 77, 78]

[22] S.E. Tyaginov et al. Interface traps density-of-states as a vital component for hot-carrier degradation model. *Microelectronics Reliability*, 50(1267), 2010. [cited at p. 43, 48]

[23] W. Wang et al. Enabling Universal Memory by Overcoming the Contradictory Speed and Stability Nature of Phase-Change Materials. *Nature: Scientific Reports*, 2(360), April 2012. [cited at p. xiii]

[24] F. Xiong et al. Ultra-low current phase-change antifuse with carbon nanotube electrodes. In *Proceedings of the NVTMS Conference*, 2009. [cited at p. vi, 64, 65]

[25] F. Xiong et al. Ultra-low power phase-change memory with carbon nanotube interconnects. In *Proceedings of the DRC Conference*, 2010. [cited at p. vi, 66, 68]

[26] J. Frenkel. *Phys. Rev.*, 54(657), 1938. [cited at p. 12]

[27] Hellmut Fritzsche. Why are chalcogenide glasses the materials of choice for Ovonic switching devices? *Journal of Physics and Chemistry of Solids*, 68(5 – 6):878 – 882, 2007. 7th International Conference of Solids State Chemistry 2006 (SSC 2006). [cited at p. 26]

[28] J. González-Hernández, E. F. Prokhorov, Yu. V. Vorobiev, E. Morales-Sánchez, A. Mendoza-Galván, S. A. Kostylev, Yu. I. Gorobets, V. N. Zakharchenko, and R. V. Zakharchenko. Mechanism of the isotermic amorphous-to-crystalline phase transition in gesbte ternary alloys. volume 19, pages 1623 – 1629. AVS, 2001. [cited at p. 29]

[29] Tamihiro Gotoh. Characteristics at high electric fields in amorphous $Ge_2Sb_2Te_5$ films. *Journal of Non-Crystalline Solids*, 354(19 – 25):2728 – 2731, 2008. [cited at p. 18]

[30] Robert M. Hill. Poole-Frenkel conduction in amorphous solids. *Philosophical Magazine*, 23(181):59–86, 1971. [cited at p. 12, 16, 17]

[31] D. Ielmini. Threshold switching mechanism by high-field energy gain in the hopping transport of chalcogenide glasses. *Phys. Rev. B*, 78:035308, 2008. [cited at p. xviii, 12, 17, 23, 24, 35]

[32] D. Ielmini and Y. Zhang. Analytical model for subthreshold conduction and threshold switching in chalcogenide-based memory devices. *J. Appl. Phys.*, 102(5):054517, September 2007. [cited at p. vi, xviii, 12, 17, 23, 24, 35, 60, 66, 68]

[33] D. Ielmini and Y. Zhang. Evidence for trap-limited transport in the subthreshold conduction regime of chalcogenide glassess. *Appl. Phys. Lett.*, 90(19):192102, May 2007. [cited at p. 55, 63]

[34] I. V. Karpov, D. Kencke, S. Tang D. Kau, and G. Spadini. In *Proceedings of the Materials Research Society Symposium*, volume 1250, pages G14–01–H07–01, San Francisco, CA, 2011. [cited at p. 11, 16]

[35] V. G. Karpov, Y. A. Kryukov, S. D. Savransky, and I. V. Karpov. Nucleation switching in phase change memory. *Applied Physics Letters*, 90(12):123504, 2007. [cited at p. 34]

[36] T.G.M. Kleinpenning. 1/f noise in solid state single injection diodes. *Physica B+C*, 94(2):141 – 151, 1978. [cited at p. 22]

[37] M.L. Knotek. Temperature and thickness dependence of low temperature transport in amorphous silicon thin films: A comparison to amorphous germanium. *Solid State Communications*, 17(11):1431 – 1433, 1975. [cited at p. 23]

[38] I. F. Kodgespirova, V. A. Shkut, and S. A. Kostylev. *Proceedings of the International Conference on Amorphous Semiconductors*, pages 247 – 249, 1982. in Russian. [cited at p. 12, 22]

[39] V. I. Kol'dyaev. Nonlinear Frenkel and Poole effects. *Philosophical Magazine Part B*, 79(2):331–342, 1999. [cited at p. 17]

[40] A. V. Kolobov, P. Fons, A. I. Frenkel, A. L. Ankudinov, J. Tominaga, and T. Uruga. Understanding the phase-change mechanism of rewritable optical media. *Nature Mater.*, 3:703–708, Oct. 2004. [cited at p. 5, 9]

[41] S. Lai and T. Lowrey. In *Tech. Dig. - Int. Electron Devices Meet. 2001*, volume 803, 2001. [cited at p. 11]

[42] M. A. Lampert and P. Mark. *Current Injection in Solids.* Academic Press, New York, 1970. [cited at p. 21]

[43] É A. Lebedev, S.A. Kozykhin, N.N. Konstantinova, and L.P. Kazakova. Conductivity of layers of a chalcogenide glassy semiconductor $Ge_2Sb_2Te_5$ in high electric fields. *Semiconductors*, 43:1343–1346, 2009. [cited at p. 12]

[44] E. A. Lebedev and N. A. Rogachev. *Sov. Phys. Semiconductors*, 15(86), 1981. [cited at p. 19, 20, 23]

[45] Bong-Sub Lee, John R. Abelson, Stephen G. Bishop, Dae-Hwan Kang, Byung ki Cheong, and Ki-Bum Kim. Investigation of the optical and electronic properties of $Ge2Sb_2Te_5$ phase change material in its amorphous, cubic, and hexagonal phases. *Journal of Applied Physics*, 97(9):093509, 2005. [cited at p. 17]

[46] Suyoun Lee, Doo Seok Jeong, Jeung hyun Jeong, Wu Zhe, Young-Wook Park, Hyung-Woo Ahn, and Byung ki Cheong. A study on the temperature dependence of the threshold switching characteristics of $Ge_2Sb_2Te_5$. *Applied Physics Letters*, 96(2):023501, 2010. [cited at p. 17, 23, 24]

[47] C. Lefurgy, K. Rajamani, F. Rawson, W. Felter, M. Kistler, and T.W. Keller. Energy Management for Commercial Servers. *Computer*, 36(12):39–48, December 2003. [cited at p. xvii]

[48] E. I. Levin, I. M. Ruzin, and B. I. Shklovskii. *Sov. Phys. Semiconductors*, 22:401, 1998. [cited at p. 25, 26]

[49] I. M. Lifshits, S. A. Gredeskul, and L. A. Pastur. *Introduction to the Theory of Disordered Systems*. John Wiley & Sons, New York, 1988. [cited at p. 20]

[50] J. M. Marshall and A. E. Owen. The mobility of photo-induced carriers in disordered As_2Te_3 and $As_{30}Te_48Si_{12}Ge_{10}$. *Philosophical Magazine*, 31(6):1341–1356, 1975. [cited at p. 22]

[51] N.F. Mott and E.A. Davis. *Electronic processes in noncrystalline materials*. Clarendon Press, Oxford, 1961. [cited at p. 17, 22, 23, 30]

[52] M. Nardone, V. G. Karpov, D. C. S. Jackson, and I. V. Karpov. A unified model of nucleation switching. *Applied Physics Letters*, 94(10):103509, 2009. [cited at p. 32]

[53] T. Nonaka, G. Ohbayashi, Y. Toriumi, Y. Mori, and H. Hashimoto. *Thin Solid Films*, 370:258, 2000. [cited at p. 4]

[54] J.H. Oh, J.H. Park, Y.S. Lim, H.S. Lim, Y.T. Oh, J.S. Kim, J.M. Shin, Y.J. Song, K.C. Ryoo, D.W. Lim, S.S. Park, J.I. Kim, J.H. Kim, J. Yu, F. Yeung, C.W. Jeong, J.H. Kong, D.H. Kang, G.H. Koh, G.T. Jeong, H.S. Jeong, and Kinam Kim. Full integration of highly manufacturable 512mb pram based on 90nm technology. In *Electron Devices Meeting, 2006. IEDM '06. International*, pages 1–4, dec. 2006. [cited at p. 11]

[55] R.S. Ovshinsky. Reversible electrical switching phenomena in disordered structures. *Phys. Rev. Lett.*, 21:1450–1453, 1968. [cited at p. xvii, 3]

[56] A.E. Owen and J.M. Robertson. Electronic conduction and switching in chalcogenide glasses. *Electron Devices, IEEE Transactions on*, 20(2):105–122, Feb. 1973. [cited at p. 24]

[57] F Pellizzer, A Benvenuti, B Gleixner, Y Kim, B Johnson, M Magistretti, T Marangon, A Pirovano, R Bez, and G Atwood. A 90nm phase change memory technology for stand-alone non-volatile memory applications, 2006. [cited at p. 11]

[58] I. I. Petrov, R. M. Imamov, and Z. G. Pinsker. *Sov. Phys. Cryst.*, 13:339, 1968. [cited at p. 4]

[59] W. A. Phillips. Two-electron excitations and the low temperature properties of glasses. *Philosophical Magazine*, 34(6):983 – 991, 1976. [cited at p. 23]

[60] A. Pirovano, A. L. Lacaita, A. Benvenuti, F. Pellizzer, and R. Bez. Electron switching in phase-change memories. *IEEE Transactions on Electron Devices*, ED-51(3):452–459, March 2004. [cited at p. 33]

[61] M. Pollak and J. J. Hauser. Note on the anisotropy of the conductivity in thin amorphous films. *Phys. Rev. Lett.*, 31:1304 – 1307, Nov 1973. [cited at p. 24]

[62] H. H. Poole. *Lond. Edinb. Dubl. Phil. Mag.*, 33(112), 1916. [cited at p. 12]

[63] M. K. Qureshi, V. Srinivasan, and J. A. Rivers. Scalable High Performance Main Memory System Using Phase-Change Memory Technology. In *Proc. ISCA09*, Austin, June 2009. [cited at p. xvii]

[64] M. E. Raikh and I. M. Ruzin. *Mesoscopic Phenomena in Solids.* B. L. Altshuller, P. A. Lee, and R. A. Webb, Elsevier, New York, 1991. [cited at p. 24, 25]

[65] J. M. Robertson. Ph.d. thesis, 1971. [cited at p. 22]

[66] M. Rudan, F. Giovanardi, T. Tsafack, F. Xiong, E. Piccinini, F. Buscemi, A. Liao, E. Pop, R. Brunetti, and C. Jacoboni. Modeling of the Voltage Snap-Back in Amorphous-GST Memory Devices. In *Proc. of the sispad 2010 Conference*, pages 257–260, Bologna, Italy, September 2010. IEEE. [cited at p. 64]

[67] V. K. Saraswat, V. Kishore, Deepika, N. S. Saxena, T. P. Sharma, L. I. Singh, and P. K. Saraswat. I-V Measurements of Se-Te-Sb Glassy Bulk and Thin Film samples. *Chalcogenide Letters*, 5:95 – 103, May 2008. [cited at p. 12]

[68] G. Servalli. A 45nm generation phase change memory technology. In *Electron Devices Meeting (IEDM), 2009 IEEE International*, pages 1–4, Dec. 2009. [cited at p. 11]

[69] Y-H Shih, M-H Lee, M. Breitwisch, R. Cheek, J.Y. Wu, B. Rajendran, Y. Zhu, E.K. Lai, C.F. Chen, H.Y. Cheng, A. Schrott, E. Joseph, R. Dasaka, S. Raoux, H. L Lung, and C. Lam. Understanding amorphous states of phase-change memory using frenkel-poole model. In *Electron Devices Meeting (IEDM), 2009 IEEE International*, pages 1–4, Dec. [cited at p. 18, 29]

[70] B. I. Shklovskii. *Sov. Phys. Semiconductors*, 13:53, 1979. [cited at p. 28]

[71] B. I. Shklovskii and A. L. Efros. *Electronic Properties of Doped Semiconductors.* Springer-Verlag, New York, 1992. [cited at p. 17, 24, 27, 31]

[72] M. Simon, M. Nardone, V. G. Karpov, and I. V. Karpov. Conductive path formation in glasses of phase change memory. *Journal of Applied Physics*, 108(6):064514, 2010. [cited at p. 34]

[73] S. M. Sze. *Physics of Semiconductor Devices.* John Wiley & Sons, NewYork, second edition, 1981. [cited at p. 18, 26, 59]

[74] E.N. Voronkov and S.A. Kozyukhin. Electrical conductivity of amorphous films of chalcogenide compounds in high electric fields. *Semiconductors*, 43:921–924, 2009. [cited at p. 12]

[75] F. Xiong, A. D. Liao, D. Estrada, and E. Pop. Low-power switching of phase-change materials with carbon nanotube electrodes. *Science*, 332:568–570, April 2011. [cited at p. vi, 61, 64, 66]

[76] N. Yamada and T. Matsunaga. In *International Symposium on Optical Memories. Technical Diges*, page 70, Jeju, Korea, 2004. [cited at p. 4]